MATEMATICKO-FYZIKÁLNÍ FAKULTA

Univerzita Karlova

DIPLOMOVÁ PRÁCE

Bc. Markéta Pešková

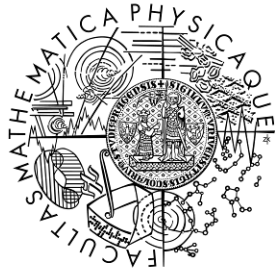## Studium azimutálních asymetrií v procesu Drell-Yan na zařízení COMPASS

Katedra fyziky nízkých teplot

Vedoucí diplomové práce: M.Sc. Michael Finger, CSc.

Studijní program: Fyzika

Studijní obor: Jaderná a subjaderná fyzika

Praha 2017

MASTER THESIS

Bc. Markéta Pešková

Study of azimuthal asymmetries in COMPASS Drell-Yan data

I declare that I carried out this master thesis independently, and only with the cited sources, literature and other professional sources.

I understand that my work relates to the rights and obligations under the Act No. 121/2000 Coll., the Copyright Act, as amended, in particular the fact that the Charles University in Prague has the right to conclude a license agreement on the use of this work as a school work pursuant to Section 60 paragraph 1 of the Copyright Act.

In Prague, 12.5.2017   signature

Název práce: Studium azimutálních asymetrií v procesu Drell-Yan na zařízení COMPASS

Autor: Bc. Markéta Pešková

Katedra / Ústav: Katedra fyziky nízkých teplot

Vedoucí diplomové práce: M.Sc. Michael Finger, CSc.

Abstrakt: Drell-Yan (DY) process, čili produkce leptonového páru z hadron-hadronové interakce, je jedním z unikátních nástrojů ke studiu hadronové struktury. V této práci představujeme teoretické pozadí za tímto procesem a jeho souvislost s popisem spinové struktury nukleonu. Je popsán formalismus Partonových Distribučních Funkcí (PDF) a PDF závislých na příčné hybnosti (TMD PDF), který s tímto procesem úzce souvisí. Dále je vysvětlena zásadní teoretická předpověď týkající se TMD PDF lichých při otočení času o změně jejich znaménka při měření v DY a v Semi-inkluzivním hlubokém nepružném rozptylu (SIDIS), kterou se snaží potvrdit experiment COMPASS. Experiment je stručně popsán v další části práce s důrazem na modifikace potřebné k měření DY procesu provedeného v letech 2014 a 2015 se 190 GeV/c^2 svazkem záporně nabitých pionů na protonovém terči (v roce 2015 polarizovaném). V poslední části přinášíme výsledky naší nezávislé analýzy dat z roku 2015. Byly extrahovány tři azimutální asymetrie, které dávají přístup k různým TMD, s použitím dat s koncovým stavem o dvou mionech a invariantní hmotě od 4.3 do 8.5 GeV/c^2. Naše výsledky jsou v souladu s výstupem oficiální analýzy, jež byla v současnosti podána k publikaci, a naznačují naplnění předpovědí o změně znaménka T-lichých TMD.

Klíčová slova: Drell-Yan proces, spinová struktura nukleonu, TMD PDF, Transverzální spinové asymetrie, COMPASS

Title: Study of azimuthal asymmetries in COMPASS Drell-Yan data

Author: Bc. Markéta Pešková

Department / Institute: Department of Low Temperature Physics

Supervisor of the master thesis: M.Sc. Michael Finger, CSc.

Abstract: Drell-Yan (DY) process, i.e. a lepton pair production in hadron-hadron interaction, is one of the unique tools to study structure of hadrons. In this thesis we present its theoretical background and its link to description of the nucleon spin structure. The corresponding formalism of the Parton Distribution Functions (PDF) and the Transverse Momentum Dependent Parton Distribution Functions (TMD PDF) is explained in some detail. The fundamental theoretical prediction of a sign change of the T-odd TMDs in the DY and Semi-inclusive DIS (SIDIS) is described. In the following a concise description of the COMPASS apparatus is given with the emphasis on the setup modification needed and implemented for the Drell-Yan measurement performed in 2014 and 2015 with 190 GeV/c^2 beam of negative pions and the proton target (polarised in 2015). In the final chapter we present our independent analysis of the DY data taken in 2015. Three azimuthal asymmetries giving access to the different TMD PDF were extracted using the dimuon events from a mass region of 4.3 to 8.5 GeV/c^2. Our results are in agreement with the official results recently submitted for publication, and give a significant hint toward the sign change.

Contents

Introduction

For the last hundred years the frontiers of the human knowledge of the microscopic structure of matter have been profoundly expanded. For more than 100 years ago, the famous scattering experiments performed by H. Geiger and E. Marsden on the advice of sir E. Rutherford heralded the birth of a new branch of physics studying matter on the nuclear and subnuclear level. The scattering experiments revealed the existence of an atomic nucleus and electron cloud, and gradually helped to penetrate deeper into the nucleus and discover its structure, made of protons and neutrons. With the improving resolution of the particle accelerators it has become clear that the nucleons are not the fundamental elementary particles which constitute matter. In the 50' in the Stanford University Robert Hofstadter brought an evidence of a finite radius of a nucleon from an elastic e-p scattering. In the late 60' the Stanford Linear Accelerator Center (SLAC) using the elastic and inelastic e-p scattering published the results indicating a presence of point-like constituents of a nucleon. The constituents were described by Feynman's Parton Model (PM) developed shortly after the discovery. In this model, the nucleon is composed of point-like fermions, so called partons which makes this model compatible with constituent quark model (QM) of Gell-Mann and Zweig, assuming valence quarks with spin ½ and electric charges of +2/3e and -1/3e. Further investigation of the inner dynamics in nucleon and hadrons in general lead to the formulation of the Quantum Chromodynamics (QCD) in the 70', a non-abelian quantum field theory describing strong interaction between the quarks intermediated by newly predicted and subsequently discovered vector bosons called gluons. QCD has defended its position as the most successful theory of strong interaction even after decades of experimental tests, and is still being tested. QCD improved PM has served for almost complete description of the structure of nucleons though a lot of unanswered questions remain regarding the low energy processes in hadrons (non-perturbative regime).

One of those questions appeared during the investigation of the nucleon spin. The problem was discovered in 1988 at the European Muon Collaboration (EMC) at CERN when testing the naïve theoretical prediction from the QM that the nucleon spin is fully given as a composition of the spins of the three valence quarks, however, the results that surprised the whole physics community have shown that quarks contribute only one third to the total spin of a nucleon [1]. This result has led to the formulation of new theoretical tools and stirred a lot

of experimental effort to explain the processes contributing to the nucleon spin and this "spin crisis" has not yet been resolved. This topic became a subject of study in lepton scattering experiments at CERN namely SMC and COMPASS, HERMES at DESY, SLAC laboratory, and JLab, and also in polarised proton-proton collider at RHIC. One of the possible contributions comes from the gluon polarisation ΔG, whose measurement was one of the points of interest of the HERMES, SMC, and the COMPASS. The COMPASS experiment, which is subject of this thesis, is a fixed target experiment located on the SPS M2 beamline at CERN. Experiments mentioned above also have contributed to measurement of the significant left-right spin asymmetries which suggested an important role of the intrinsic transverse momentum of partons connected with the orbital angular momentum (OAM), and the experimental efforts on this matter are still ongoing.

Nucleon structure can be described by spin-independent unpolarised structure functions $F_1 (x, Q^2)$ and $F_2 (x, Q^2)$, and the polarised structure functions, $G_1 (x, Q^2)$ and $G_2 (x, Q^2)$, which can be directly measured in the scattering experiments. In the parton model in the leading order in the collinear approximation (with parton intrinsic transverse momentum integrated over) they can be interpreted in terms of Parton Distribution Functions (PDF) f_1, g_1, and h_1. Nowadays, the understanding of the longitudinal structure of nucleon described by unpolarised PDF f_1 and helicity function g_1, has been virtually reached. However, the transverse structure of the nucleon concerning the intrinsic motion of partons and transverse spin distribution is still little known. Beyond the collinear approximation the nucleon structure is described by eight Transverse Momentum Dependent Parton Distribution Functions (TMDs). The knowledge of the intrinsic transverse momentum of partons and its correlation with spin is essential for determining parton orbital motion and thus hopefully answering the question for the origin of nucleon spin at last.

There are two experimental tools for obtaining TMDs which are complementary to each other[1], Semi-Inclusive Deep Inelastic Scattering (SIDIS), and Drell-Yan process (DY). The COMPASS experiment ("COmmon Muon and Proton Apparatus for Structure and Spectroscopy") design allows studying both of these processes with basically the same setup which gives the possibility to test the universality of the TMD picture and thus one of the important predictions of QCD.

---

[1] The connection of those processes and the implication for the theory will be described in the Section 1.6.

The aim of this thesis is the extraction of the leading twist transverse-spin-dependent azimuthal asymmetries (TSA) in polarised pion-induced Drell-Yan process from 2015 COMPASS data. In the following, the theoretical background on the structure of nucleon is reviewed. The details of the COMPASS spectrometer layout and experimental goals are presented in Chapter 2. In the following chapter, we will describe the data sample, the procedure for extracting the TSAs and the systematic studies. And in the final part, we will present the results obtained from our analysis.

1. Physics case: the Drell-Yan process

Scattering processes have played the most important role in probing the inner constituents of matter. The elastic scattering enabled to discover basic structure of atom in the times of Rutherford's experiment; measuring the size, shape, and the form-factors of the nuclei; the size and elastic form-factors of nucleons; and continues to be an important tool for testing of the Standard model. The deep inelastic scattering (DIS), involving the collision of electromagnetic probe (lepton) to the target particle, has moved the frontiers into the inner structure of nucleon and its dynamics. The measurement at SLAC in 1968 brought a clear evidence of point-like constituents of nucleon in the discovery of the Bjorken scaling. The DIS was the essential tool for linking the partons and quarks, and somewhat later for finding the missing constituent of nucleon, filling the gap in the measurements (see Chapter 1.2.3), the gluon. The polarised DIS, which uses longitudinally polarised lepton projectile and longitudinally or transversely polarised target nucleon, gave the access to the longitudinal spin structure of the nucleon via measuring the helicity distribution of partons in the nucleon. On the other hand, transversal spin structure described by the transversity distribution function or TMDs, being chiral odd, is not accessible by DIS. In the DIS the chiral odd processes are strongly suppressed, but in SIDIS, or DY the chiral odd processes can be observed.

In the following subsection the formalism of the DIS is shortly reviewed, the naïve Parton Model and QCD are introduced in the part 1.2. Then, the unpolarised and polarised structure of nucleon is presented, with the emphasis on the transverse spin distributions, the helicity and TMDs. In the last subsection 1.4 the DY process is discussed and its comparison to the complementary process of SIDIS and the process of extracting the TSAs in order to obtain the transverse spin distributions.

1.1. Kinematics of deep inelastic processes

The DIS is a process of scattering the charged or neutral lepton l with the momentum k on a nucleon H with the momentum P, as follows:

$$l(k) + H(P) \rightarrow l'(k') + X, \tag{1.1}$$

where X denotes any hadronic final state created from the energy transfer from the incoming lepton. If $X = H$ and $l = l'$ then (1.1) describes an elastic scattering, where no energy transfer occurs. In the case of the neutral current DIS processes $l = l'$, and the other case of the charged current processes involves leptons differing in one unit of electric charge e.

However, the latter process is not relevant for the topic of this thesis. The neutral intermediation particle can be either photon or Z boson, but for the following discussion we will consider the photon intermediator only[2]. The lowest order Feynman diagrams for the processes of elastic electron-proton scattering and the inelastic case scheme are shown on figures 1.1a and 1.1b, respectively. Concerning the DIS diagram 1.1b, the lepton vertex is described by the perturbative QED, while the photon-proton interaction involves non-perturbative QCD effects of the proton structure, described by the proton structure functions.

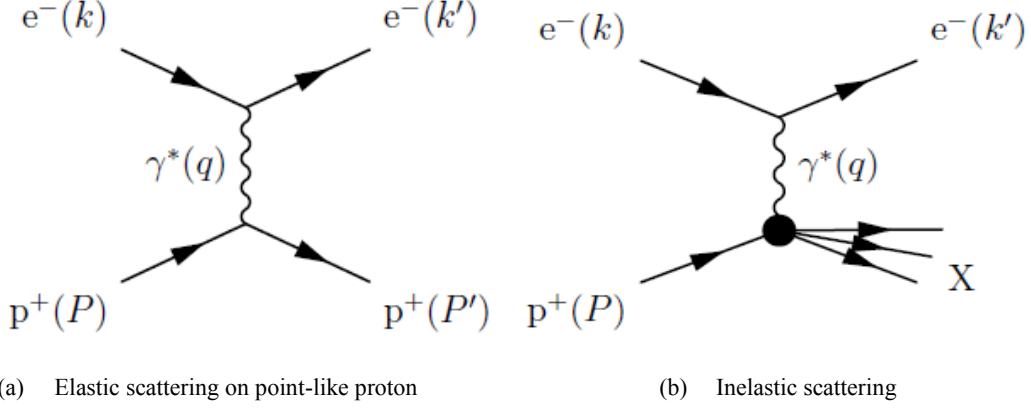(a)   Elastic scattering on point-like proton   (b)   Inelastic scattering

Figure 1.1: The lowest order Feynman diagram of electron-proton scattering (a) and the schematic of the inelastic e-p scattering. The diagrams are taken from ref. [3].

The following Lorentz invariant variables are commonly used for the description of DIS process [4]:

$$s \equiv (k + P)^2 = M^2 + 2k \cdot P = M_p(2E_{lab} + M_p), \tag{1.2}$$

$$Q^2 \equiv -q^2 = -(k - k')^2 = 2k \cdot k' = 2EE'\sin^2(\vartheta/2), \tag{1.3}$$

$$x \equiv \frac{Q^2}{2P \cdot q} = \frac{Q^2}{2M_p \upsilon} = \frac{Q^2}{Q^2 + W^2 - M_p^2}, \tag{1.4}$$

$$y \equiv \frac{q \cdot P}{k \cdot P} = \frac{E_{lab} - E'_{lab}}{E_{lab}} = \frac{\upsilon}{E_{lab}} = \left(\frac{s - M_p^2}{s}\right)\frac{1 - \cos\vartheta*}{2}, \tag{1.5}$$

$$W^2 \equiv (q + P)^2 = \frac{Q^2(1 - x)}{x} + M_p^2, \tag{1.6}$$

where W is the invariant mass of the hadronic system X produced by the absorption of the virtual photon by the nucleon. The Mandelstam invariant s denotes the center-of-mass (CMS) energy of the lp system squared. The M_p corresponds to the proton mass, while the lepton mass is neglected here; E and E' are the energies of the incoming and scattered lepton in the CMS, respectively, P and k, k' are the same as in eq. (1.1), and ϑ describes the scattering angle of the lepton. The Q^2 invariant is the negative value of the squared four-momentum of

_____

[2] In the COMPASS DIS experiments the CMS energy $\sqrt{s} \approx 20$ GeV/c^2 is well below the Z peak, thus its contribution can be safely neglected.

5

the virtual photon, i.e. a momentum transfer between the leptonic and hadronic system. The variable y gives the amount of energy transferred between the lepton and hadron system, and x stands for the Bjorken x variable which is related with the inelasticity of the collision. Bjorken x varies from 0 to 1, the latter being the elastic scattering, while with decreasing value we move to the higher energy scales. In the parton model the Bjorken x represents the fraction of momentum carried by a parton inside the proton. The momentum transfer is a measure of experimental resolution, so in the DIS kinematic domain, where $Q^2 \gg M_p$ and $P.q \gg M_p$ [4] it is high enough to probe the internal structure of nucleon. Note that (neglecting the masses) we can express $Q^2 \cong sxy$, which means that (for the unpolarised case) with the given s only two of the above invariants are independent.

Let us first remind the expression for the cross-section of a general process $1+2\rightarrow3+4+\ldots+n$:

$$d\sigma = \frac{(2\pi)^4}{|\vec{v}_1 - \vec{v}_2|}\frac{1}{2E_1}\frac{1}{2E_2}\left|M_{fi}\right|^2 \prod_{i=3}^{n}\frac{dp_i}{(2\pi)^3 2E_i}\delta^{(4)}\left(p_1 + p_2 - \sum_{i=3}^{n}p_n\right)S, \qquad (1.7)$$

where $\vec{v}_i$ is the velocity of a particle in initial state, and $p_i = (E_i, \vec{p}_i)$ denotes the four-momentum of the i-th particle. M_{fi} is the Lorentz-invariant amplitude of transition between initial and final state. S is the statistical factor standing for the case of more identical particles in final state. From this basic formula the cross-section for the elastic scattering of electron on a point-like proton can be derived [4]:

$$\frac{d\sigma}{dQ^2} = \frac{4\pi\alpha^2}{Q^4}\left(1 - y + \frac{y^2}{2} - \frac{M^2 y}{2kP}\right). \qquad (1.8)$$

And in the laboratory frame (LAB) we get:

$$\frac{d\sigma}{d\Omega_{lab}} = \sigma_{Mott}\frac{E'_{lab}}{E_{lab}}\left[1 + \frac{Q^2}{2M^2}\tan^2\left(\frac{\vartheta_{lab}}{2}\right)\right], \quad \sigma_{Mott} = \frac{\alpha^2 \cos^2(\vartheta_{lab}/2)}{4E_{lab}^2 \sin^4(\vartheta_{lab}/2)}, \qquad (1.9)$$

where σ_{Mott} is the Mott formula for scattering of relativistic Dirac particle (unpolarised) on static point-like charge potential, and α is fine structure constant. If we consider that proton has an internal structure, we have to modify the cross-section with the form-factors[3] or structure functions [4],[6]. After some treatment we arrive to the following expression:

$$\frac{d\sigma}{d\Omega_{lab}} = \sigma_{Mott}\frac{E'_{lab}}{E_{lab}}\left[\frac{G_E^2 + \tau G_M^2}{1+\tau} + 2\tau G_M^2 \tan^2\left(\frac{\vartheta_{lab}}{2}\right)\right], \qquad (1.10)$$

---

[3] Form-factor $F(q^2)$ is a Fourier transformation of charge distribution in a particle. In the scattering cross-section formula it accounts for the effect of the extension of the charge distribution from a nonpoint-like particle [5].

where $\tau = \dfrac{Q^2}{4M^2}$ and $G_E{}^2$ and $G_M{}^2$ are the electric and magnetic form-factors.

In the DIS the kinetic energy is not conserved, i.e. the variables Q^2 and v become independent, thus the eq. (1.10) changes. The following formulae are valid in CMS and LAB, respectively [4],[7]:

$$\frac{d^2\sigma}{dxdQ^2} = \frac{4\pi\alpha^2}{Q^4}\left[\left(1 - y - \frac{M^2xy}{s}\right)\frac{F_2(x,Q^2)}{x} + y^2 F_1(x,Q^2)\right], \qquad (1.11)$$

$$\frac{d^2\sigma}{dE'd\Omega_{lab}} = \sigma_{Mott}\left[\frac{M}{v}W_2(x,Q^2) + 2W_1(x,Q^2)\tan^2\left(\frac{\vartheta_{lab}}{2}\right)\right], \qquad (1.12)$$

where F_1 (x,Q^2) and F_2 (x,Q^2), or equivalently W_1 (v,Q^2) and W_2 (v,Q^2) are the inelastic electromagnetic form-factors or structure functions of the proton, which comes from symmetric part of the hadronic tensor $W^{\mu v}$ ($\sigma \propto \dfrac{1}{Q^4}L_{\mu v}W^{\mu v}$) [4][7]. Within the parton model the structure functions are related to the Parton Distribution Functions (PDFs) which will be discussed in the next section.

Let us now consider the polarised DIS with the longitudinally polarised lepton and longitudinally or transversely polarised target hadron:

$$l(k,\xi) + H(P,S) \rightarrow l'(k',\xi') + X, \qquad (1.13)$$

which is the same as (1.1) with only adding the spins of the lepton ξ, ξ' and hadron spin S, respectively. In the polarised case two additional polarised structure functions appear, $\widetilde{G}_1$ (v,Q^2) and $\widetilde{G}_2(v,Q^2)$ coming from the antisymmetric part of $W^{\mu v}$. Following equations apply for the W_i (v,Q^2) and $\widetilde{G}_i$ (v,Q^2):

$$MW_1(v,Q^2) = F_1(x,Q^2), \qquad (1.14)$$
$$vW_2(v,Q^2) = F_2(x,Q^2), \qquad (1.15)$$
$$\frac{v}{M}\widetilde{G}_1(v,Q^2) = G_1(x,Q^2), \qquad (1.16)$$
$$\frac{v^2}{M^2}\widetilde{G}_2(v^2) = G_2(x,Q^2), \qquad (1.17)$$

The longitudinally and transversely polarised DIS cross-section can be then expressed in the following way [7]:

$$\left(\frac{d^2\sigma^{\uparrow\Uparrow}}{d\Omega_{lab}dE'_{lab}} - \frac{d^2\sigma^{\uparrow\Downarrow}}{d\Omega_{lab}dE'_{lab}}\right) = \frac{4\alpha^2}{MvQ^2}\frac{E'_{lab}}{E_{lab}}\left[(E_{lab} + E'_{lab}\cos\vartheta)g_1(x,Q^2) - 2xg_2(x,Q^2)\right], \text{(1.18)}$$

$$\left(\frac{d^2\sigma^{\uparrow\Rightarrow}}{d\Omega_{lab}dE'_{lab}} - \frac{d^2\sigma^{\uparrow\Leftarrow}}{d\Omega_{lab}dE'_{lab}}\right) = \frac{4\alpha^2}{MvQ^2}\frac{E'^2_{lab}}{E_{lab}}\sin\vartheta\left[g_1(x,Q^2) - \frac{2E_{lab}}{v}g_2(x,Q^2)\right], \qquad (1.19)$$

where $\uparrow\downarrow$ denote the longitudinal polarisation of lepton and $\Uparrow\Downarrow, \Rightarrow\Leftarrow$ are the longitudinal and transversal polarisation of target nucleon, respectively. Averaging of the cross-section over the target spin orientations yields the equation 1.12 In the unpolarised cross-section the antisymmetric part of $W^{\mu\nu}$ and the lepton tensor $L^{\mu\nu}$ vanish and the cross-section is parametrized only be the form-factors $F_1\,(x,Q^2)$ and $F_2\,(x,Q^2)$, and on the contrary in the polarised one the antisymmetric part of hadronic and lepton tensor appear and structure functions $G_1\,(x,Q^2)$ and $G_2\,(x,Q^2)$ can be accessed. The experimental quantity that is measured for obtaining them is the longitudinal spin-spin asymmetry:

$$A_{\parallel} = \frac{\sigma^{\uparrow\Downarrow} - \sigma^{\uparrow\Uparrow}}{\sigma^{\uparrow\Downarrow} + \sigma^{\uparrow\Uparrow}} .\qquad(1.20)$$

Of course, the asymmetry gives access only to the combination of the polarised structure functions not the individual ones. Nevertheless, one can see that in (1.18) the coefficients of G_1 and G_2 differ in the magnitude, the G_2 contribution is suppressed w.r.t. G_1 by a factor M/E. Thus, the longitudinal double spin asymmetry is used for measuring G_1 function. On the other hand, in the process (1.19) no such suppression is present. Therefore, the function G_2 can be extracted using the double spin asymmetry $A_{\perp}$:

$$A_{\perp} = \frac{\sigma^{\uparrow\Rightarrow} - \sigma^{\uparrow\Leftarrow}}{\sigma^{\uparrow\Rightarrow} + \sigma^{\uparrow\Leftarrow}} ,\qquad(1.21)$$

combined with the G_1 known from the asymmetry (1.20).

1.2 Features of the parton model

1.2.1 The Unpolarised nucleon structure

The first measurements of the structure functions and elastic form-factors with electron-proton unpolarised DIS were performed at the SLAC laboratory (Standford Linear Accelerator) in the late 60'. The data showed factors a rapid decrease of the elastic form-factors with rising Q^2 and conversely the increase of the inelastic form-factors to a constant non-zero value. The explanation of this phenomenon was given by Richard P. Feynman, namely, that if the target nucleon has any internal structure, there is a lower probability that its constituents recombine back after the high energy collision. This behaviour of the nucleon form-factors had originally been predicted by James D. Bjorken [8], and then called after him, the Bjorken scaling. Later it has been shown that Bjorken scaling is an approximate scaling because the inelastic form-factors actually do approach zero, but very slowly. Thus, the equations (1.14)-(1.17) can be rewritten in a sense of Bjorken scaling:

$$\lim_{Q^2 \to \infty, \upsilon / Q^2 \, fixed} M W_1\left(\nu, Q^2\right) \to F_1(x), \qquad (1.22)$$

$$\lim_{Q^2 \to \infty, \upsilon / Q^2 \, fixed} \nu W_2\left(\nu, Q^2\right) \to F_2(x), \qquad (1.23)$$

$$\lim_{Q^2 \to \infty, \upsilon / Q^2 \, fixed} \frac{\nu}{M} \widetilde{G}_1\left(\nu, Q^2\right) \to G_1(x), \qquad (1.24)$$

$$\lim_{Q^2 \to \infty, \upsilon / Q^2 \, fixed} \frac{\nu^2}{M^2} \widetilde{G}_2\left(\nu, Q^2\right) \to G_2(x), \qquad (1.25)$$
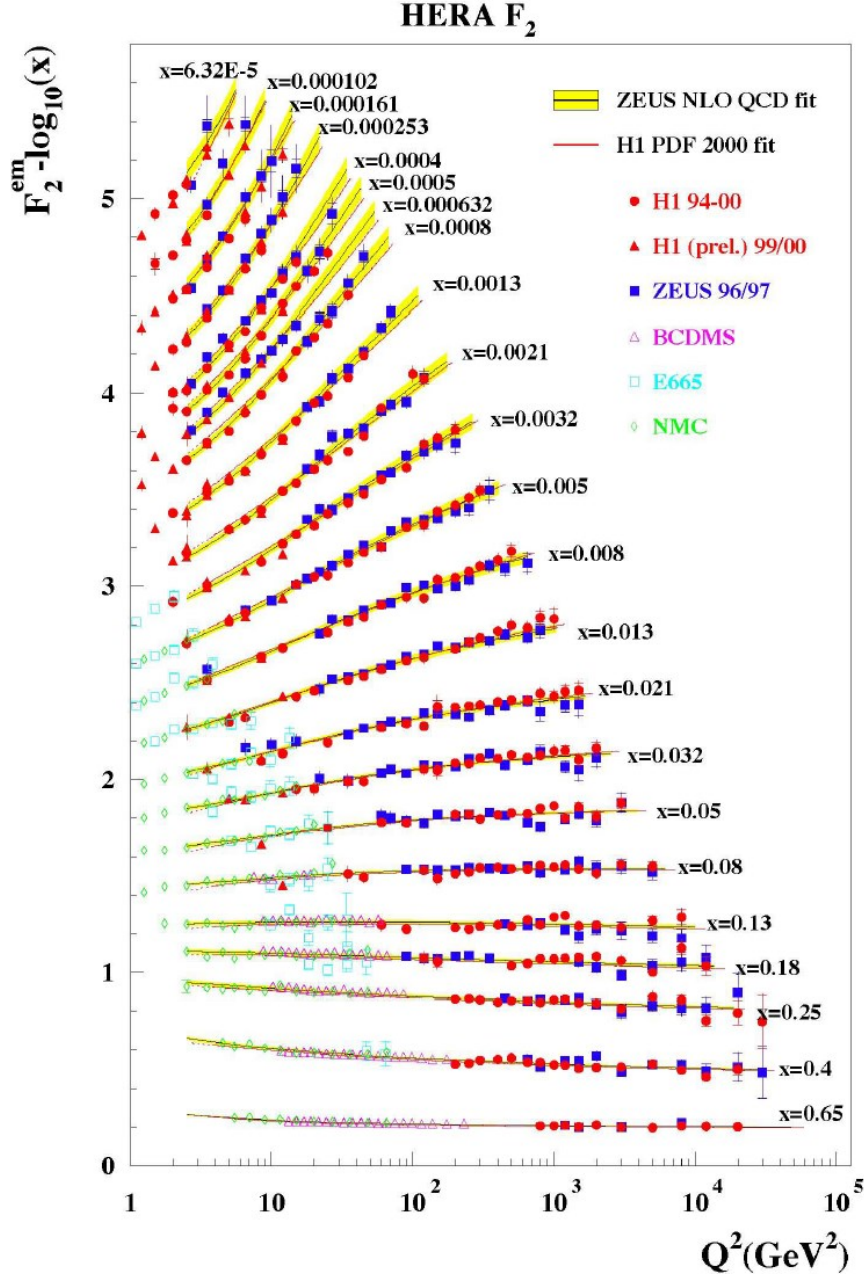

Figure 1.2: The scaling of proton structure function F_2 measured in electromagnetic scattering of positron beam from the fixed proton target in the experiments ZEUS [10] and H1 [11] at HERA, for x > 0.00006, and for electrons in SLAC [12] and muons in BCDMS [13], E665 [14], and NMC [15]. The data are plotted as a function of Q^2 in bins of x. Taken from ref. [9].

On the basis of the results of DIS experiments, Feynman formulated the parton model (Parton is an abbreviation for "part of proton" [9]). In the parton model the DIS is viewed as a "quasi-free scattering from point-like constituents within the proton, as viewed from a frame where proton has infinite momentum." [8]

In the infinite momentum frame the proton becomes Lorentz-contracted to a disc and the internal movement of the partons is strongly slowed down by the time dilatation, thus the constituents can be considered as free particles during the collision in the sense that the lifetime of the parton states is much longer than the duration of the collision. This makes the parton model valid only in high energy scale. The DIS cross-section is then an incoherent sum over elastic lepton-parton cross-sections. The hadronisation process (conversion of the partons to the final state hadrons) takes place much later after the collision, as can be seen on the figure 1.3. In the collinear approximation it is assumed that the transverse momentum of the partons can be neglected as well as their rest masses and only their longitudinal momentum is considered. The longitudinal momentum of the i-th parton can be expressed as a fraction of the proton momentum $\eta_i P$. Note that the momentum conservation law of the proton vertex in figure 1.1a:

$$\left(\eta_i P'\right)^2 = \left(\eta_i P\right)^2 - Q^2 + 2\eta_i Pq \Rightarrow Q^2 = 2\eta_i Pq, \tag{1.26}$$

implies that Bjorken x represents the fraction of the proton momentum η_i carried by a particular parton. Under the consideration of high energy limit $s \to \infty$ in (1.11), and thus the y variable being small, the elastic cross-section of electron on parton with charge fraction e_p is given:

$$\frac{d\sigma}{dQ^2} = \frac{4\pi\alpha^2 e_p^2}{Q^4}. \tag{1.27}$$

After comparing (1.11) with weighted sum of the partonic cross-sections, we get the inelastic electron-proton cross-section in high energy limit:

$$\frac{d\sigma}{dx dQ^2} = \frac{4\pi\alpha^2}{Q^4} \frac{F_2\left(x, Q^2\right)}{x} = \frac{4\pi\alpha^2}{Q^4} \sum_i e_i^2 f_i(x), \tag{1.28}$$

where $f_i(x)$ is the probability to find the i-th parton with charge e_i and momentum fraction xP inside the proton. The functions $f_i(x)$ are called the Parton Distribution Functions (PDFs). And the function $F_2(x,Q^2)$ is given as:

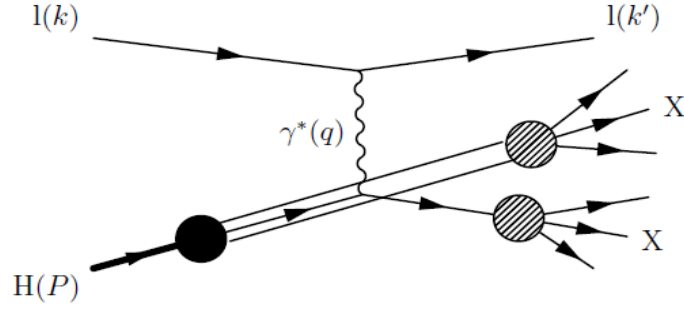$$F_2\left(x, Q^2\right) = F_2(x) = x \sum_i e_i^2 f_i(x). \tag{1.29}$$

Figure 1.3: Deep inelastic scattering in parton model. The process of hadronisation begins much latter after the collision; this is called the independent fragmentation model (taken from the ref. [5]).

Parton model then naturally leads to Bjorken scaling (F_2 does not depend on Q^2). Also the function $F_1(x)$ from the cross-section (1.11) contributes in finite energies. The relationship between $F_i(x)$ functions can be approximated by the Callan-Gross relation for partons with ½ spin: $F_2(x) = 2xF_2(x)$) which has been confirmed by experimental data, e.g. [4]. In the 1970's, the charged partons in the nucleon were unambiguously identified with the quarks from the additive quark model, proposed in 1964 to explain the hadron spectrum, but then some inconsistencies arose. One of the problems was the discrepancy between the experimental data and the probability definition of the structure function $F_2(x)$ expressed by the momentum sum rule:

$$\sum_i \int_0^1 x f_i(x) dx = 1, \tag{1.30}$$

as the actually measured value is only 0,5 [6]. It was a clear indication of a presence of some additional particles not interacting electromagnetically.

There is another problem with the interpretation of partons as quarks. As only u, d, c, and s quarks can be constituents of the proton (b and t are too heavy) the proton structure function can be calculated as a sum of the PDFs of all quarks and antiquarks:

$$F_2^p = x \left(\frac{4}{9} \left[f_u(x) + \bar{f}_u(x) + f_c(x) + \bar{f}_c(x) \right] + \frac{1}{9} \left[f_d(x) + \bar{f}_d(x) + f_s(x) + \bar{f}_s(x) \right] \right). \tag{1.31}$$

Integrating $F_2(x)$ over x we get a mean square charge per parton. The experimental value is $0,17 \pm 0,009$ [4] which is considerably lower than expected value of ⅓ of the 3-quark model, i.e. this is another strong indication for additional constituent particle in proton.

Another issue is the behavior of the parton distribution which is roughly proportional to $1/x$ for $x \rightarrow 0$ and the integral from this function diverges. This would imply an infinite

number of charged partons in the proton. We can define the so-called valence and sea PDFs as a combination of quark and antiquark distribution functions as follows:

$$f_q^{val}(x) \equiv f_q(x) - \bar{f}_q(x), \qquad f_q^{sea}(x) \equiv \bar{f}_q(x). \qquad (1.32)$$

Then the integral of the valence function for u and d quark is fully in agreement with static quark model [4]:

$$\int_0^1 f_u^{val}(x)dx \approx 2, \qquad \int_0^1 f_d^{val}(x)dx \approx 1, \qquad \int_0^1 f_s^{val}(x)dx \approx 0 \qquad (1.33)$$

while the integral of the sea PDFs diverges. These problems have been solved with the formulation of the QCD, a non-abelian gauge theory of strong interaction, see the section 1.2.3.
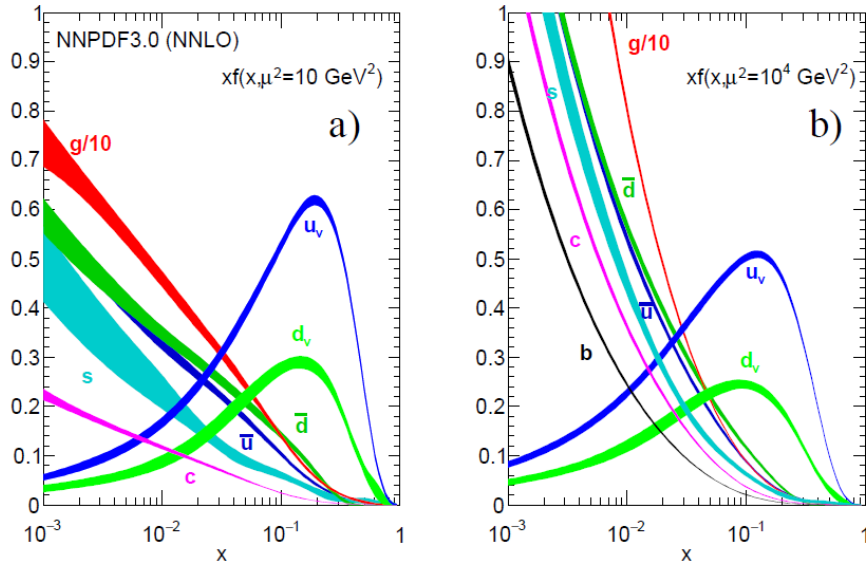

Figure 1.4: x times the unpolarised PDF $f(x)$ for the valence and sea quark and gluons in proton for scales $\mu^2 = 10$ (GeV/c)^2 and $\mu^2 = 10^4$ (GeV/c)^2 and $\alpha_s(M_Z^2) = 0.118$ [17].

1.2.2 The Spin structure of nucleon

"You think you understand something? Now add spin…"
Robert L. Jaffe

In the collinear approximation, the structure of the nucleon is reflected by the unpolarised parton distribution function reviewed above and the polarised PDF $g_1(x)$ which is called helicity function[4], as follows [7]:

$$g_1(x) \equiv \frac{1}{2}\sum_q e_q^2 \Delta f(x) = \frac{1}{2}\sum_q e_q^2 \left(\left(f_1^{q\uparrow\Uparrow}(x) + \bar{f}_1^{q\uparrow\Uparrow}(x) \right) - \left(f_1^{q\downarrow\Uparrow}(x) + \bar{f}_1^{q\downarrow\Uparrow}(x) \right) \right), \qquad (1.34)$$

---

[4] The helicity denotes the projection of the particle spin onto the direction of its momentum.

that denotes the difference between the density of quarks with spin parallel with respect to the longitudinally polarised hadron and the quarks with spin anti-parallel. The transversal structure described by the transversity function $h_1(x)$[5] which is analogous to $g_1(x)$, but for the transversely polarised hadrons.

We can determine the first moments of $g_1(x)$ function for proton and neutron:

$$\Gamma_1^{p,n} = \int_0^1 dx\, g_1^{p,n}(x) = \frac{1}{9}\left[\pm\frac{3}{4}a_3 + \frac{1}{4}a_8 + a_0\right],$$ (1.35)

where a_0, a_3, and a_8 are given:

$$a_0 = \left(\Delta u + \Delta \bar{u} + \Delta d + \Delta \bar{d} + \Delta s + \Delta \bar{s}\right) \equiv \Delta\Sigma,$$ (1.36)

$$a_3 = \left(\Delta u + \Delta \bar{u} - \Delta d - \Delta \bar{d}\right),$$ (1.37)

$$a_8 = \sqrt{\frac{1}{3}}\left(\Delta u + \Delta \bar{u} + \Delta d + \Delta \bar{d} - 2\left(\Delta s + \Delta \bar{s}\right)\right).$$ (1.38)

The a_3, and a_8 can be obtained from the hyperon β-decay. Using the known value of a_3 and a_8, the a_0 can be determined via measuring the Γ_1^p. In the 1988 the EMC collaboration provided the first measurement of Γ_1^p for a very wide range of x. The results are shown on figure 1.5 and the measured value was [1]:

$$\Gamma_1^p = 0.123 \pm 0.013(stat.) \pm 0.019(syst.).$$ (1.39)

With the reasonable assumption of neglecting the contribution of strange quark to the proton spin $\Delta s = \Delta \bar{s} = 0$ (on the basis of Elis-Jaffe sum rule, eq. (1.44)) also the contribution of valence quark spins to the spin of a proton, $\Delta\Sigma$ (ibid.):

$$\Delta\Sigma = a_0^{EMC} = 2\langle S_z \rangle_{u+d} = 0.120 \pm 0.094(stat.) \pm 0.226(syst.).$$ (1.40)

which was in contradiction with the naïve expectation as the 3-quark parton model assumes the nucleon as an ensemble of approximately free partons moving collinear with nucleon with no orbital angular moment, and the nucleon spin consisting only from the contribution of the 3 valence quarks and thus $\Delta\Sigma$ must equal 1 with two valence quarks with parallel spin and one with anti-parallel, ½ + ½ - ½ = ½. But the surprising results of EMC measurement, basically compatible with zero, brought a crisis to parton model known as a "spin crisis" and triggered new experimental and theoretical efforts for explaining the origin of the nucleon spin.

---

[5] The subscript 1 denotes the leading order of perturbative QCD. The notation we use is called the Amsterdam notation (Jaffe, Ji, and Mulders); one of the older notations which is also often used denotes $f(x) \equiv q(x)$, $g_1^q(x) \equiv \Delta q$, and $h_1^q(x) \equiv \Delta_\perp q(x)$.
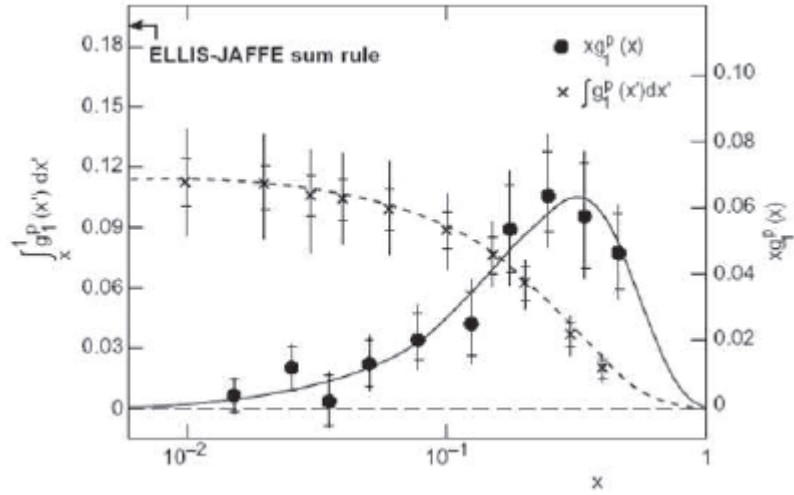
Figure 1.5: The $xg_1{}^p(x)$ (in circles) and $\Gamma_1{}^p$ (in crosses) measurement of the EMC collaboration in 1988 [1].

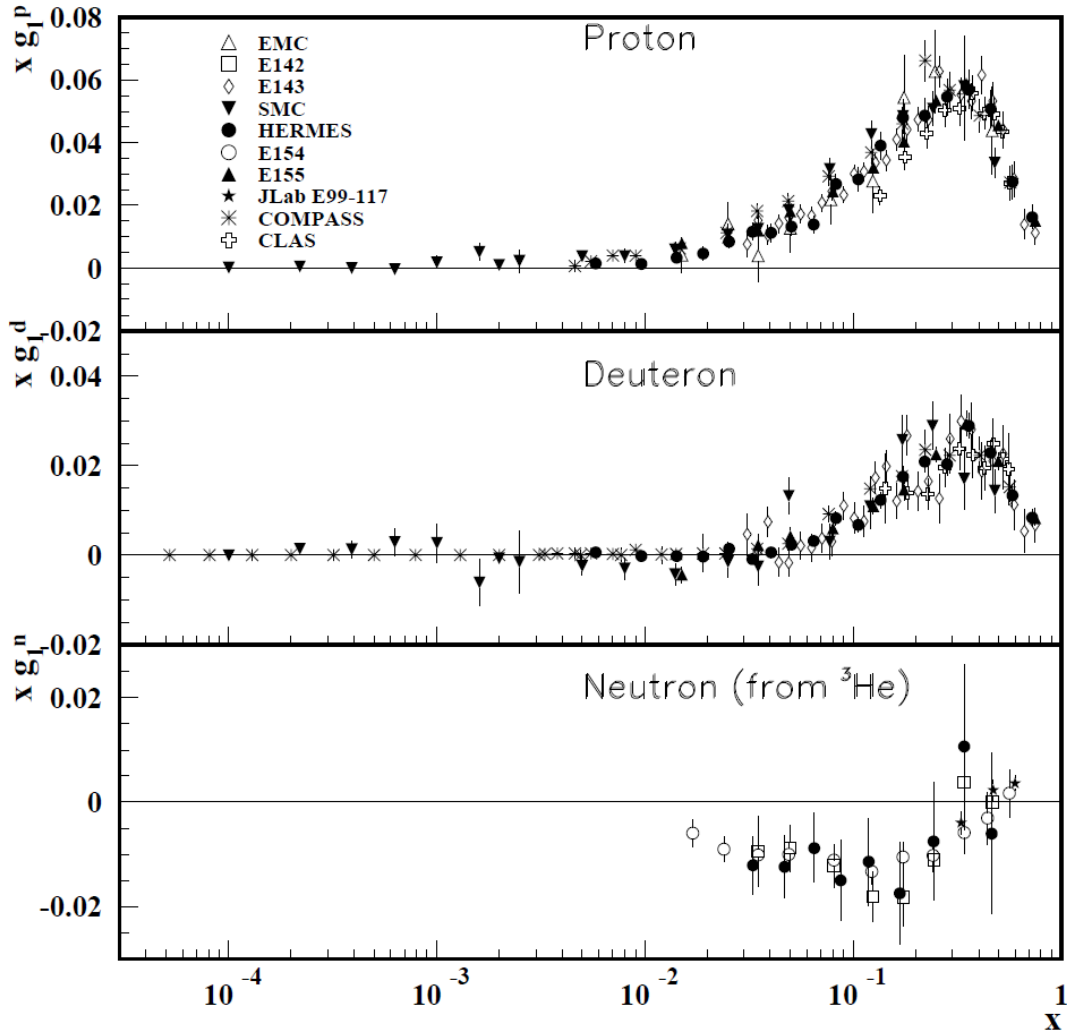

Figure 1.6: The spin dependent structure function $xg_1(x)$ of the proton, deuteron, and proton on varying energy scales from $0.3 - 100$ GeV/c^2. The figure was taken from ref. [17].

1.2.3 The QCD improvement of the parton model

The formulation of the QCD brought gluons as another type of partons in the nucleon and the presence of the gluon field explained the violation of the Bjorken scaling in high energies. Just to give a short overview, QCD is based on SU(3) symmetry of colour charges with eight massless and coloured field quanta, vector bosons called gluons. Gluons carry the colour charge (8 colours) which allows self-interaction. In the low energy under 1 GeVc the strong coupling $\alpha_s(Q^2)$ diverges which leads to confinement of the quarks and perturbative methods of the QCD are not valid. In the high energy the gluon radiation appears which causes the breaking of the Bjorken scaling, and in the limit of infinite energy (equivalent to distances going to zero) α_s goes to zero[6]. The Q^2-evolution of the parton distribution functions can be then derived perturbatively. With increasing the Q^2, the resolution of the probe increase as well. At high energies a valence quark appears to be surrounded by additional $q\bar{q}$ pairs, i.e. the sea quarks, and gluons. This is described by the splitting functions P_{qq}, P_{qg}, P_{gq}, and P_{gg}[7]. The Q^2 evolution of parton distribution function can be calculated by the DGLAP equations if they are known at a certain scale. The first moment of $g_1(x)$ can be then rewritten in Q^2-dependence [7]:

$$\Gamma_1^p\left(Q^2\right)=\int_0^1 dx g_1^p\left(x,Q^2\right)=\frac{1}{12}\left[\left(a_3+\frac{a_8}{\sqrt{3}}\right)E_{NS}\left(Q^2\right)+\frac{4}{3}a_0\left(Q^2\right)E_S\left(Q^2\right)\right], \qquad (1.41)$$

where the E_{NS} and E_S are the non-singlet and singlet coefficient functions are expansions of the running coupling $\alpha_s(Q^2)$:

$$E_{NS}\left(Q^2\right)=1-\frac{\alpha_s}{\pi}-\left(\begin{array}{c}3.58\\3.15\end{array}\right)\left(\frac{\alpha_s}{\pi}\right)^2-O\left(\left(\frac{\alpha_s}{\pi}\right)^3\right),$$

$$E_S\left(Q^2\right)=1-\frac{\alpha_s}{\pi}-\left(\begin{array}{c}1.10\\-0.07\end{array}\right)\left(\frac{\alpha_s}{\pi}\right)^2-O\left(\left(\frac{\alpha_s}{\pi}\right)^3\right), \qquad (1.42)$$

where the upper and the lower number in the parentheses represent a coefficient used if 3 or 4 quark flavours are considered, respectively. A fundamental sum rule can be derived by the means of QCD:

$$\Gamma_1^p\left(x\right)-\Gamma_1^n\left(x\right)=\frac{g_A}{6}E_{NS}\left(Q^2\right). \qquad (1.43)$$

This rule is called Bjorken sum rule and was first experimentally tested by EMC [1] and SMC [16] via measuring Γ_1^p and Γ_1^n, respectively. The importance of this result lies in the

---

[6] This phenomenon is called asymptotic freedom; Nobel prize: Politzer, Gross, Wilczek, 2004.

[7] These functions describe a probability of a parton (denoted by the first subscript) emitting a different parton (the latter subscript).

fact that it was not derived from the parton model and thus it can be then used for its confirmation. The measurements have shown consistent with the expectations, using the known value of a_3.

Using an assumption that $\Delta s = \Delta \bar{s} = 0$ then $a_0 = \sqrt{3}a_8$ from the eq. (1.36) and (1.38) and (1.41) turns to:

$$\Gamma_1^{p',n}(x) = \frac{1}{12}a_3\left(\pm 1 + \frac{5}{\sqrt{3}}\frac{a_8}{a_3}\right), \tag{1.44}$$

which is called the Ellis-Jaffe sum rule. The results of the Ellis-Jaffe sum rule verification are shown on fig. 1.5 together with the predicted value marked by an arrow [1]. As one can see there is a significant violation of Ellis-Jaffe sum rule implicating that the above assumption cannot be valid.
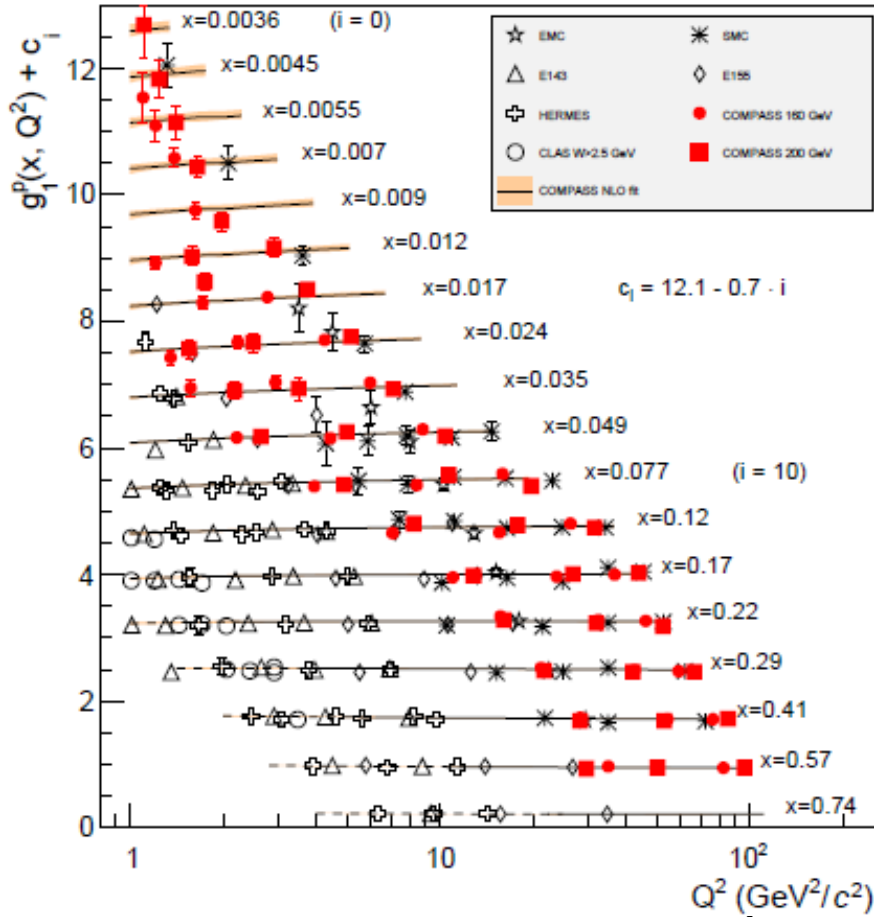

Figure 1.7: The world data on scaling of the g_1^p as a function of Q^2 and x. One can see the slight hint of Bjorken scaling violation for small x, however the Q^2 and x range of the data is smaller than the collected data for the structure function $F_2(x,Q^2)$ as can be seen on the fig. 1.2. The figure was taken from ref. [19].

The $\Gamma_1{}^p$ and the value of quark spin contribution $\Delta\Sigma$ and a_0 have been measured by many other experiments, one of the most recent result is from 2007 COMPASS μp DIS data [18]:

$$\Delta\Sigma^{COMPASS} = 0.32 \pm 0.03(stat.), \tag{1.45}$$

$$a_0{}^{COMPASS} = 0.33 \pm 0.03(stat.). \tag{1.46}$$

Both of the results are nearly identical, the latter was derived from the $\Gamma_1{}^d$ using the octet axial charge a_8. This value is rather higher but far from the original assumption.

As a result of the QCD corrections, the gluonic contribution to the nucleon spin is non-zero, the equality of a_0 and $\Delta\Sigma$ (eq. (1.36)) is no longer valid, it applies:

$$a_0 = \Delta\Sigma - 3\frac{\alpha(Q^2)}{\pi}\Delta G(Q^2), \tag{1.47}$$

where $\Delta G(Q^2) = G^{\uparrow\uparrow\uparrow}(x, Q^2) - G^{\downarrow\uparrow\uparrow}(x, Q^2)$ is the gluonic contribution to the spin of nucleon. Thus the small measured value of a_0 does not necessarily mean the $\Delta\Sigma$ is small.
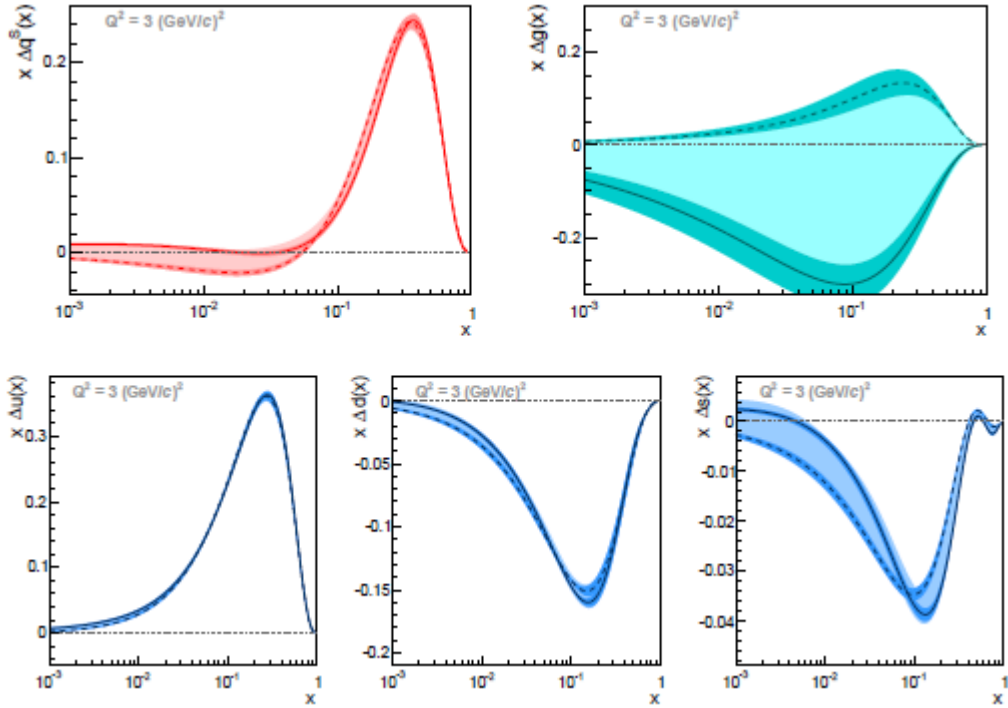

Figure 1.8: Results of the QCD fits to g_1 world data at a scale $\mu^2 = 3$ (GeV/c)^2 for singlet $x\Delta f^S(x)$ and gluon distribution $x\Delta g(x)$ (top band) and the distributions $x(\Delta f(x) - \Delta\bar{f}(x))$ for the flavours u,d, and s. The dark bands denotes the statistical errors and the light ones the systematic errors. The figure was taken from ref. [19].

The ΔG has been subject of various measurements, e.g. the COMPASS experiment which confirmed the non-zero value of $\Delta G(Q^2) = 0.2^{+0.06}_{-0.07}$ [20] but this contribution is still not sufficient. Contemporary experiments are ongoing for determining the last possible

contribution of quark and gluon orbital angular momentum to conclude the spin puzzle as is described in the Jaffe-Manohar sum rule [21]:

$$\frac{1}{2} = \frac{1}{2}\Delta\Sigma + \Delta G + L_q + L_g \,, \tag{1.48}$$

where L_q and L_g are the quark and gluon orbital angular momentum, respectively.

1.3 Transverse-spin-dependent nucleon structure

In the previous section we presented the results of the measured contribution of quark and gluon polarisation to the nucleon spin. All the remaining effect that creates the total nucleon spin has to be addressed to the orbital angular momentum of partons. The only possible way to access L_q and L_g are the transverse spin or momentum effects in the nucleon. In the past there had been a common assumption that in high energies the transverse-spin effects are suppressed. However, it is far from the truth, there is a difference between the polarisation itself and its measureable manifestation [22]. The problem is to find a process which is sensitive to the transverse-spin effects as they are often strongly suppressed. Transverse polarisation of quarks cannot be observed in the DIS but it is accessible by SIDIS and Drell-Yan processes.

Let us first explain the Jaffe-Ji-Mulders notation (also called the Amsterdam notation) we use for the PDFs and consequently the TMDs [22],[23]. The letters f, g, and h denote the unpolarised, the longitudinally polarised, and the transversely polarised PDFs, respectively. The subscript 1 stands for the leading-twist functions, and the subscripts L and T correspond to the longitudinally or transversally polarised parent nucleon. The superscript $\perp$ denotes the presence of the transverse momenta with the uncontracted Lorentz indices.

1.3.1 The Transversity distribution

It has been shown in the section 1.2 that there are 3 PDFs describing the structure of the nucleon in the collinear approximation, two of them has been already presented. The third PDF, the transversity distribution $h_1^q(x)$[8], is analogous to the helicity but applies for the transversely polarised hadrons and quarks. It describes the density of the transversely polarised quarks with the fraction of momentum x and spin parallel with the nucleon spin minus the density of quarks with spin antiparallel w.r.t. the transversely polarised nucleon [24].

$$h_1^q(x) = \left(\left(q^{\rightrightarrows}(x) + \overline{q}^{\rightrightarrows}(x) \right) - \left(q^{\leftrightarrows}(x) + \overline{q}^{\leftrightarrows}(x) \right) \right). \tag{1.49}$$

---

[8] The Q^2-dependence of the PFDs and TMDs is omitted for brevity.

Again, within the QCD improved Parton model the Q^2-dependence appears in order to renormalize the quark fields. Same as the f_1 and g_1 distributions, the h_1 is a leading twist quantity[9] thus there is no reason for the transversity to be smaller than the helicity. However, in the Q^2-evolution it is suppressed in low x range with respect to the helicity. Another distinction from the helicity is the non-existence of the transversal counterpart of the gluon polarisation which makes the overall contribution of the transversity lower than the helicity contribution. The transversity is connected with the helicity and unpolarised PDF by the Soffer's inequality [7] (for a particular quark flavour):

$$|h_1(x)| \le \frac{1}{2}[f_1(x) + g_1(x)]. \tag{1.50}$$

The transversity was introduced by Ralston and Soper in 1979 [27]. But more thorough theoretical efforts were developed in the '90s and first proposals for the measurements of the transversity were submitted. However, there is still very little data collected nowadays [22]. The reason is that $h_1(x)$ is a chiral-odd function thus its measurement requires a flip of the probed quark chirality. But as it has been mentioned above, this process cannot be accessed in the DIS due to the conservation of helicity in the QCD processes. To measure the transversity, one has to flip the chirality twice, so either two hadrons in initial state are needed, as in DY, or one hadron in the initial state and one in the final, like in SIDIS. The present measurements of the transversity are held in the COMPASS, JLab, or RHIC experiment (and a contribution from the past HERMES experiment data).

1.3.2 Transverse Momentum Dependent PDFs

If we abandon the collinear approximation and consider the transverse momentum of quarks k_T to be finite, we can expand the description of the nucleon structure to a 3D picture in the momentum space given by the Transverse Momentum Dependent (TMD) PDFs. Another approach using the finite k_T and developed in the 90' are the Generalised Parton Distribution (GPD) which describe a longitudinal momentum of partons and their radial position distribution, but those are not a subject of this thesis.

TMD approach is applicable only for small transverse momenta of partons $k_T << Q^2$ [22]. In the leading twist, 8 k_T-dependent time-reversal invariant TMDs emerge [22]: $f_1(x, k_T^2)$, $g_{1L}(x, k_T^2)$, $h_1(x, k_T^2)$, $g_{1T}(x, k_T^2)$, $h_{1T}^\perp(x, k_T^2)$, $h_{1L}^\perp(x, k_T^2)$, $h_1^\perp(x, k_T^2)$, and $f_{1T}^\perp(x, k_T^2)$. They are summarized in the figure 1.9. The first three TMDs integrated over k_T^2 give the already

---

[9] Twist t denotes for the order of the expansion of the cross-section (DY or SIDIS) proportional to $(1/Q)^{t-2}$.

discussed $f_1(x)$, $g_1(x)$, and $h_1(x)$ distributions. The other 5 TMDs are chiral-odd functions which vanish after the integration. The distribution $h_{1T}^{\perp}(x,\ k_T^2)$ is called the pretzelosity function; $g_{1T}(x,\ k_T^2)$ and $h_{1L}^{\perp}(x,\ k_T^2)$ are the worm-gear functions which correlate two perpendicular spin directions [24]. The two last functions, which arise if we don't demand the time-invariance of the amplitude, are the naively T-odd distributions, the Boer-Mulders function $h_1^{\perp}(x,\ k_T^2)$ and the Sivers function $f_{1T}^{\perp}(x,\ k_T^2)$. The Boer-Mulders distribution measures the correlation between the transversal spin and the k_T of the quarks within the unpolarised nucleon. The Sivers function together with the naïve T-reversal will be discussed in the following subsection.

Figure 1.9: The whole set of TMDs ordered by the nucleon polarisation versus the polarisation of quarks.

For further convenience, we mention the role of fragmentation functions (FF). In the hadron production processes (e.g., SIDIS) the transverse spin and k_T dependent structure functions consist of the TMDs and the FFs of the daughter hadrons. FFs are in a sense a mirror of the parton distributions as they represent the probability of a particular quark with a given polarisation to form a certain daughter hadron with the momentum fraction z in the process of hadronisation [22].

1.3.3 The Sivers distribution

As the QCD is a T-invariant theory, one might expect that the above introduced naively T-odd distributions are equal to zero. In the following subsection we will give a brief theoretical justification of the observed data which proof otherwise (e.g. the Sivers asymmetry results from SIDIS at COMPASS [26]), more details on the derivation of the relations below and the TMD factorization can be found e.g. in referencies [22],[27],[28]. In the second part

of the subsection, we give an outline of one of the naively *T*-odd distributions, the Sivers function. The other *T*-odd function, the Boer-Mulders will not be discussed as it was not a topic of our analysis.

The cross-section of the high-energy hadroproduction (e.g. DY) or leptoproduction (SIDIS) can be factorized into lepton part $L^{\mu\nu}$ and hadron part $W^{\mu\nu}$, as it was mentioned in the section 1.1. The soft part of the hadron tensor is represented by the quark-quark correlation matrix. The general form of the correlation matrix is [22]:

$$\Phi_{ij}(k,P,S)=\int d^4\xi e^{ik\cdot\xi}\langle PS|\psi_j(0)\mathcal{L}^\dagger(0,\infty)\mathcal{L}(\infty,\xi)\psi_i(\xi)|PS\rangle, \tag{1.51}$$

where $\mathcal{L}$ is a light-like gauge-link operator, path-ordered exponential, so-called Wilson line, inserted between the quarks to preserve the gauge invariance, defined as:

$$\mathcal{L}(y,\infty)=P\exp\left(-ig\int\limits_y^\infty ds_\mu A^\mu(s)\right), \tag{1.52}$$

where *y* is the initial time, and *g* is the coupling constant of a gluon gauge field A^μ. Then the quark distribution functions can be expressed as:

$$\mathrm{Tr}(\Gamma\Phi)=\int d^4\xi e^{ik\cdot\xi}\langle PS|\psi_j(0)\mathcal{L}^\dagger(0,\infty)\Gamma\mathcal{L}(\infty,\xi)\psi_i(\xi)|PS\rangle, \tag{1.53}$$

It is the presence of the Wilson lines which guarantees the non-vanishing of the *T*-odd distributions from the cross-section. Following symmetries apply for the quark-quark correlator matrix:

$$\Phi^+(k,P,S)=\gamma^0\Phi(k,P,S)\gamma^0 \qquad \text{(hermicity)} \tag{1.54}$$

$$P\Phi(k,P,S)=\gamma^0\Phi(\widetilde{k},\widetilde{P},-\widetilde{S})\gamma^0 \qquad \text{(parity)} \tag{1.55}$$

$$T\Phi(k,P,S)=\gamma^5 C\Phi(\widetilde{k},\widetilde{P},\widetilde{S})C^+\gamma^5 \quad \text{(time-reversal)} \tag{1.56}$$

The equation (1.56) can be applied only if the Wilson lines are not inserted. The correlator can be decomposed in a Dirac matrices basis in a following way:

$$\Phi(k,P,S)=\left\{S1+V_\mu\gamma^\mu+A\gamma^5\gamma^\mu+iP_5\gamma^5+\frac{1}{2}iT_{\mu\nu}\sigma^{\mu\nu}\gamma_5\right\}, \tag{1.57}$$

where *S*, *V*, *A*, *P*, and *T* are scalar, vector, axial, pseudo scalar, and tensor terms. After some treatment (see [22]) we get the form with the distribution functions:

$$\mathrm{Tr}(\gamma^\mu\Phi)=P_{q/N}(x,k_T^2)=f_1(x,k_T^2)+f_{1T}^\perp(x,k_T^2)\frac{[k_T\times\hat{S}_N]\cdot S_T}{M},$$

$$\mathrm{Tr}(\gamma^\mu\gamma^5\Phi)=P_{q/N}(x,k_T^2)s_L(x,k_T)=g_{1L}(x,k_T^2)S_L+g_{1T}(x,k_T^2)\frac{k_T\cdot S_T}{M},$$

$$\mathrm{Tr}(i\sigma^{\mu\nu}\gamma^5\Phi)=P_{q/N}(x,k_T^2)s_T(x,k_T)=h_{1T}(x,k_T^2)S_T+\left[h_{1L}^\perp(x,k_T^2)S_L+h_{1T}^\perp(x,k_T^2)\frac{k_T\cdot S_T}{M}\right]\frac{k_T}{M}+$$

$$+h_1^\perp(x,k_T^2)\frac{[k_T\times\hat{S}_N]}{M} \tag{1.58}$$

The function $P_{q/N}(x, k_T^2)$ represents generally the quark distribution functions, i.e. the probability to find a quark with nucleon momentum fraction x and with intrinsic transverse momentum k_T; $s_{L/T}$ denotes the longitudinal or transversal spin of the quark; the $S_{L/T}$ is the spin of the target nucleon with respect to nucleon momentum. The analogous relations apply for antiquarks as well (with the antiquark-antiquark correlator $\overline{\Phi}$). Then the unpolarised PDF is composed as an addition of f_1 for quarks and antiquarks $f_1 + \bar{f}_1$, i.e. the flavour singlet, and the rest of the 8 TMDs is a subtraction $f_1 - \bar{f}_1$, the flavour non-singlet [22]. The last terms of the relations $\text{Tr}(\gamma^\mu \Phi)$ and $\text{Tr}(i\sigma^{\mu\nu}\gamma^5 \Phi)$ in equations (1.58) appear only if the condition (1.56) is not applied.

Finally, we can explain why the constraint (1.56) is "naïve" and why T-invariance of the correlator (1.51) is preserved. The link operator presented above (eq. (1.52)) is a representation of a final-state interaction (in the eikonal approximation, see [29][30]) between the struck quark and the remnant of the nucleon. It is integrated from the time y to the future. On the other hand, under the time-reversal the future-pointing Wilson lines are flipped into the past-pointing ones, thus representing the initial-state interaction. This is the reason why it is naïve to assume that the eq. (1.56) is the appropriate form of the T-reversal valid for the correlator (1.51). This was the Collins's argument [29] based on QCD of non-vanishing of the T-odd distributions, as they are actually *not T*-odd, but *naively T*-odd. The requirement of the gauge invariance caused the presence of the Wilson lines, and thus not the classic T-reversal, but a naïve one have to be used to preserve the T-invariance of the correlator. As a consequence of the Wilson lines application, the discussed distributions appear to be T-odd under a classic T-reversal. Another consequence is the process dependence of the correlator incorporated into the Wilson lines which change their sign when applied in the initial state interaction versus the final ones due to the switching of the direction of integration.

One of the T-odd functions is the Sivers distribution $f_{1T}^\perp$. It was introduced by Dennis W. Sivers in 1990 [31] in order to explain the large single-spin asymmetries measured in 70's in DIS. Sivers function describes the correlation of the transverse spin S_T of the nucleon with the intrinsic transverse momentum k_T of the quark, in other words it describes the left-right asymmetry in the distribution of partons in the nucleon with respect to the plane spanned by the directions of momentum and spin of the nucleon. A correlation between the k_T and the transverse polarisation of a hadron is related to the non-zero orbital angular momentum in the

nucleon. The non-zero value of the Sivers distribution was shown experimentally by the HERMES [32] and COMPASS [26].

The Sivers asymmetry was measured at COMPASS in production of charged pions, kaons, and neutral kaons in SIDIS. Recently, new analysis of the COMPASS data from 2007 and 2010 was issued [26] showing the Sivers asymmetry summed up for the positive hadrons and the negative ones in four Q^2 ranges which are almost identical as the ones used in the recent DY analysis [35] to enable the direct comparison of the Sivers asymmetry results, measured by COMPASS in the SIDIS and DY processes. The complete results for the four Q^2 ranges are shown in figure 1.10 [26].
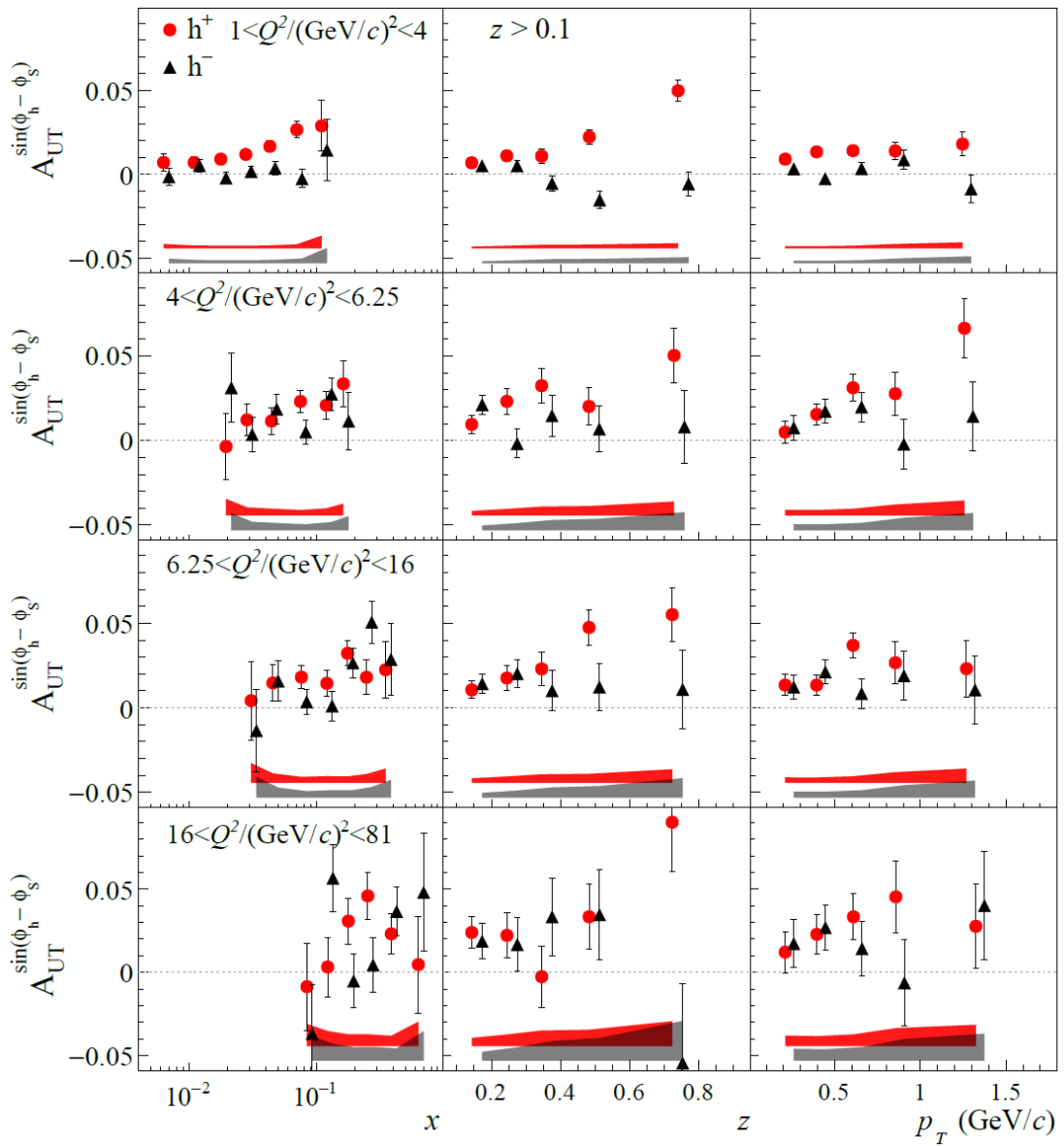
Figure 1.10: The Sivers asymmetries from COMPASS for the positive and negative hadrons as function of x, z, and p_T^h (taken from ref. [26]) in four different Q^2 ranges.

One can see that for positive hadrons, positive Sivers asymmetry was observed in the whole x-interval in all four mass ranges [26]. The amplitude is apparently rising to the value of $x \sim 0.2$ and then possibly decreasing for larger x. The Sivers asymmetry in z and p_T^h seem to have approximately linear dependence. The data for the negative hadrons show lower amplitude and for the lower Q^2 ranges is rather compatible with zero, except for the low Q^2 in the z distribution where it drops to the negative values, while in the high mass range there is an indication for a slight rise in the positive values. The integrated values of the complete set of the cross-section amplitudes are depicted in the figure 1.11.
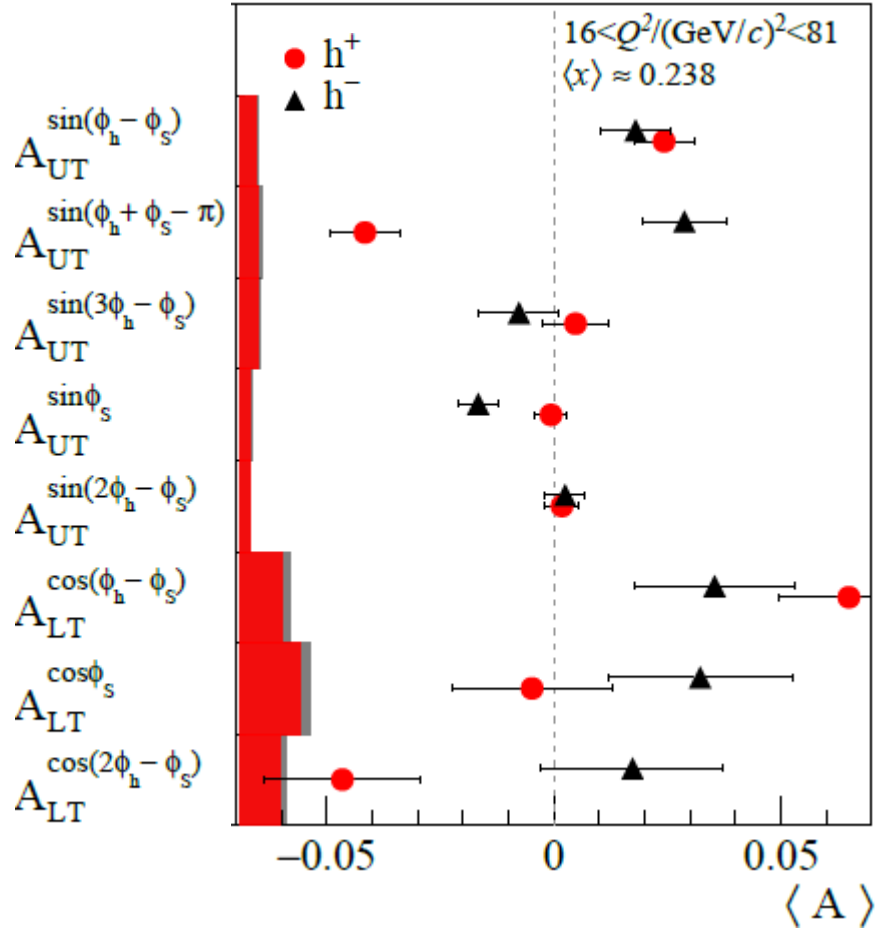
Figure 1.11: The integrated transverse-spin asymmetries (TSA) in the high Q^2 range. Systematic errors are shown as the horizontal bars. The first is the Sivers asymmetry, the second is the transversity asymmetry, and the third the pretzelosity asymmetry (the remaining modulation amplitudes are mostly of higher twist origin and are not the subject of this thesis). Taken from ref. [26].

1.3.4 The Pretzelosity distribution

The pretzelosity function $h_{1T}^\perp(x, k_T^2)$ is a chiral-odd TMD which describes a correlation between the transverse spin of the nucleon with a transverse spin and k_T of a quark. It is

predicted to be suppressed compared to f_1 in large and small x. There is a constraint on a value of pretzelosity after integration over the k_T given by an inequality [33]:

$$\left|h_{1T}^{\perp(1)}(x)\right| \le \frac{1}{2}\left(f_1(x) - g_1(x)\right) \le f_1(x).$$ (1.59)

In a sense, the pretzelosity measures a deviation of the nucleon shape from a sphere. And similarly, like transversity, it has no analogy for gluons.

1.4 The Drell-Yan process

In this section we will give a short review of the DY formalism and observables (used notation follows the article of Arnold, Metz, and Schlegel [34]). The Drell-Yan process was first introduced in 1970 by Sidney D. Drell and Tung-Mow Yan [35]. It is a process of hadron-hadron reaction (in the leading order, the reaction proceeds via quark-antiquark annihilation) with a production of a massive lepton pair:

$$H_a(P_a) + H_b(P_b, S_b) \to \gamma^*(q) + X \to l^-(k,s) + l^+(k',s') + X,$$ (1.60)

where $P_{a,b}$ are the momenta of the colliding hadrons; S_b denote the spin of the target hadron (considering only the polarised target as in the case of COMPASS measurement), which have the following properties: $S_p \cdot P_p = 0$ and $S_p^2 = -1$; k and k' are the momenta of leptons; and s and s' their spins. $q = k + k'$ is the total momentum of the lepton pair, or equivalently, of the virtual photon γ^*. And X denotes the hadron shower created from the remnants of the struck initial hadrons. The figure 1.12 shows the Feynman diagram of this process:
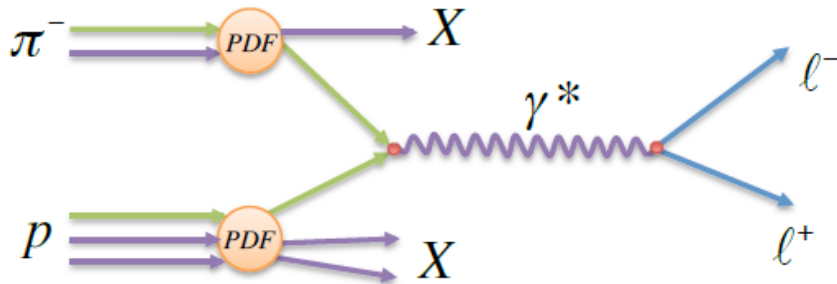
Figure 1.12: The Feynman leading order diagram of the Drell-Yan process: annihilation of a quark-antiquark pair into a lepton pair. The circles denote the PDFs of the hadrons. The colliding hadrons are π^- and p such as at COMPASS experiment (taken from ref. [24]).

We assume a reference frame of hadron-hadron collision head-on along the z axis. The following invariant kinematic variables can be defined:

$$s = (P_a + P_b)^2,$$

$$x_{a,b} = \frac{q^2}{(2P_{a,b}q)},$$

25

$$x_F = x_a - x_b \cong \frac{2q}{\sqrt{s}}, \qquad (1.61)$$

$$\tau = \frac{4m^2}{s},$$

$$M_{ll}^2 = Q^2 = q^2 \cong s x_a x_b,$$

where s describes the total CMS energy squared, x is the Bjorken x of a parton in hadron (see eq. (1.4)), x_F denotes the so-called Feynman variable, and the last quantity is the invariant mass squared of the dilepton. The equalities in the second and last equation apply only if we neglect the parton masses. The cross-section of the unpolarised case using the parton model is given [4]:

$$\frac{d\sigma}{dm^2 dx_F} = \frac{1}{3}\left[\frac{4\pi\alpha^2}{3m^2}\right] \sum_i e_i^2 \iint f_{1i}(x_a) \bar{f}_{1i}(x_b) \delta(x_a x_b s - m^2) \delta(x_a - x_b - x_F) dx_a dx_b, \qquad (1.62)$$

where the expression in the square brackets stands for the parton-antiparton annihilation cross-section. The factor of ⅓ is a colour factor and reflects the probability that both quark and antiquark have the same colour charge, i.e. colour-anticolour, which is necessary for annihilation into a colourless photon. The index i runs over both quarks and antiquarks from the hadrons a and b. After the integration of (1.62) over x_2 from the eq. (1.63) by means of the second δ-function we get:

$$\frac{m^3 d\sigma}{dm dx_F} = \frac{8\pi\alpha^2}{9\sqrt{x_F^2 + \tau}}\left[\sum_i e_i^2 f_{1i}(x_1) \bar{f}_{1i}(x_2)\right], \quad x_{1,2} = \frac{1}{2}\left(\pm x_F + \sqrt{x_F^2 - \tau}\right). \qquad (1.63)$$

The r. h. s. of the eq. (1.63) scales with the parameter τ independently on the particular shape of the quark PDFs [4]. This is another example of scaling behaviour of the parton model as we could see in DIS (see fig. 1.2 and 1.7).

Along with the DIS, the unpolarised DY process played an important role in testing of the Parton model. However, unlike the DIS, the DY enables to determine the PDFs of pions and kaons, and its polarised version has proven [36] to be a convenient tool for studying the transversity distribution and T-odd TMDs (see Section 1.3) and some other issues both in perturbative and non-perturbative QCD. Nevertheless, the measurement of the polarised DY is rather demanding because of its very low total cross-section [34].

The complete cross-section of the Drell-Yan process containing the polarised part was derived by Arnold, Metz, and Schlegel [34]. In their article, two special reference frames are used: the first is called Collins-Soper (CS) frame depicted in the figure 1.13a. It is a dilepton (or equivalently virtual photon) CMS frame, the z-axis corresponds to the bisector between the directions of the beam and target particle momenta, the x-axis is located on the plane

26

spanned between the two momenta, and the *y*-axis is perpendicular to both of them in a right-handed direction [24]. If we neglect the lepton mass, we can write the l and $\bar{l}$ momenta as follows [37]:

$$l^-_{CS} = \frac{k}{2}\left(1, \sin\theta\cos\phi, \sin\theta\sin\phi, \cos\theta\right), \tag{1.64}$$

$$l^+_{CS} = \frac{k'}{2}\left(1, -\sin\theta\cos\phi, -\sin\theta\sin\phi, -\cos\theta\right). \tag{1.65}$$

The second is a target frame (TF) shown in the figure 1.13b where the *z*-axis is defined in the beam momentum direction, the *x*-axis along the transverse component q_T of the dilepton (or virtual photon) momentum q, and $\hat{y} = \hat{z} \times \hat{x}$, yielding:

$$P^\mu_{a,TF} = \left(P^0_{a,TF}, 0, 0, P^3_{a,TF}\right), \tag{1.66}$$

$$P^\mu_{b,TF} = \left(M_b, 0, 0, 0\right), \tag{1.67}$$

$$q^\mu_{TF} = \left(q^0_{TF}, 0, 0, q^3_{TF}\right), \tag{1.68}$$

$$S^\mu_{TF} = \left(0, S_T\cos\phi_S, S_T\sin\phi_S, S_L\right), \tag{1.69}$$

where *a* and *b* denote the beam and the target hadron, respectively. The angles present in the equations above are following: the ϕ_s angle which is an azimuthal angle of the transverse polarisation in the TF; and the ϕ and θ angles which denote the azimuthal and polar angle in the CS, respectively.
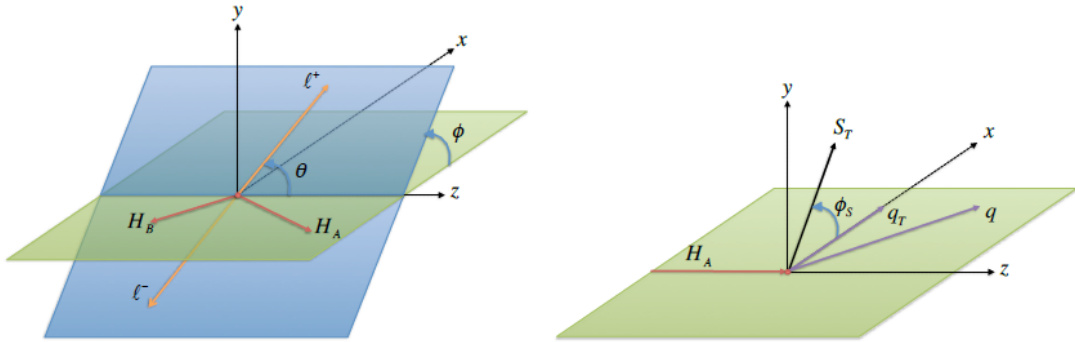
(a) The Collins-Soper frame. Definition of polar and azimuthal angles θ and Φ.

(b) Target rest frame. The definition of the azimuthal angle Φ_S of the proton spin.

Figure 1.13: Definition of the angles from Collins-Soper reference frame used for DY. (taken from ref. [24]).

If we assume the QCD TMD factorization theorem [34], it was shown that at the limit of high energies ($s, q^2 \gg M_a^2, M_b^2$) and low transverse momentum ($q_T \ll q$) the cross-section can be expressed as a sum of weighted convolutions of TMDs. We will use the following shorthand [34]:

$$C[w(k_{aT},k_{bT})f_1f_2]=\frac{1}{N_c}\sum_i e_i^2\int\delta^{(2)}(q_T-k_{aT}-k_{bT})w(k_{aT},k_{bT})$$
$$\times\left[f_1^i(x_a,k_{aT}^2)\bar{f}_2^i(x_b,k_{bT}^2)+\bar{f}_1^i(x_a,k_{aT}^2)f_2^i(x_b,k_{bT}^2)\right]d^2k_{aT}d^2k_{bT} \tag{1.70}$$

where w is a kinematic factor, the N_c is a number of colours and $f_i(x, k_T^2)$ are the TMDs. For the full form of the DY cross-section see ref. [27] (for its full derivation), or ref. [34]. Here, we are interested only in the case of transversely polarised target and beam hadron unpolarised as will be elaborated below. Let us also assume for further convenience the beam hadron a as π^- and the target hadron b as proton. Thus, we get a following formula [34][37]:

$$\frac{d\sigma}{d^4qd\Omega}=\frac{\alpha^2}{Fq^2}\hat{\sigma}_U\left\{\left(1+A_U^1\cos^2\theta+\sin2\theta A_U^{\cos\phi}\cos\phi+\sin^2\theta A_U^{\cos2\phi}\cos2\phi\right)\right.$$
$$\pm|\vec{S}_T|\left[\left(A_T^{\sin\phi_S}+\cos^2\theta\widetilde{A}_T^{\sin\phi_S}\right)\sin\phi_S+\sin2\theta\left(A_T^{\sin(\phi+\phi_S)}\sin(\phi+\phi_S)\right.\right.$$
$$+A_T^{\sin(\phi-\phi_S)}\sin(\phi-\phi_S)\right)+\sin^2\theta\left(A_T^{\sin(2\phi+\phi_S)}\sin(2\phi+\phi_S)+\right.$$
$$\left.\left.\left.+A_T^{\sin(2\phi-\phi_S)}\sin(2\phi-\phi_S)\right)\right]\right\} \tag{1.71}$$

where $F=4\sqrt{(p_a\cdot p_b)^2-M_a^2M_b^2}$ denotes the flux of incoming particles; α is the fine structure constant; $\hat{\sigma}_U=(F_1+F_2)$ is the unpolarised part of cross-section, which does not depend on the azimuthal angles ϕ_s and ϕ, factorised out of the cross section (F_1 and F_2 are the unpolarised structure functions discussed in the section 1.2.1); and $A_{U(T)}^{w(\phi,\phi_s)}=\dfrac{F_{U(T)}^{w(\phi,\phi_s)}}{\hat{\sigma}_U}$ are the measured amplitudes of the modulations of the azimuthal angles where the superscript stands for the azimuthal modulation which is described by the structure function and the subscript U, L, or T for unpolarised, longitudinally, or transversely polarised target proton, respectively (beam pions are taken as unpolarised, hence the subscript U is omitted). Now, it is convenient to introduce the depolarisation factors $D_{f(\theta)}=\dfrac{f(\theta)}{\left[1+A_U^1\cos^2\theta\right]}$ to isolate the azimuthal modulations in the braces (the factor $\hat{\sigma}_U(1+A_U^1\cos^2\theta)$ is the only surviving term which after integrating over the azimuthal angles ϕ_s and ϕ). Then we get:

$$\frac{d\sigma}{d^4qd\Omega}=\frac{\alpha^2}{Fq^2}\hat{\sigma}_U\left[1+A_U^1\cos^2\theta\right]\left\{\left(1+D_{[\sin2\theta]}A_U^{\cos\phi}\cos\phi+D_{[\sin^2\theta]}A_U^{\cos2\phi}\cos2\phi\right)\right.$$
$$\pm|\vec{S}_T|\left[\left(D_{[1]}A_T^{\sin\phi_S}+D_{[\cos^2\theta]}\widetilde{A}_T^{\sin\phi_S}\right)\sin\phi_S+D_{[\sin2\theta]}\left(A_T^{\sin(\phi+\phi_S)}\sin(\phi+\phi_S)\right.\right.$$
$$+A_T^{\sin(\phi-\phi_S)}\sin(\phi-\phi_S)\right)+D_{[\sin^2\theta]}\left(A_T^{\sin(2\phi+\phi_S)}\sin(2\phi+\phi_S)+\right.$$
$$\left.\left.\left.+A_T^{\sin(2\phi-\phi_S)}\sin(2\phi-\phi_S)\right)\right]\right\} \tag{1.72}$$

Finally, in the leading order QCD the cross-section simplifies [37] as some of the amplitude are of higher twist order, as follows:

$$\frac{d\sigma}{d^4qd\Omega} \overset{LO}{=} \frac{\alpha^2}{Fq^2}\hat{\sigma}_U \left[1+\cos^2\theta\right]\left\{\left(1+D_{[\sin^2\theta]}A_U^{\cos2\phi}\cos2\phi\right)\right.$$
$$+\left|\vec{S}_T\right|\left[A_T^{\sin\phi_S}\sin\phi_S + D_{[\sin^2\theta]}\left(A_T^{\sin(2\phi+\phi_S)}\sin(2\phi+\phi_S)\right.\right. \tag{1.73}$$
$$\left.\left.\left.+A_T^{\sin(2\phi-\phi_S)}\sin(2\phi-\phi_S)\right)\right]\right\}$$

As the $A_U^1 \overset{LO}{=} 1$ and $F_U^2 \overset{LO}{=} 0$, the non-vanishing asymmetries at LO are given as the fractions of the corresponding structure functions to the unpolarised structure function $F_U^1 \overset{LO}{=} C\left[f_1\bar{f}_1\right]$ [38]:

$$A_U^{\cos2\phi} \overset{LO}{=} \frac{F_U^{\cos2\phi}}{F_U^1} = C\left[\frac{2\left(\vec{h}.\vec{k}_{\pi T}\right)\left(\vec{h}.\vec{k}_{pT}\right)-\vec{k}_{\pi T}.\vec{k}_{pT}}{M_\pi M_p F_U^1}h_1^\perp\bar{h}_1^\perp\right], \tag{1.74}$$

$$A_U^{\sin\phi_S} \overset{LO}{=} \widetilde{A}_U^{\sin\phi_S} = \frac{F_T^1}{F_U^1} = C\left[\frac{\vec{h}.\vec{k}_{pT}}{M_p F_U^1}f_1\bar{f}_{1T}^\perp\right], \tag{1.75}$$

$$A_T^{\sin(2\phi+\phi_S)} \overset{LO}{=} \frac{F_T^{\sin(2\phi+\phi_S)}}{2F_U^1} = -C\left[\frac{2\left(\vec{h}.\vec{k}_{pT}\right)\left[2\left(\vec{h}.\vec{k}_{\pi T}\right)\left(\vec{h}.\vec{k}_{pT}\right)-\vec{k}_{\pi T}.\vec{k}_{pT}\right]-k_{pT}^2\left(\vec{h}.\vec{k}_{\pi T}\right)}{4M_\pi M_p^2 F_U^1}h_1^\perp\bar{h}_{1T}^\perp\right], \tag{1.76}$$

$$A_T^{\sin(2\phi-\phi_S)} \overset{LO}{=} \frac{F_T^{\sin(2\phi-\phi_S)}}{2F_U^1} = -C\left[\frac{\vec{h}.\vec{k}_{\pi T}}{2M_\pi F_U^1}h_1^\perp\bar{h}_1\right], \tag{1.77}$$

where $\vec{h} = \vec{q}_T/q_T$ is the unite vector of dilepton (virtual photon) transverse momentum. As one can see from the eq. (1.74)-(1.77), the following TMDs can be extracted from the measurement with the transversely polarised target:

➢ $A_U^{\cos2\Phi}$ gives access to the Boer-Mulders function of the pion beam,

➢ $A_U^{\sin\Phi_S}$ leads to the Sivers function of the target proton,

➢ $A_T^{\sin(2\Phi+\Phi_S)}$ to the Boer-Mulders function of the beam pion and to pretzelosity function $h_{1T}^\perp$ of the target proton,

➢ $A_T^{\sin(2\Phi-\Phi_S)}$ to the Boer-Mulders function of the beam pion and to the transversity function h_1 of the target proton.

Beyond the LO more asymmetries emerge, however within the QCD TMDs approach they remain kinematic corrections of higher twist (for higher twist asymmetries, see [34]).

The extraction of the convoluted parton distributions from the structure functions is done by the QCD TMD factorization theorem [34] which can only be applied under a condition of sufficiently large mass of produced leptons. This is why the majority of experiments use muons on the final state. This is the case of the COMPASS DY program and other present or future experiments, such as RHIC, SeaQuest (E906, 2012-2017) and its upgrade E1039 (after

2018) at Fermilab [39], J-PARC (after 2019), NICA (2020 or later), PANDA at FAIR (2025 or later) or IHEP [5]. The uniqueness of the COMPASS experiment lies in that it provides also measurements of SIDIS using mostly the same setup as for DY under minimal uncertainties of TMD evolution in the comparison of the Sivers TMD PDFs when extracted from these two measurements.

The DY reaction studied at COMPASS is following:

$$\pi^-(P_\pi) + p(P_p, S_p) \rightarrow \gamma^*(q) + X \rightarrow \mu^-(l) + \mu^+(l') + X, \tag{1.78}$$

with transversely polarised proton (NH$_3$) target as will be described in the Chapter 2.

1.5 The SIDIS process

The SIDIS process is lepton scattering off a nucleon (here we consider proton) with the production of a hadron in the final state as shows the eq. (1.79). We will consider the fully polarised case where the lepton beam and the target are polarised:

$$l(k, \lambda) + p(P_p, S_p) \rightarrow l'(k', \lambda') + h(P_h) + X, \tag{1.79}$$

where l and l' are the incoming and scattered lepton, respectively, k and k' are their four-momenta, and λ and λ' denote their helicities; p is the target proton with a four-momentum P_p and polarization S_p (either longitudinally, or transversely); h is the final identified hadron with the four-momentum P_h; and X is the unmeasured final hadron system.
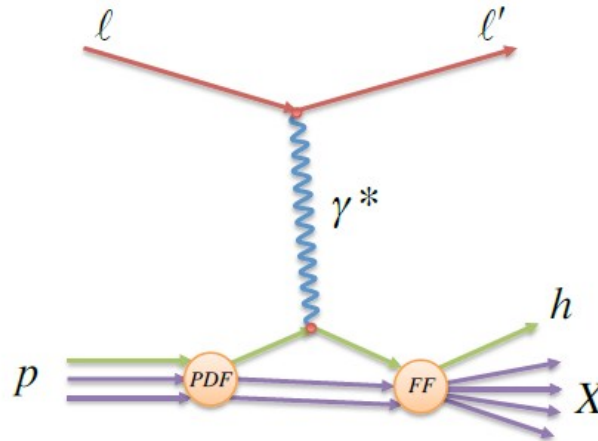

Figure 1.14: SIDIS process. Taken from ref. [24].

There are two additional kinematical variables used (except from the eq. (1.2)-(1.6)) which have to be defined before we proceed to the cross-section [9]:

$$z = \frac{P_p \cdot P_h}{P_p \cdot q}, \tag{1.80}$$

$$\gamma = \frac{2Mx}{Q}, \tag{1.81}$$

where q is the virtual photon four-momentum. The reference frame used in SIDIS is depicted in figure 1.15, however this process is not a topic of this thesis so the deatils will not be elaborated.
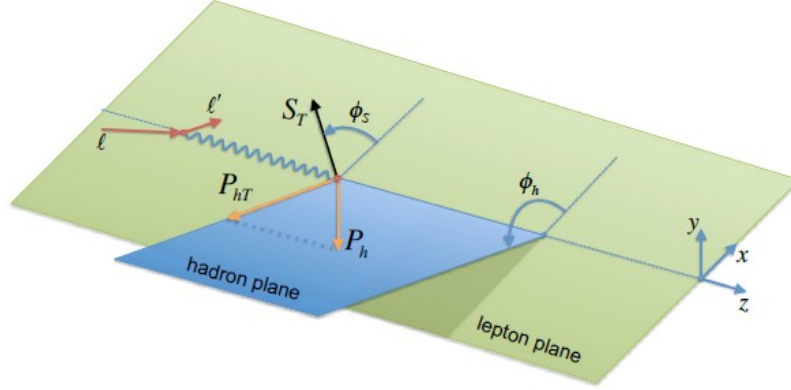

Figure 1.15: The definition of the azimuthal angles ϕ and ϕ_h for SIDIS reference frame (taken from ref. [24]).

In order to have a possibility of direct comparison with the DY asymmetries, one needs only the LO QCD limit and considering only the transversely polarised target and unpolarised lepton beam, thus the cross-section is given in the following simple form (derived in [40]):

$$
\frac{d\sigma}{dx\,dy\,dz\,d\psi\,d\phi_h\,dP_{hT}^2} \overset{LO}{=} \frac{\alpha^2}{xyQ^2}\frac{y^2}{2(1-\varepsilon)}\left(1+\frac{\gamma^2}{2x}\right)\left(F_{UU,T}+\varepsilon F_{UU,L}\right)\times
$$
$$
\left\{1+\varepsilon\cos(2\phi_h)A_{UU}^{\cos(2\phi_h)}\right.
$$
$$
\left.+S_T\left[\begin{array}{l}\sin(\phi_h-\phi_S)A_{UT}^{\sin(\phi_h-\phi_S)}\\ +\varepsilon\sin(\phi_h+\phi_S-\pi)A_{UT}^{\sin(\phi_h+\phi_S-\pi)}+\varepsilon\sin(3\phi_h-\phi_S)A_{UT}^{\sin(3\phi_h-\phi_S)}\end{array}\right]\right\} \qquad (1.82)
$$

where x, y, and z were introduced in eq. (1.4), (1.5) and (1.80); the ε is the ratio of the longitudinally versus transversally polarised beam flux; and $A_{P_1P_2}^{w(\phi_h,\phi_s)}=\dfrac{F_{P_1P_2}^{w(\phi_h,\phi_s)}}{F_{UU,T}+F_{UU,L}}$ is the definition of the asymmetries where P_1 and P_2 represent the polarisation (U, L, T) of the beam and the target, respectively. For the full description of all the involved asymmetries, see [40].

In the previous section we saw that DY asymmetries are convolutions of two PDFs of the beam hadron and the target hadron, on the other hand, in SIDIS the asymmetries are given as convolutions of PDFs of the target nucleon with the fragmentation functions of final hadron h. Hence, the asymmetries in the eq. (1.83) are defined as follows:

$$
A_{UU}^{\cos(2\phi_h)} \propto \frac{C\left[h_1^\perp H_1^\perp\right]}{F_{UU,T}+F_{UU,L}}, \qquad (1.83)
$$

$$
A_{UT}^{\sin(\phi_h-\phi_S)} \propto \frac{C\left[f_{1T}^\perp D_1\right]}{F_{UU,T}+F_{UU,L}}, \qquad (1.84)
$$

$$A_{UT}^{\sin(\phi_h + \phi_S - \pi)} \propto \frac{C\left[h_1 H_1^\perp\right]}{F_{UU,T} + F_{UU,L}}, \tag{1.85}$$

$$A_{UT}^{\sin(3\phi_h - \phi_S)} \propto \frac{C\left[h_{1T}^\perp H_1^\perp\right]}{F_{UU,T} + F_{UU,L}}, \tag{1.86}$$

where $H_1^\perp$ and D_1 are the Collins fragmentation function for the polarised final hadron and unpolarised fragmentation function, respectively [24]. The indices of the structure functions denote the polarisation of the beam, the target, and the virtual photon, respectively. And the unpolarised structure function $F_{UU,T} = C[f_1 D_1], F_{UU,L} = 0$.

1.6 The Sign change of *T*-odd TMDs

The problematics of *T*-odd TMDs was described in the section 1.3.3. The gauge-link operator $\mathcal{L}$ flips the direction of integration under the time-reversal and thus, practically, reverse the interaction from final-state interaction to initial-state one. Hence, as a consequence this operator makes the *T*-odd TMDs (Sivers and Boer-Mulders) process-dependent [36]. It was theoretically shown that the Sivers function $f_{1T}^\perp$ and the Boer-Mulders $h_1^\perp$ extracted from the DY process [36] should reverse its sign with respect to those obtained from SIDIS process [41] by Brodsky et al. Sign change was also proven by Collins in 2002 [29]. The underlying process in SIDIS is a final-state interaction where a gluon exchange takes place between the struck quark and the nucleon remnant, while initial-state interaction is the case in DY where the gluon is exchanged between the incoming quark in the projectile hadron and the target spectator quark system. Sign change of the *T*-odd distributions fundamental QCD prediction is a crucial test for the TMD approach:

$$f_{1T}^\perp(DY) = -f_{1T}^\perp(SIDIS) \quad h_1^\perp(DY) = -h_1^\perp(SIDIS). \tag{1.87}$$

It is contemporary a subject of experimental tests, such as in DY and SIDIS measurement at COMPASS experiment. The measurements are a test of the universality of the *T*-even TMDs[10] and the restricted universality of the *T*-odd ones [29].

---

[10] Universality is the process independence of these functions. It allows them to be measured in a limited set of interactions and predict their results in different processes.

2. COMPASS experiment at CERN

In the following section we will give a brief overview on the COMPASS spectrometer, data acquisition system, and the setup for DY measurement with the emphasis on the polarised target. For more technical detail on the spectrometer see [42],[37].

The original idea for establishing the COMPASS experiment came up in 1995. Two different groups had distinctive physical projects, first on hadron spectroscopy with a hadron beam, and the other on nucleon structure with a muon beam. These two groups could be unified due to the versatility of the former SMC beamline which could in principle support both the hadron and the muon beam. Thus, in 1997 the COMPASS experiment for studying a hadron spectroscopy and a nucleon structure was approved by CERN. The data taking (measuring of (SI)DIS with muon beam and hadron spectroscopy) ran since 2002 till the shutdown of CERN accelerators in 2005. Afterwards the experiment underwent some modifications, namely installation of the new polarisation magnet for the target [9] and the RichWall detector and new measurements of hadron spectroscopy took place together with the short DY test run in 2009 followed by the SIDIS in 2010-11 (see the obtained results for the Sivers asymmetry in Section 1.3.3). In 2010 the second phase of the experiment COMPASS-II was approved [37] and began data taking in 2012 with the Primakoff effect measurements and Deep Virtual Compton Scattering (DVCS) pilot run followed by two years of long shutdown. Then there were two years of DY data taking (specifics of this measurements will elaborated in the Section 3), and in 2016 and 2017 the DVCS measurement was going on. An additional measurement of DY in 2018 is planned. For the future years, the proposal is being prepared for the years after next long shutdown.

2.1 General outline of the spectrometer

The COMPASS experiment is located in the hall 888 in the CERN Prèvessin site as a descendant of the experiments EMC or SMC. It is a fixed target experiment placed on the M2 beam line which provides tertiary muon or secondary hadron beams with momenta $160 - 200$ GeV/c^2 and $120 - 280$ GeV/c^2, respectively [42], using the primary proton beam from the SPS accelerator (Super Proton Synchrotron). The secondary hadron beam is produced on the T6 beryllium target which is placed about 1 km upstream from the experimental hall. Then the requested beam is obtained simply by selecting the right momentum and charge by the bending magnets, and the corresponding beam radius is achieved by the focusing quadrupole

magnets in the M2 beam line. The beam extraction takes place during a so-called spill which lasts between 5 and 10 seconds. The whole spill period together with a longer period without beam for COMPASS[11] (mostly 30 to 40 seconds) is called a supercycle.
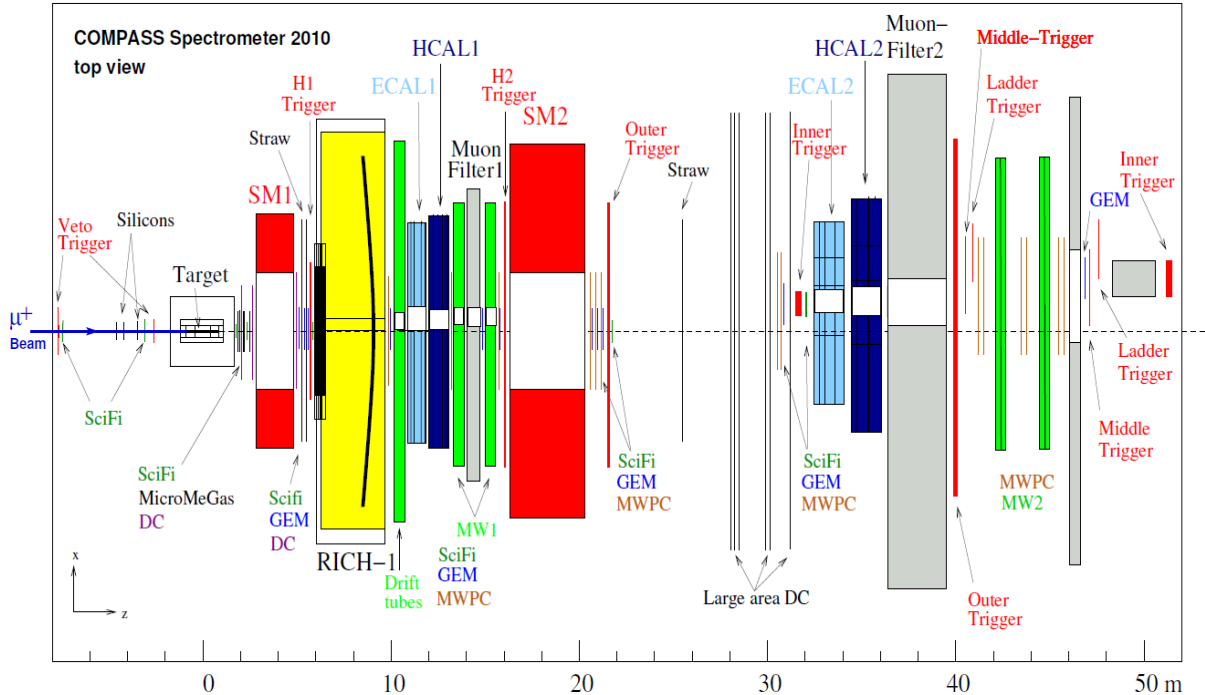

Figure 2.1: A scheme of the top view of the COMPASS spectrometer from the SIDIS measurement in 2010 [37].

The COMPASS spectrometer consists of three parts: the detectors upstream of the target responsible for monitoring of the beam, the Large Angle Spectrometer (LAS), and the Small Angle Spectrometer (SAS) both downstream of the target. A sketch of the top view on the whole spectrometer (in the SIDIS setup) is shown in the figure 2.1, the spatial view of the setup used for DY can be seen in the figure 2.2 (the difference between the two setups will be explained below). The contamination of the hadron beam is monitored by the **differential Cherenkov detectors** (CEDARs) which are located upstream of the target. The purity of the hadron beam is circa 97% of pions with the 2.3% rest of kaons and 0.7% of antiprotons and other particles [9]. Muon beam is obtained from the charged pion decay $\pi^- \to \mu^- \nu_\mu$, and because of the V-A character of the weak interaction they are naturally polarised. The polarisation of the muon beam has been measured up to -80 ± 4% [42]. The upstream detector behind the CEDARs is the **Beam Momentum Station** (BMS) measuring the momentum of the beam particles however it is only applicable for muon beam. It is followed by the **Beam telescope**

---

[11] The SPS beam is distributed between several experiments such as COMPASS, NA62, NA61, and the Test beam hall.

which determines the exact position of the particles in the beam. It consists from the **Scintillating fibers** (SciFi) and the **silicon detectors**, but the latter were also not present during the data taking with the hadron beam for DY run because they could not stand the high intensity of the beam. The SciFi detectors are used for the track reconstruction due to their excellent time resolution which is 0.4 ns rather than for their spatial resolution (better than 50 μm) [9]. Both previously mentioned detectors belong to the group of so-called very small area trackers.
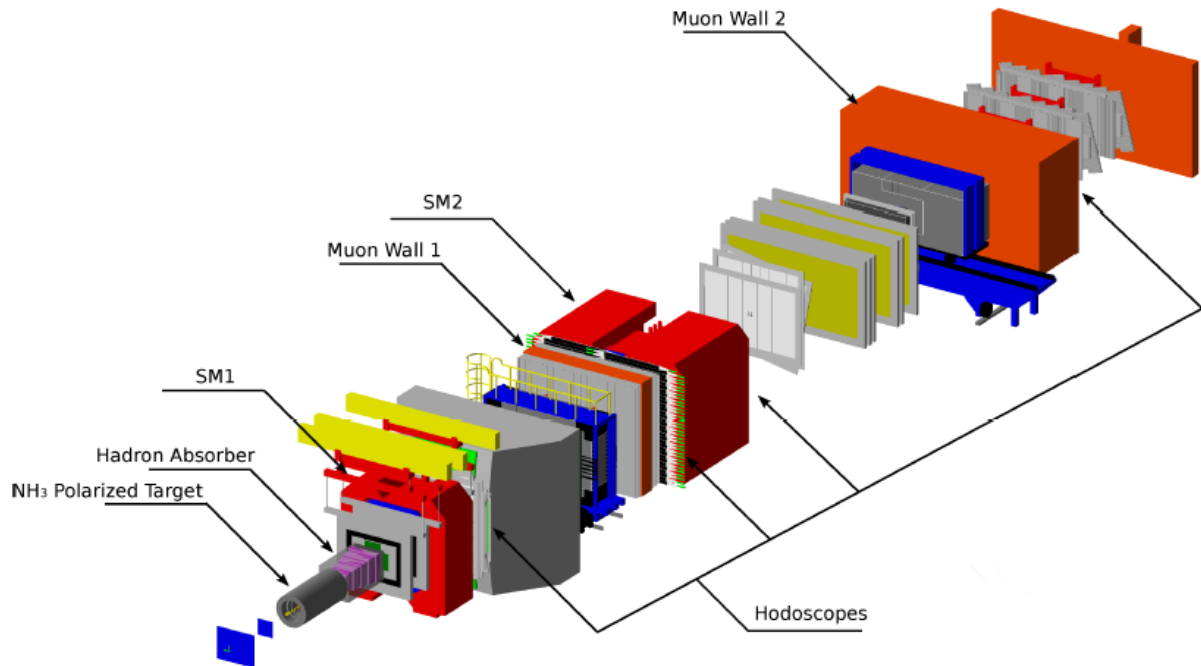

Figure 2.2: Three-dimensional view of the COMPASS setup used for the DY measurement [24].

The LAS contains the SM1 dipole magnet (see figures 2.1 or 2.2) for measuring the momentum of the particles with the aperture of 229×152 cm^2 which gives ± 180 mrad acceptance and magnetic field integral 1.0 Tm. The SM2 dipole magnet in SAS area has the magnetic integral field 4.4 Tm and aperture 1×2 m^2 [42]. Both of them are followed by several different types of detectors with decreasing resolution with the increasing distance downstream from the target. The small area trackers are used to track the particles which are in close distance from the beam throughout the spectrometer. The first of them located in LAS area are the **Micromesh gaseous detectors** (Micromegas) (see the figure 2.3) which are right behind the target accompanied with additional SciFis. There are 3 Micromegas station with 4 projection planes each (X, Y, and two diagonal U, V). They are gaseous detectors with a conversion region and the amplifier region separated with metallic micromesh, as can be seen on the scheme 2.3a. The principle is that the incoming particle ionizes a gas atom which is attracted to the mesh and produces an electron shower which is detected by the read-out

strips. Their spatial resolution is around 100 μm and the time resolution ~9 ns [24]. In the 2015 the Micromegas were upgraded for a pixelised center. However, the Micromegas are not the essential detector for DY measurement because of their low angular coverage.

<table>
<tr><td>(a) Principle of the Micromegas detector</td><td>(b) Picture of the two Micromegas planes (U and V projections). The active area is 40×40 cm².</td></tr>
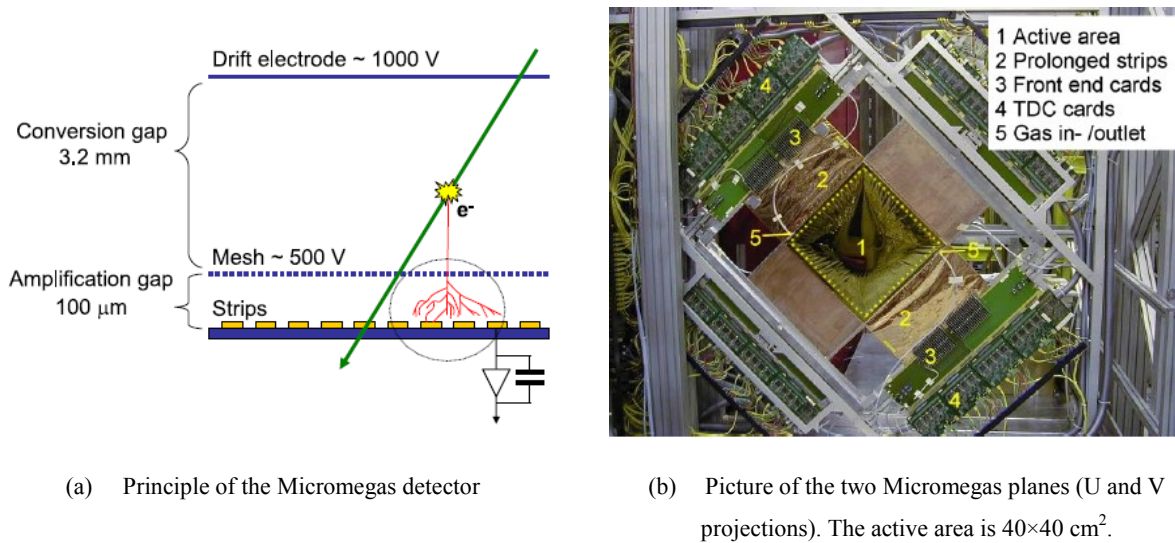</table>

Figure 2.3: The Micromegas detector (taken from ref. [42]).

The second type of small area tracker are the **Gaseous electron multiplier detectors** (GEM) shown on the figure 2.4. They are 11 GEM stations distributed throughout the whole spectrometer (see the fig. 2.1). They are gaseous detectors with 3 polyamid foils (50 μm) densely covered with the drifting holes with a strong electric potential up to 100 V which gradually amplifies the ionizing signal of the passing particle up to the read-out strips. The active area of GEMs is 31×31 cm^2 and their time resolution is 10 ns. Two of the stations were also pixelised, although they are not important detectors in the DY measurement from the same reason as the Micromegas.
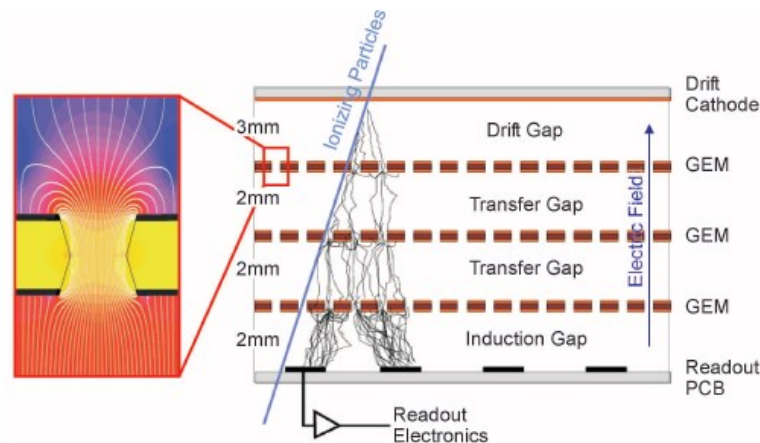

Figure 2.4.: The schematics of the GEM principle of operation. Taken from ref. [42].

The large area trackers are not exposed to such a high flux of particles as they are not that close to the beam, and thus they also have a larger angular coverage. This group of detectors

consists of **Drift Chambers** (DC), **Straw tube detectors** and **Multiwire Proportional Chambers** (MWPC), and in SAS of **W45** and **RichWall**. They are also gaseous detectors, but have a worse time and spatial resolution, however, their active area is much larger. Concerning the DCs, there are four stations in the spectrometer with four plane projections each, two of them upstream from the SM1 – in LAS – (DC00, DC01) and the other two downstream in SAS (DC04, DC05). The active area of the first two is 180×127 cm^2, and the latter two 500×250 cm^2 (their dead zone in the central part coincides with the active zone of the small area trackers which are usually attached to them, dead zone prevents saturation of the detectors from the non-interacting beam flux), and their spatial resolution is 190 μm for LAS DCs and 0.5 mm for SAS DCs [42]. The principle of their operation is shown in figure 2.5. The SAS large area drift chambers W45 have 6 stations with also 4 planes each for each projection. Their active area is 520×260 cm^2 with a large dead zone ranging from 50 to 100 cm^2 depending on the station. MPWC unlike the previous mentioned drift chambers consists only of a single chamber with a multiple layers of wires. MWPCs are positioned both in LAS and SAS in 14 stations. Their active zone is 178×120 (or 90 for some of them) cm^2 and spatial resolution ~1.6 mm which seems to be very bad, however it has been shown on the internal DY analysis meeting that they are actually essential for the reconstruction of the particle tracks in small angles [43]. The Straws are made of thin plastic tubes inflated with gas and a gold-plated tungsten wire stretched inside every tube which attracts the electrons from the gas ionisation. There were 2 straw detectors in the spectrometer in the time of DY measurements, presently only one is operating. The active area is 323×280 cm^2 and its spatial resolution is 190 μm thus they are efficient for tracking of charged particles in large scattering angles (15 – 200 mrad) [42].
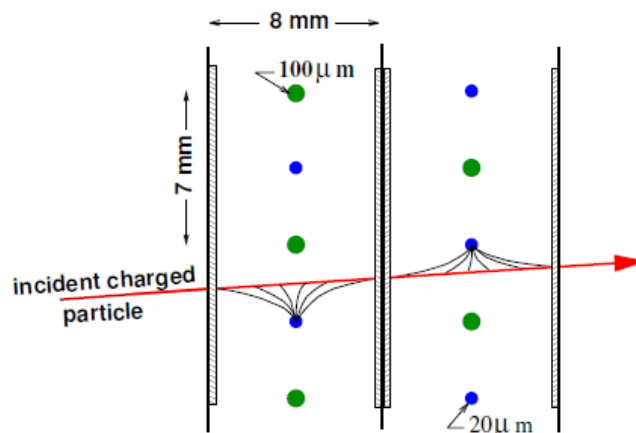

Figure 2.5: The drift cell geometry of COMPASS DC. Taken from ref. [42].

The last from the large area trackers is RichWall detector which is made of 8 layers of Mini Drift Tubes (MDT) modules which consist from an aluminium comb with 8 spaces

covered with an inox layer, in each space a gold-plated tungsten wire is stretched acting as an anode. The detector is located right behind the RICH detector which will be discussed below.

The detection of the muons is performed by the **muon walls** (MW1 in LAS and MW2 in SAS). They are place at the end of the spectrometer as muons interact very rarely. They consist of an absorber, which filters the muons from the other particles (the MW1 has a 60 cm thick iron wall and the MW2 has 2.4 m thick concrete wall), and several tracking planes composed of the MDT [42] (see the fig. 2.6). Their active zone is over 16 m^2 and their resolution is 3 mm for MW1 and 0.6 – 0.9 mm for MW2. The principle of work is following: the planes are placed in front of the absorber and behind it as well, and when a track detected in the former detector continues to the latter, then the particle must be a muon.
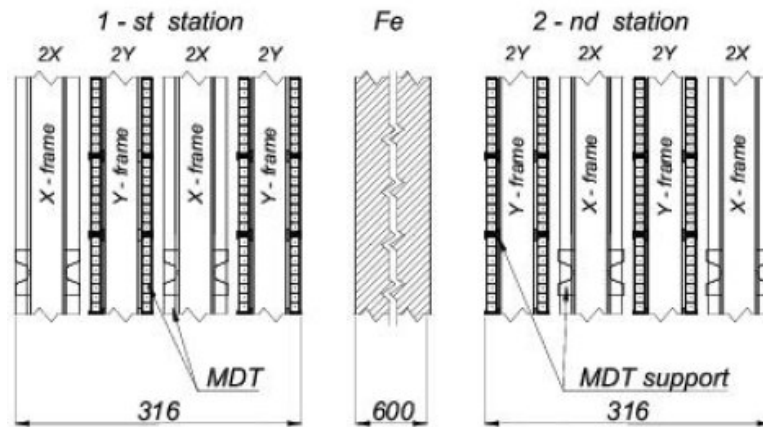

Figure 2.6: The schematics of the side-view of the MW1. All dimensions are in mm. Taken from ref. [42].

Another important group of the detectors are the **calorimeters**. There are currently two electromagnetic (ECAL1 and ECAL2) and two hadronic (HCAL1 and HCAL2) calorimeters in COMPASS, numbers denote their location in LAS and SAS, respectively. The ECALs are mostly homogeneous calorimeters, i.e. that the calorimeter modules are made of a lead glass that serves as both the absorber and the scintillator. The modules are read out by photomultipliers. There are about 3000 modules in the central part of the ECAL1. On the other hand, the ECAL2 is a shashlik type calorimeter which denotes altering layers of the absorber and the scintillator. The HCALs are both shashlik type. There are 480 modules in HCAL1 and 218 modules in HCAL2. All the signals are read by the multipliers and small part of them is used for triggering. The calorimeters are not used during DY measurement, hence we will omit the details (for more, see [42]).

Important part of the apparatus for the particle identification is the **Ring Imaging Cherenkov detector** (RICH). It is used for the identification of the charged particles of the

momentum range $1 - 43$ GeV/c. It is based on the Cherenkov effect, i.e. the emission of an electromagnetic radiation when the charged particle is passing through a dielectric medium with velocity higher than the phase velocity of light in that medium [5]. It contains about 80 m^3 of gas (C_4F_{10} is usually used). It has to be perfectly transparent thus the gas is usually additionally purified. The reflective part consists of two mosaic mirrors made of 116 hexagonal and pentagonal mirrors. The scheme and the sketch of the RICH detector are shown in the figure 2.7. The photo-detection is based on photomultipliers and MWPC detectors equipped by CsI photocathodes which detect the Cherenkov light and convert it to photoelectrons and those are amplified by the MWPC. Although is commonly used only for the hadron spectroscopy, for DY it can be used but with the data from the other detectors is rather redundant.
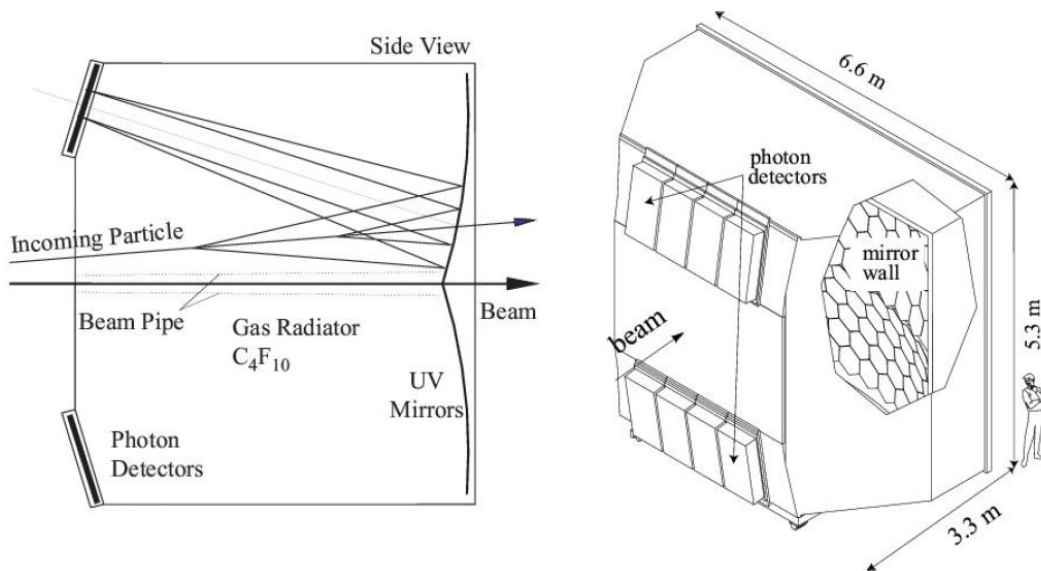

Figure 2.7: The scheme of the RICH detector (on the left), and the artistic view (right). Taken from ref. [42].

2.2 The Data Acquisition system and triggers

The trigger system enables to pre-filter the data from the detector system to record only the processes of our interest. It consists of the hodoscopes made of scintillating slabs which are capable of working in a high rate environment as they have a very fast response (about 1 ns). The trigger system has 5 stations with 2 hodoscopes at every station and the triggering is based on the coincidence signal between them. The principle of signalling for the DY events is having two muons in coincidence [24]. Three hodoscope stations were used for that purpose: Large Angle Spectrometer Trigger (LAST), the Middle Trigger (MT), and the Outer Trigger (OT). For selecting a dimuon event a double trigger is mandatory, i.e. either both muons has to be signalled from the first stage of the spectrometer (LAST-LAST, azimuthal

angles of muons between 25 to 160 mrad), or a single muon signal coming from LAST had to be coincided with a signal from Middle or Outer (8 to 45 mrad). As will be elaborated in the Chapter 3, the MT was not used in our analysis at the end.

Once the data are collected they need to be read out, appropriately filtered and preliminary analysed to create a meaningful set of information from various detectors. This is the purpose of the Data Acquisition system (DAQ; see the figure 2.8 for its scheme). COMPASS detector system has about 300 000 channels that have to be read out and processed in a sufficiently high rate. The readout of the detectors is performed by the front end electronics. The average size of a single event is 35 kB and trigger rate is 50 kHz. For the DY data taking the rate is rather lower, about 30-35 kHz, and the event size 25 kB. The front end electronics converts the analogue signals from the detectors to a digital form and sends them through 1000 links into the hardware modules called CATCH, HGeSiCa, and Gandalf (250 modules in total). These modules are located near to the detectors and have two purposes: to operate the front end electronics, and to create basic data blocks universal for the rest of the DAQ system. The output of the modules goes straight to the Field Programmable Gate Array (FPGA) modules, or in some cases through Slink multiplexers or TIGER modules.
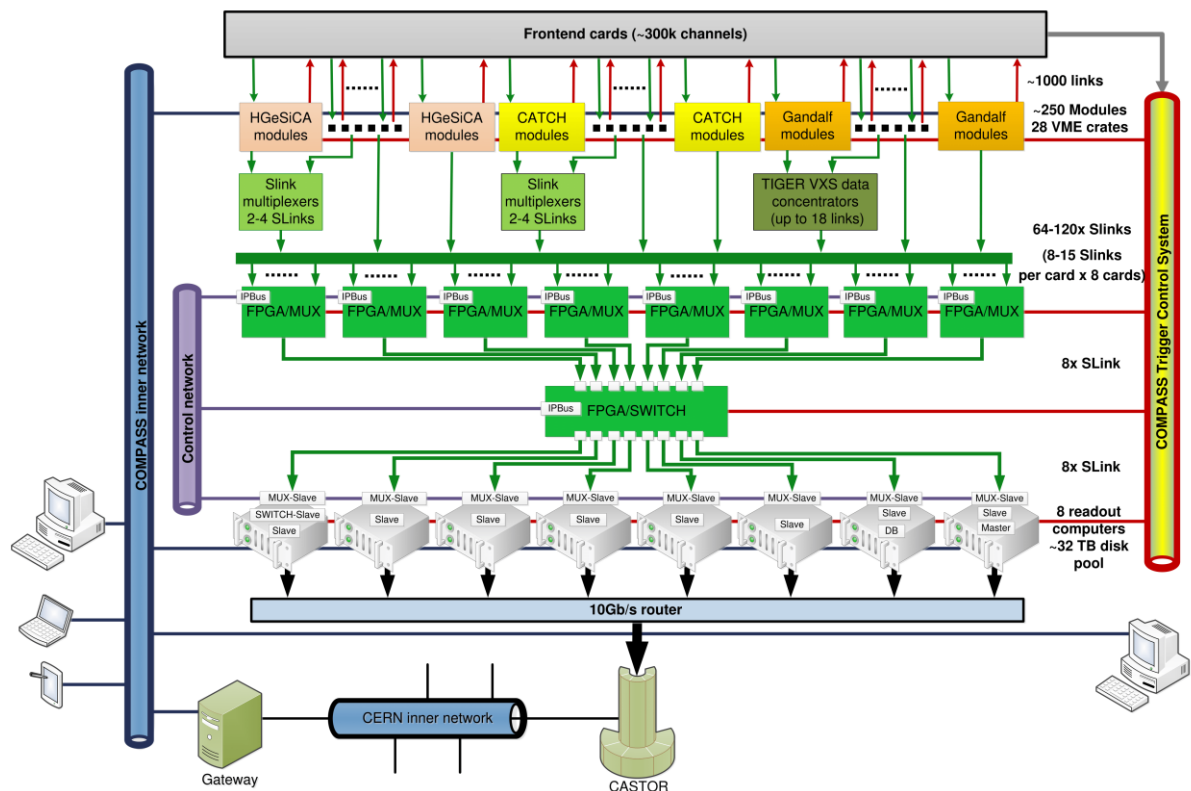

Figure 2.8: The scheme of the new DAQ hardware [44].

40

In the Slinks and TIGERs the number of links is reduced to about 90, depending on the number of detectors. The FPGA takes at most 15 links and reduces them into 1 output link. These modules are connected to the triggers and timing systems, as can be seen in the fig. 2.8, which label the outputs with timestamps and event identification. The output data from FPGA are called subevents, i.e. parts of a particular event [44].

Then the data flows from the FPGA level to the SWITCH which composes events from the corresponding subevents and sends them forward to readout PCCORE computers via custom-made spill-buffer cards which process them further and convert them to *date* format. Then the data are temporarily stored in the PCCOREs (~32 TB at our disposal) and about 1% of events is directly used for the online monitoring. Final step is sending the data to the CERN Advanced STORage manager (CASTOR), the central permanent data storage of CERN. Then the data can be accessed by the physicists for the final reconstruction (see below) and subsequent analysis. For more technical information about the DAQ architecture, see [44],[45].

2.3 The Data reconstruction and analysis

The stored raw data have to be reconstructed in order to be available for the physical analysis. For that purpose the COMPASS experiment uses the COMpass Reconstruction and AnaLysis program (CORAL). The reconstruction is a complex algorithm of identifying the particles and completing their tracks and vertices. The position of a hit in a particular detector is not a part of the raw data, it is a first step of the reconstruction which has to take the info of the fired channels from the detector and compare it with the detector geometry [24]. Then, the track reconstruction takes place using the information of position, time, energy, momentum, or velocity. The track is reconstructed in the segments of the spectrometer which surround the magnets SM1 and SM2, then the segments are connected and fitted taking into account the magnetic fields of both of the magnets. The last step of the reconstruction is the vertexing using the info from the reconstructed tracks. The output of the production from CORAL is so-called mini Data Summary Trees (mDSTs) with the fully reconstructed events. The mDSTs can be analysed with the COMPASS program PHysics Analysis Software and Tools (PHAST).

2.4 The Setup for the Drell-Yan measurement

The specific modifications of the COMPASS spectrometer had to be done for the efficient DY data taking. In order to measure the angular modulations from the DY cross-section a

large angular acceptance is necessary, and of course a high-performance polarised target, together with the support for the high-intensity hadron beam. For the DY measurement a 190 GeV/c^2 π^- beam was used with the intensity up to ~10^8/spill, and the transversely polarised target (see the subsection below). The DY setup can be seen in the figure 2.9.
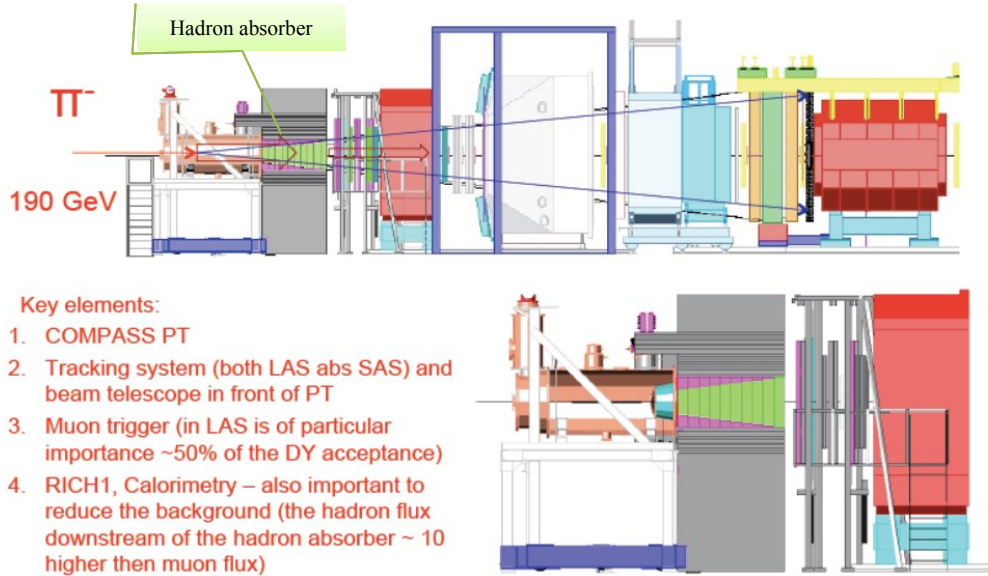

Figure 2.9: The scheme of the COMPASS spectrometer for the DY measurement (taken from ref. [46]).

The most important modification of the DY setup based on the 2007 and 2008 test runs [37] is the installation of the new **hadron absorber** [46]. The absorber is needed to reduce the high secondary hadron and electron flux produced by the DY reaction (for the specific reaction measured at COMPASS, see eq. (1.78)) to lower the occupancies of trackers. Muons have a long mean free path and thus most of them easily penetrate throughout the whole spectrometer with just minor deviation of their track due to their elastic scattering. The choice of the absorber material was guided by two main criteria: to maximize the number of interaction lengths crossed by the particles from the hadron shower in order to stop them and to minimize the radiation lengths to have a minimal energy loss, i.e. to minimize the multiple scattering of muons. A model of the absorber was tested in 2009 DY test beam and the results were satisfactory [37]. The position of the hadron absorber is marked in the figure 2.9. The absorber consists of three main parts: the outside layer is a stainless steel block; the main part is made of aluminum oxide (Al_2O_3); and the very inner part is the tungsten beam plug which is supposed to stop the beam[12]. The whole absorber is shielded with concrete to protect the target electronics and reduce the radiation dose spread in the hall. The inevitable disadvantage

---

[12] In the previous experiments the configuration with no beam plug but just a hole of air was tested in order to prevent backscattering of the beam particles into the target, but it wasn't successful.

of using the absorber is the increased multiple scattering of the measured dimuons which worsens the precision of the vertex reconstruction. As a consequence, an increased migration of events from one target cell to another appears, which lowers the measured spin asymmetries. The rate of migration of events through the cells has to be considered in the analysis as will be seen in the Chapter 3. There were two precautions adopted to reduce the event migration between the cells: to enlarge the gap between the target cells to 20 cm; and the installation of the so-called **vertex detector** between the target and the absorber (a modified SciFi detector, in principle). This detector should have helped to improve the resolution of the vertex reconstruction by a factor of 5 [37]. The vertex detector was installed before the beginning of the 2015 run, unfortunately the efforts for reconstructing the data from the detector have not yet been successful due to the high number of correlated hits. The discussions on solving the reconstruction problem are still on-going [47].

The higher beam intensity in the 2014 and 2015 DY runs together with the presence of the hadron absorber also led to general reinforcement of the concrete shielding around the whole spectrometer and to repositioning of the access door to the experimental zone to reduce the radiation dose. For the same reason, the control room has been moved to a remote control room which is located in an office building (no. 892).

2.3.1 The Polarised target

The polarised target (PT) is the crucial component of the COMPASS experiment for the measurement of the transverse or longitudinal spin asymmetries. The construction of the COMPASS PT enables to gain a very high polarisation (in the material used in DY measurements, the ammonia, the polarisation of 95% is technically reachable). The main components of the target are a dipole magnet and a solenoid (their operation principle will be explained below), a cooling device, and a microwave system. The figure 2.10 shows the scheme of the PT layout (the detailed scheme of the PT can be found in the Attachment 1).

The polarizability of the target material is enabled by its nuclear paramagnetism. However, the nuclear paramagnetism is very weak and not sufficient for reaching a significant level of polarisation even in presence of very low temperatures and high magnetic field. To help the process of polarisation, the Dynamic Nuclear Polarization (DNP) has to be used, i.e. a technique of transferring a high electron polarisation to the nuclei through a radiofrequency field [9]. DNP requires temperatures in order of ~100 mK and a strong and homogeneous magnetic field (more on the principles of the DNP method can be found e.g. in [9],[48]). This method enables to reach the level of polarisation exceeding 90%.
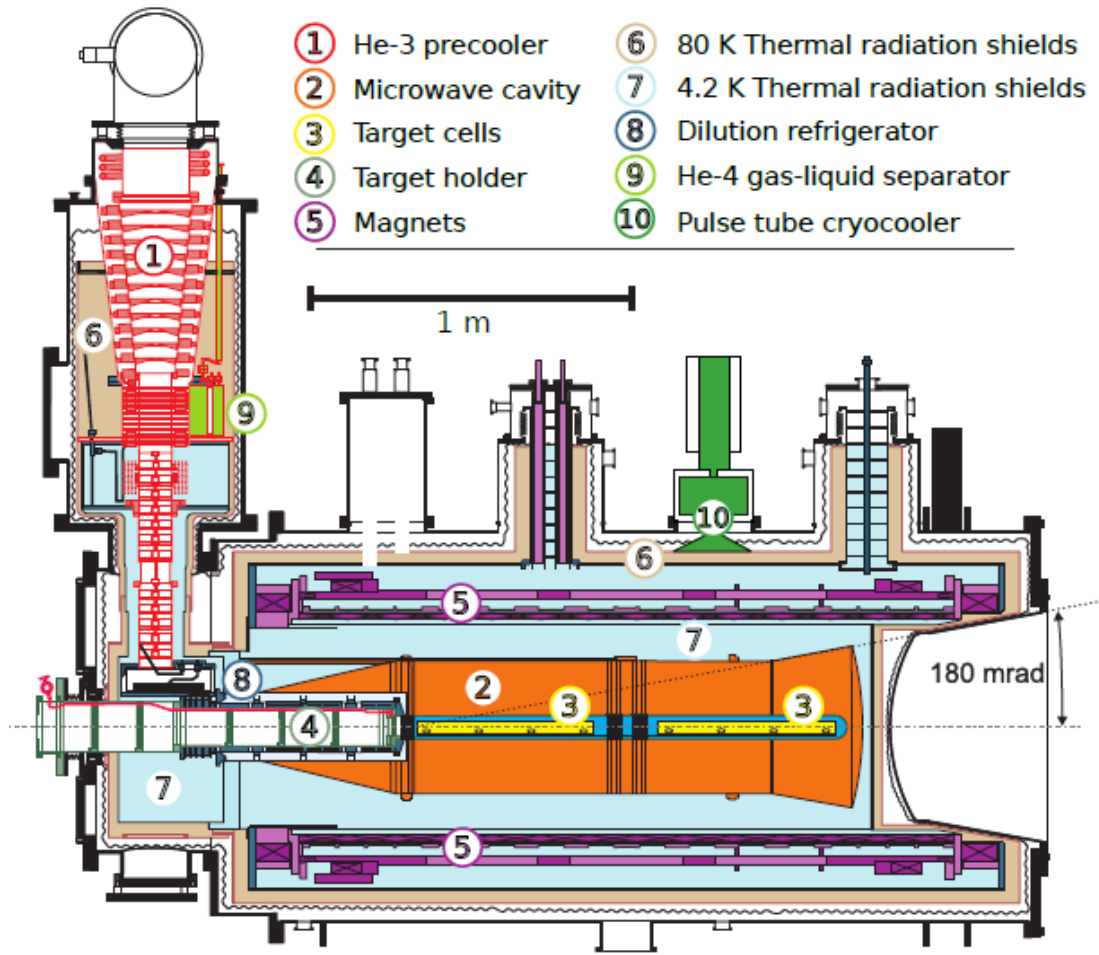
Figure 2.10: The side view of the Polarised target system. Taken from ref. [49].

The PT consists of 2 cells, the upstream and the downstream cell, which have an opposite polarization. Each of them has 4 cm in diameter (see figure 2.11) and 55 cm in length[13]. The reason for having two separate cells is that the asymmetries cannot be extracted from the consecutive measurements on the same target with switched polarisations because of the variations of relative beam flux which would highly increase the systematic error. Each cell contains 5 NMR (Nuclear Magnetic Resonance) coils which provide a precise measurement of the nuclear polarisation [9]. The target cells are placed in the dilution chamber which is inside the microwave cavity. The cavity is cloaked by the solenoid and dipole which were mentioned above.

The dilution chamber containing the target cells is a part of the dilution refrigerator (DR) which allows cooling down the target material to a temperature of about 70 mK [9]. It is worth to note that the COMPASS DR is one of the largest in the world, and so is the PT. The principal of operation of the DR is the following: There is a mixture of liquid ^{3}He and ^{4}He

---

[13] These target parameters apply only for the DY measurement, for the different settings used in other measurements, see e.g. [9][42].

with a specific concentration of ^{3}He. The mixture is cooled down to ~1 K. Then a phase separation occurs, i.e. the mixture splits up to a phase rich on the ^{3}He (concentrated phase) and on the phase rich on the ^{4}He (diluted phase), where the first starts to float on the latter. There is a capillary inside the DR that ends in the diluted phase. The capillary continuously sucks out the helium from the diluted phase and as the there is a pressure difference between the ^{3}He and ^{4}He, the ^{3}He is sucked preferably. Thus the diluted phase soon gets ^{3}He-depleted (the fraction of ^{3}He in dilute phase cannot decrease lower than to 6% which results from the ^{3}He and ^{4}He phase diagram, see the figure 3.12). Consequently the atoms of ^{3}He are forced to cross the boundary between the two phases from the upper concentrated phase. This is where the actual cooling takes place. It is analogous to the classical evaporation but the role of the vacuum is played by the ^{4}He atoms. The ^{3}He vapours are then compressed, purified, cooled down in heat exchangers and returned back to the concentrated phase, allowing a continual operation. ^{3}He vapours are also sucked out from the upper phase surface to preserve the cooled temperature. The space where both of the separated phases are kept is the dilution (or mixing) chamber (in the COMPASS PT it directly surrounds the target cells; see the figure 2.11). The DR is equipped by 36 thermometers for the temperature monitoring and several pressure gauges, valve controls, and flow meters for checking the ^{3}He and ^{4}He flows. The monitoring system is run by computer software.
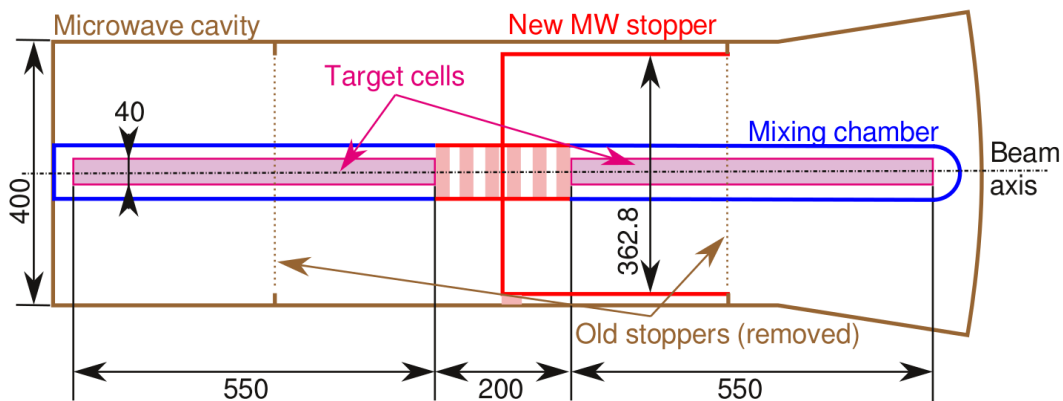
Figure 2.11: The Polarised target and the microwave cavity in more detail. The dimensions are in mm [50].

When the material is cooled, the procedure of polarisation takes place. The magnetic field for the polarisation is provided by a 2.5 T superconducting solenoid magnet which align the spins of nucleons in the material parallel with the magnetic field, i.e. longitudinal with the beam direction. After the polarisation the additional 0.6 T superconducting dipole magnet

rotates the spins into the transverse direction[14]. At temperature of 70 mK the relaxation times of nucleon spins are very long[15], which enables a long measurement with the transverse polarisation without the necessity to repolarise (about a week). A photograph of the whole device is shown in Attachment 2.
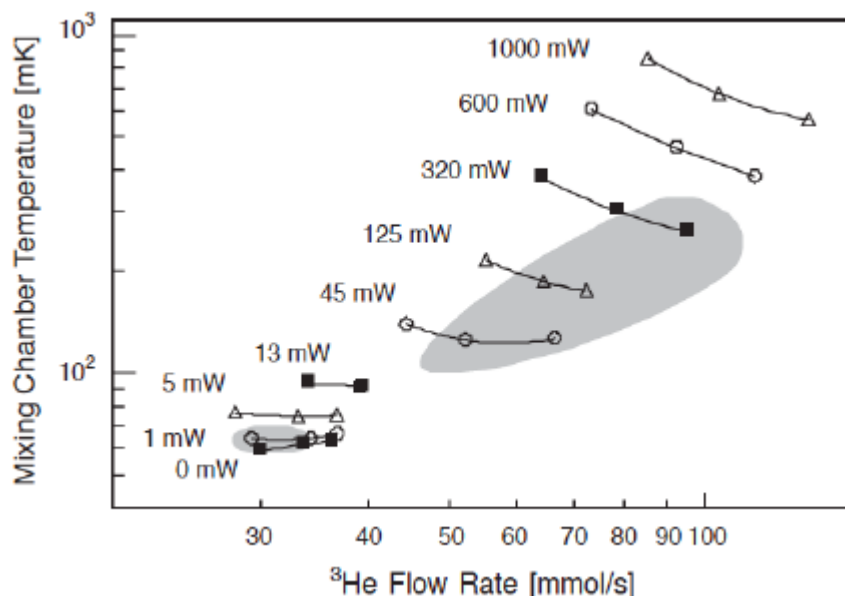

Figure 2.12: The dependence of the dilution chamber temperature (in mK) on the ^{3}He flow (mmols/s). The large shaded area indicates the region where the DNP occurs, and the smaller one shows the region of a frozen spin mode. Taken from ref. [9].

The radiofrequency field for the DNP uses microwaves at frequency of about 70 kHz. The key component of this system is the microwave cavity which creates the standing microwaves of the given frequency inside its volume which is divided to two parts by a microwave stopper, as can be seen in the figure 2.11. This setup allows using different frequencies in upstream and downstream cell which is necessary to obtain the opposite cell polarisations. The cavity is cooled by liquid ^{4}He to a temperature of about 4 K. The rest of the system consists of the two microwave generators.

The choice of the target material is crucial point for optimising the function of the PT. It is necessary for obtaining the highest possible polarisation and for the largest possible statistics. The properties of the material can be expressed by the formula called the figure of merit F_{oM}:

---

[14] This process of the field rotation occurs as the solenoid is ramped down after the creation of the polarisation, and simultaneously the dipole is ramped up.

[15] They reach about 4000 hours for the ammonia (used in DY measurements) in the transverse field [3].

$$F_{oM} = f^2 P^2 \rho F_p, \qquad (2.1)$$

where F_p is a packing factor; P is a maximum possible polarisation of the material; ρ is the target material density; and f is the dilution factor which denotes the fraction of events on polarised nucleons with respect to the unpolarised ones, in other words a fraction of polarisable nucleons in the target material, which is given as follows:

$$f = \left(1 + \frac{n_A \sigma_A}{n_p \sigma_p}\right)^{-1}, \qquad (2.2)$$

where σ_A is a cross-section for an unpolarised nucleon, σ_p is a cross-section for the polarised one, and n_A and n_p are molar densities for the particular nucleons.

In the past COMPASS and SMC experiments were of need for the neutron target, thus the deuterated materials as ^{6}LiD or deuterated butanol were used. For the DY measurement the solid ammonia is used. This target material was produced by freezing the liquid ammonia by liquid nitrogen into a form of small beads with 4 mm in diameter. Then the material was irradiated by 20 MeV electron beam at low temperature at the Bonn University linac to create the NH$_2$ radicals needed for the DNP. The maximum theoretical polarisation is over 95% as we mention above, while the usual polarisation achieved at COMPASS was between 80 and 90 % [9] (for the actual polarisation conditions during the DY data taking, see Chapter 3). The dilution factor of the ammonia is 0.15 in average. Additional technical details on the PT or DR can be seen e.g. in [9],[48],[51].

3. Drell-Yan measurements at COMPASS

One of the major goals of the COMPASS DY program is to test the crucial QCD prediction of *T*-odd TMDs that the Sivers function and the Boer-Mulders function have an opposite sign when measured in DY and SIDIS (see eq. (1.88)). The COMPASS experiment has measured these two functions in the SIDIS process in 2007 and 2010 and confirmed the non-zero value of the Sivers function predicted by Collins [28] (see Section 1.3.3). In the 2015 the COMPASS performed the very first polarised DY measurement and the first results were submitted to be published [52]. Along with the official analysis we made our own analysis of the transverse spin asymmetries (TSA) with a different method applied. In the following section the overview of the data-taking and data production for the 2015 DY run will be given. The strategy and methodology of our analysis will be shown. Then the selection of the events in order to get the process of interest, supress the background, and ensure a good data quality will be described. The systematic tests will be discussed. Finally the extraction of the three discussed TSAs (Sivers, Pretzelosity, and Transversity) will be presented together with a conclusion of our analysis and a comparison with the official results [52],[53].

3.1 The 2015 DY data taking

The polarised DY data taking of 2015 was preceded by a pilot run with the unpolarised target in 2014[16]. This two months lasting pilot run was important for commissioning of the spectrometer and the new data acquisition system. The data taking conditions of the 2015 data taking were the same except of the three changes: the transverse polarisation of the target cells; addition of a thin lithium foil downstream of the absorber to stop the slow neutrons produced in the interactions along the absorber, which caused a high flux of low-energy charged particles in the first detectors behind the absorber [24]; and the installation of a new drift chamber, DC05 (for the photographs of the installation of the DC05 detector, see Attachment 4). The purpose of the additional detector was to replace one of the Straw detectors, Straw2, which became outdated and inefficient. The 2015 data taking ran since 27th of April to 15th of November. The 190 GeV/c^2 π^- beam with average intensity of 6×10^7/s was used. The transversely polarised target consisted of two oppositely polarised cells as described

---

[16] There was an earlier test run in 2009 which lasted only 3 days and its only goal was to test the feasibility of the COMPASS spectrometer to measure the DY as it was originally designed for very different physics processes. However, this test proved to be a success.

in the Section 2.3.1, which were separated by 20 cm gap to decrease the migration of event from one cell to another to as much as was possible. The opposite polarisations of the cells in order to record both spin orientations simultaneously [53]. The whole run was divided in 9 periods with two weeks each. In the middle of every period the polarisation orientation of the target was reversed to significantly lower the systematic effect of a different acceptance in each target cell.

3.2 Monte Carlo simulations for the DY measurement

The support of Monte Carlo (MC) simulators in the interpretation of the high energy physics processes is nowadays a necessity. A sufficiently precise simulation of the experimental setup is essential for obtaining of the spectrometer acceptances and resolutions as a function of any particular kinematic or angular observable. For the purpose of the COMPASS DY analysis a full-chain MC simulation has been used. The pure DY process $(\gamma^* \rightarrow \mu^- \mu^+)$ without initial or the final state (hadronic shower) for high DY mass was simulated by the PYTHIA 6 (for detail, see [53]). The k_T of the target nucleon and beam pion were set on the range from 0.9 to 3.0 GeV/c^2. For the dimuon propagation through the spectrometer material the TGeant setup simulation was used, which is a version of GEANT 4 adapted for COMPASS. For the best possible imitating of the real data condition, the updated information of the detectors position from every period were used, similarly as the actual extracted beam parameters were put as an input for the beam simulation. The momentum spread of the pions in the beam was simulated using the parameters extracted from the 2014 DY pilot measurement using the BMS station. For the beam particle propagation through the target material before meeting the interaction point a new vertex generating algorithm was applied using the multiple Compton scattering and energy loss [53].

The material and type of elements of the spectrometer are described by the TGeant material map. The relevant information like density or radiation length about every cell is stored. The materials of all spectrometer components are taken into account for computing the spectrometer acceptance including the detector frames, support structures, and the hadron absorber. The simulated data sample is handled in the same way as the real raw data (see Section 2.3), it is processed by the CORAL software for the track reconstruction. The produced mDSTs are then analysed by the PHAST and the simulated data can be directly compared with the real ones. The preliminary MC data has been produced in 2016 by the COMPASS MC experts, and currently the simulations of the trigger and detector inefficiencies are on-going [54].

The TSAs in the presented analysis were extracted as a function of the nucleon and pion Bjorken variable x_N and x_π, then the so-called Feynman variable x_F defined as $x_F = x_\pi - x_N$, the transverse momentum of the dimuon q_T, and their invariant mass $M_{\mu\mu}$, in three kinematic bins for all the variables. The distributions of the variables were extracted from the MC together with the azimuthal angles distributions from the DY cross-section, eq. (1.73) in order to gain the acceptance and resolution of the spectrometer with respect to these variables. The figure 3.1 demonstrates the agreement of the real data with the simulated ones for the kinematic distributions x_N, x_π, q_T, and $M_{\mu\mu}$. As can be seen, the distributions mostly agree except of some deviations in the phase space edges.
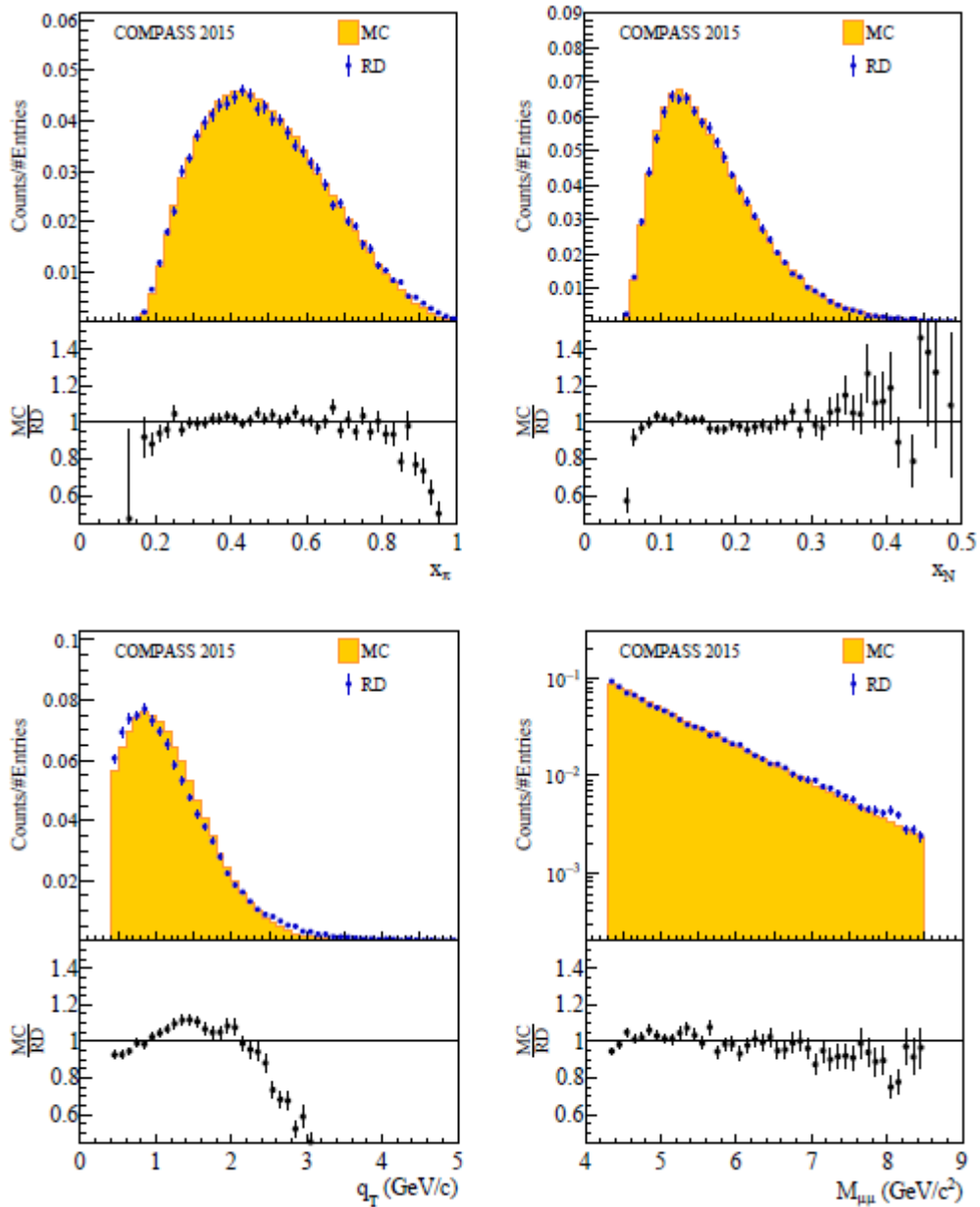

Figure 3.1: The distributions of the four kinematic variables x_N, x_π (upper band), q_T, and $M_{\mu\mu}$ (lower band) as a comparison of the real data (blue points) with the MC (yellow area). Taken from the ref. [53].
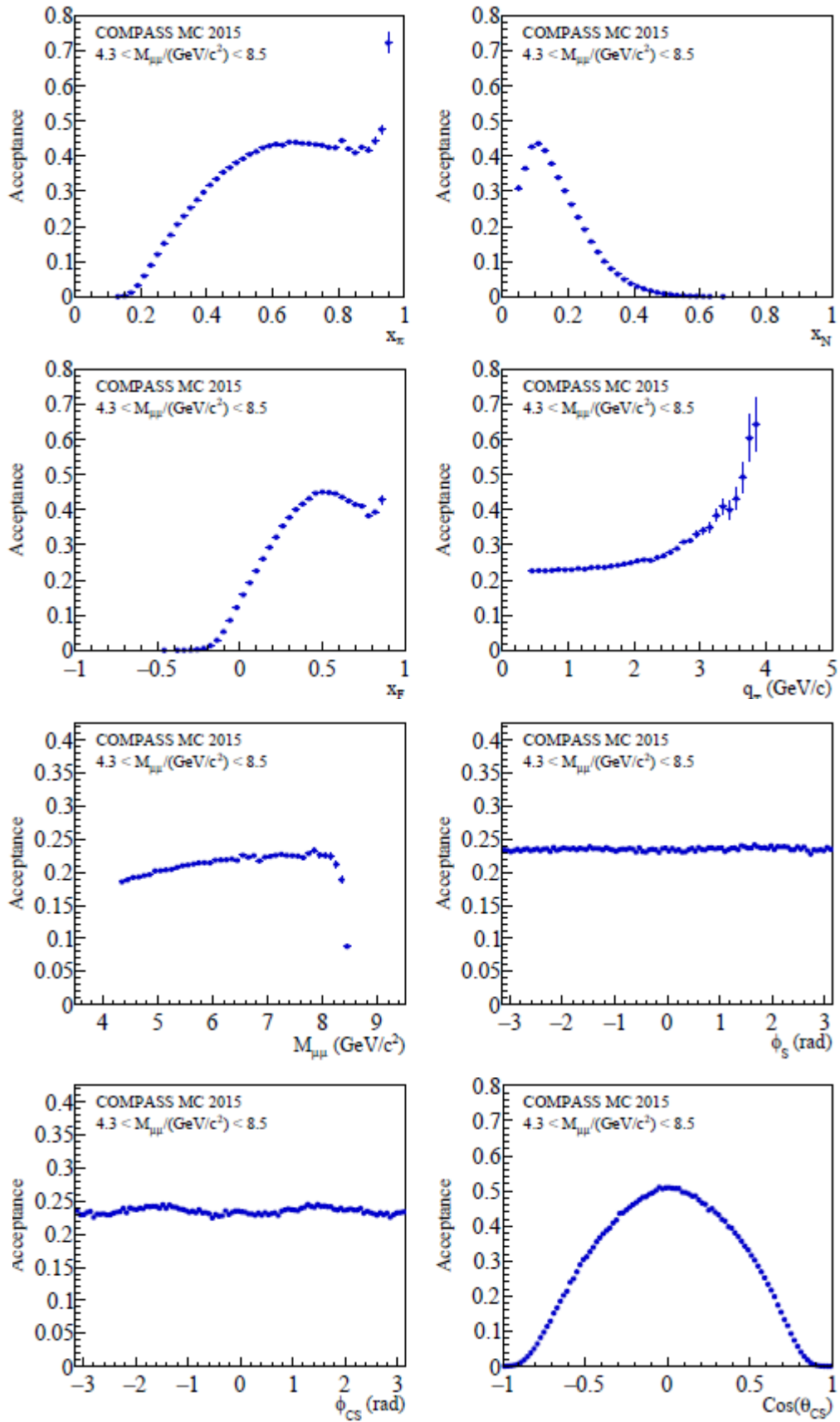
Figure 3.2: The acceptances in the kinematical variables x_N, x_π, q_T, and $M_{\mu\mu}$ (two upper bands) and angular variables ϕ_s, ϕ and $\cos(\theta)$. Taken from ref. [53].

On the basis of the produced MC data the acceptances for all the variables were produced, see the figure 3.2. The table 3.1 shows the extracted resolutions for the presented variables estimated by the RMS of the residuals, i.e. the difference between the generated value and the reconstructed one from the real data, evaluated event-by-event [53]:

Variable	RMS
X_v (cm)	0.04
Y_v (cm)	0.04
Z_v (cm)	10.97
$M_{\mu\mu}$ (GeV/c^2)	0.19
q_T (GeV/c^2)	0.15
x_N	0.02
x_π	0.01
x_F	0.02
ϕ (rad)	0.20
ϕ_S (rad)	0.19
θ (rad)	0.03

Table 3.1: The resolution for the used kinematic and angular variables (reproduced from the ref. [53]).

3.3 The Strategy for transverse spin asymmetries extraction

It can be seen from the figure 3.3 that there are various additional physics contributions in the mass spectrum, especially the J/ψ(1S) and ψ(2S) (or ψ') resonances at mass cca 3.1 and 3.7 GeV/c^2, respectively, and other main contaminations of the DY spectrum are: combinatorial background (CB) originating from uncorrelated pion and kaon decays into muons; and the so called open-charm background, that is a production od D mesons, which in part decay into muons. Thus, it is convenient for the studies of a DY process to distinguish four ranges in the dimuon invariant mass spectrum [53]:

I) $M_{\mu\mu}$: 1 – 2 GeV/c^2: "low mass" range, with a high contribution of combinatorial and open-charm background processes,

II) $M_{\mu\mu}$: 2 – 2.5 GeV/c^2: "intermediate mass" range,

III) $M_{\mu\mu}$: 2.5 – 4.3 GeV/c^2: "charmonium (J/ψ(1S) and ψ(2S)) mass" range,

IV) $M_{\mu\mu}$: 4.3 – 8.5 GeV/c^2: "high mass" range.

As can be seen from the fig. 3.3 (left), the last range of high mass is almost clear DY, with only 4% of contamination, and that is why it was chosen for this presented analysis. The table 3.2 shows the level of contamination of DY by the background processes with shifting of the lower limit of the high mass range with respect to the size of the data sample. As one can see from the table 3.2, the chosen lower limit for the high mass was an optimal compromise between the purity of the sample which would affect the systematic error, and its

size that determines the statistical error. The figure 3.4 demonstrates the estimate of the DY spectrum contamination using the assumption that the range $4.3 - 8.5$ GeV/c^2 is a pure DY, further it can be seen that an excess of events is visible for masses around 10 GeV/c^2, which can be attributed to the Υ resonance. The higher limit of the high mass range was chosen in order to avoid this region.
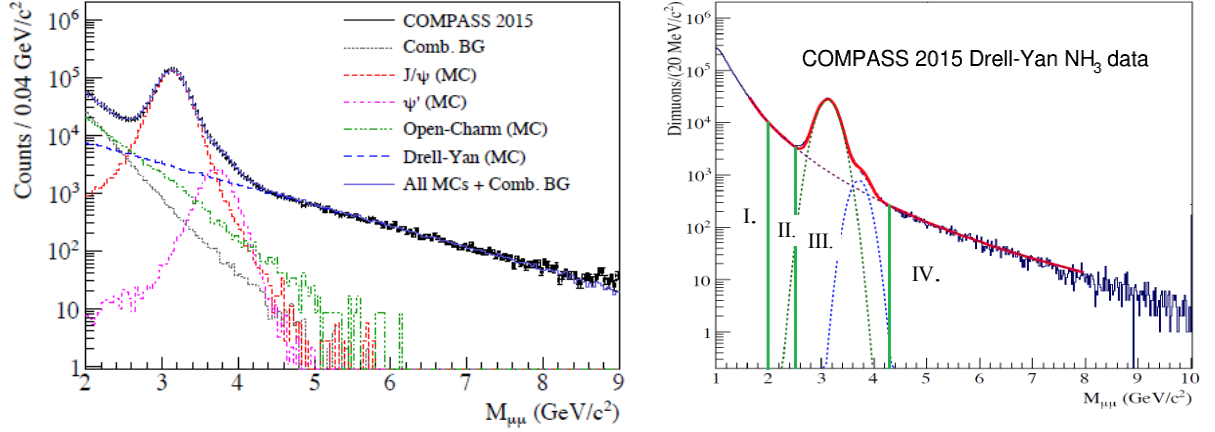

Figure 3.3: Dimuon invariant mass distribution with other physics contributions (left) and division of the four mass ranges in the spectrum (right). On the left, the real data 2015 are shown in black points, combinatorial background (CB) is estimated using the like-sign method, and other physics contributions to the cross section are MC generated and normalized to the data. Left figure taken from ref. [53], the right figure taken from ref. [55].
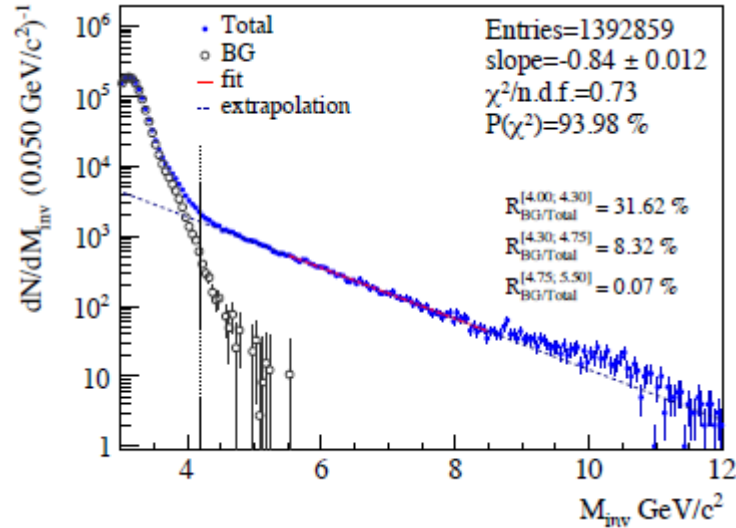

Figure 3.4: The estimated contamination of the DY process by background processes. The DY distribution is fitted by a decreasing exponential and extrapolated to the lower masses (taken from ref. [53]).

The two-dimensional distribution of (x_N, Q^2) and (x_π, Q^2) phase space of dimuons for all the four mass ranges are depicted in the figure 3.5. The whole mass spectrum of both of the distributions is inserted in the upper corner of the figure.

Mass [GeV/c^2]	Data	DY	J/ψ	ψ'	OC	CB	Bg. fraction
4.0 − 8.5	44245	40412	1054	1863	1679	319	10.8 %
4.1 − 8.5	39089	37186	608	722	1347	233	7.3 %
4.2 − 8.5	34986	34213	415	310	1106	176	5.5 %
4.3 − 8.5	31721	31448	242	139	814	126	4.0 %
4.4 − 8.5	28916	28907	164	65	656	91	3.3 %
4.5 − 8.5	26453	26583	120	33	557	75	2.9 %
4.6 − 8.5	24287	24434	94	17	440	60	2.4 %
4.7 − 8.5	22265	22451	64	9	332	45	2.0 %
4.8 − 8.5	20383	20593	53	8	274	28	1.7 %
4.9 − 8.5	18779	18871	41	3	199	17	1.4 %
5.0 − 8.5	17202	17320	39	3	149	15	1.2 %

Table 3.2: The statistical contribution of additional physics processes to DY estimated from MC, on the very right column one can see the fraction of the background that those processes cover (reproduced from the ref. [53]).
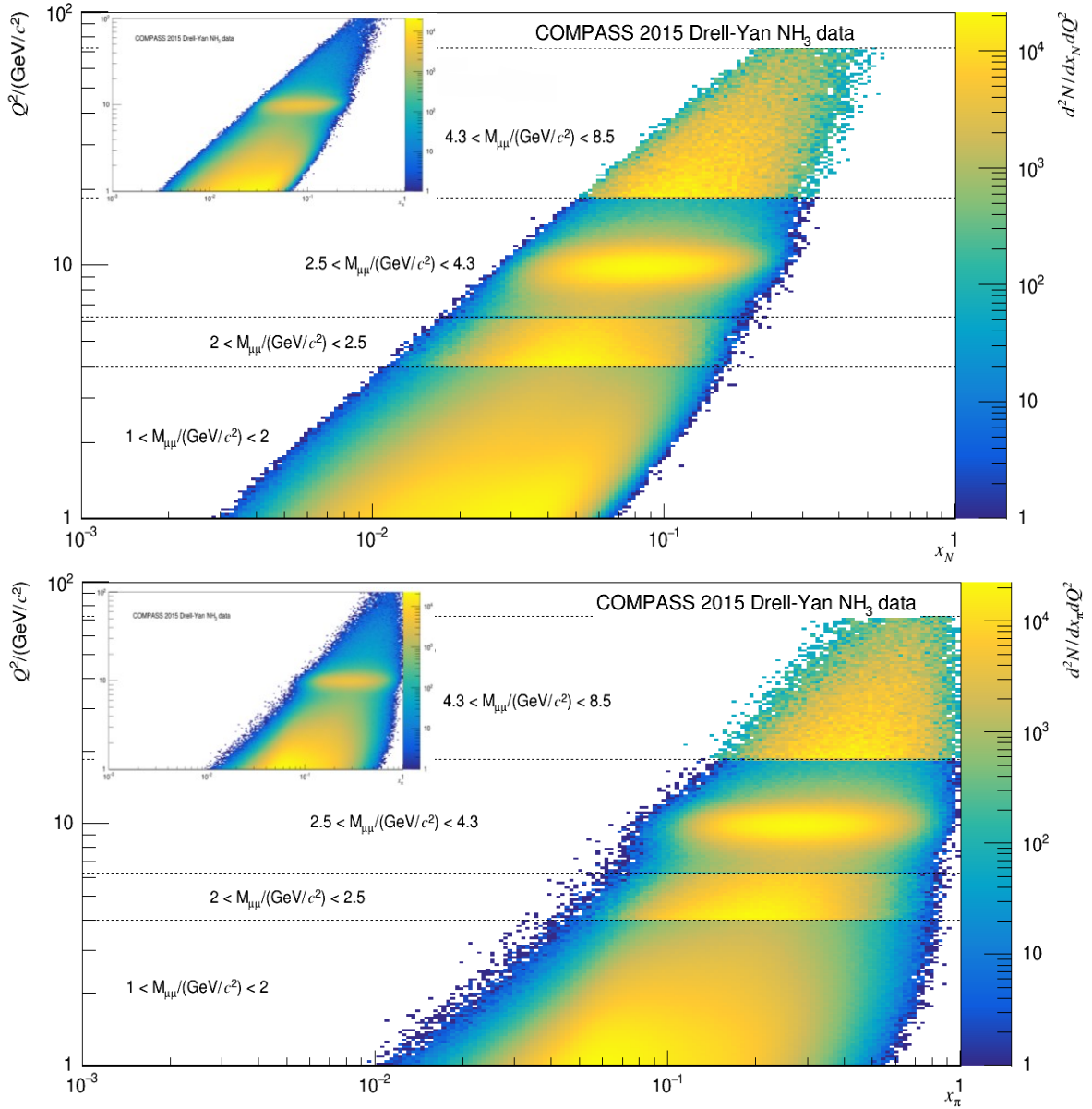

Figure 3.5: The distribution of x_N versus Q^2 (upper figure) and x_π versus Q^2 (lower).

The transverse spin asymmetries were extracted using the one-dimensional (1D) analysis procedure using the double ratio (DR) method. Let us recall that the target contains two oppositely polarised cells, and also every period consists of two sub-periods with the opposite target polarisation (see the Table 3.3). The DR combines the information from the sub-period and the cell polarisation. The advantage of this method lies in that it allows to reduce the systematic effects of the different acceptance in the target cells to minimum. Using the eq. (1.73) for the DY cross-section, we can define the counting rate N^{sc} dependent on Φ_i, where s is the given sub-period ($s = 1$, 2) and c stands for the target cell with polarisation up or down w.r.t. the target magnetic field ($c = \uparrow, \downarrow$), and Φ_i is either of the cross-section angles ϕ_s, $2\phi + \phi_s$, $2\phi - \phi_s$:

$$N^{sc}(\Phi_i) = F^{sc} n^{sc} a^{sc}(\Phi_i) \sigma(1 \pm W_i(\Phi_i)),$$ (3.1)

where F^{sc} is the particle flux, n^{sc} is the density of the target for the given cell and polarisation in the given sub-period, a^{sc} denotes the acceptance dependent on the Φ_i for the cell and the sub-period polarisation, and W_i stands for a modulation of the Φ_i for a particular asymmetry [56]. Hence, the ratio evaluation is built as follows:

$$R(\Phi) = \frac{N^{1\uparrow}(\Phi) N^{2\uparrow}(\Phi)}{N^{1\downarrow}(\Phi) N^{2\downarrow}(\Phi)}.$$ (3.2)

With the corresponding error of double ratio given as:

$$\sigma_{DR} = \sqrt{\frac{1}{N^{1\uparrow}} + \frac{1}{N^{2\uparrow}} + \frac{1}{N^{1\downarrow}} + \frac{1}{N^{2\downarrow}}}.$$ (3.3)

After the substitution of the expression (3.1) to (3.2) we get:

$$R(\Phi_i) = \frac{F^{1\uparrow} n^{1\uparrow} a^{1\uparrow}(\Phi_i)(1 + W_i(\Phi_i)) \cdot F^{2\uparrow} n^{2\uparrow} a^{2\uparrow}(\Phi_i)(1 + W_i(\Phi_i))}{F^{1\downarrow} n^{1\downarrow} a^{1\downarrow}(\Phi_i)(1 - W_i(\Phi_i)) \cdot F^{2\downarrow} n^{2\downarrow} a^{2\downarrow}(\Phi_i)(1 - W_i(\Phi_i))},$$ (3.4)

which can be written as follows:

$$R(\Phi_i) = C_F C_a \frac{(1 + W_i(\Phi_i))(1 + W_i(\Phi_i))}{(1 - W_i(\Phi_i))(1 - W_i(\Phi_i))},$$ (3.5)

where $C_F = \dfrac{F^{1\uparrow} F^{2\uparrow}}{F^{1\downarrow} F^{2\downarrow}}$ and $C_a = \dfrac{a^{1\uparrow}(\Phi_i) a^{2\uparrow}(\Phi_i)}{a^{1\downarrow}(\Phi_i) a^{2\downarrow}(\Phi_i)}$. If we apply the target selection criteria for the dimuon events which will be elaborated below, in the Section 3.4, then the beam flux is approximately constant in both of cells, thus C_F is equal to 1. Now, we can perform the Taylor expansion of (3.5) resulting in:

$$R(\Phi_i) \cong C_a \cdot (1 + 4W_i(\Phi_i)).$$ (3.6)

Then, we can apply a reasonable assumption that the ratio of acceptances in two sub-periods is the same for events coming from the upstream and downstream cell in each Φ_i bin:

$$\frac{a^{1\uparrow}(\Phi_i)}{a^{2\downarrow}(\Phi_i)} = \frac{a^{1\downarrow}(\Phi_i)}{a^{2\uparrow}(\Phi_i)} . \tag{3.7}$$

Under this assumption the acceptances in the C_a cancel out and C_a is also equal to one. One then has:

$$R(\Phi_i) \cong const \cdot \left(1 + 4W_i(\Phi_i)\right). \tag{3.8}$$

The calculation of the double ratio quantities in usually done in 16 bins over the range $(-\pi, \pi)$ [56], but since our statistical sample is not very large, we used 8 bins instead. Then, the amplitudes of the corresponding Φ_i can be extracted from a fit with the following function:

$$R(\Phi_i) \cong par[0] \cdot \left(1 + 4 \cdot par[1] \cdot \sin(\Phi_i)\right), \tag{3.8}$$

where the fitting parameter [0] corresponds to the constant in the eq. (3.8) and should be equal to one to fulfil the conditions for using the DR method, while parameter [1] denote directly the requested raw asymmetry. The fit has been performed using the χ^2-minimalisation method. The major advantage of the DR method is that the acceptances, only achievable by precise MC, are factored out. Also it combines all the data from the two target cells and has very soft requirements [56]. Its disadvantage is a higher systematic effect when using in a smaller statistical sample where some slight deviations from the assumption (3.7) start to appear. The illustration of fitted modulation for the pretzelosity asymmetry in the $M_{\mu\mu}$ variable can be seen in the figure 3.6.
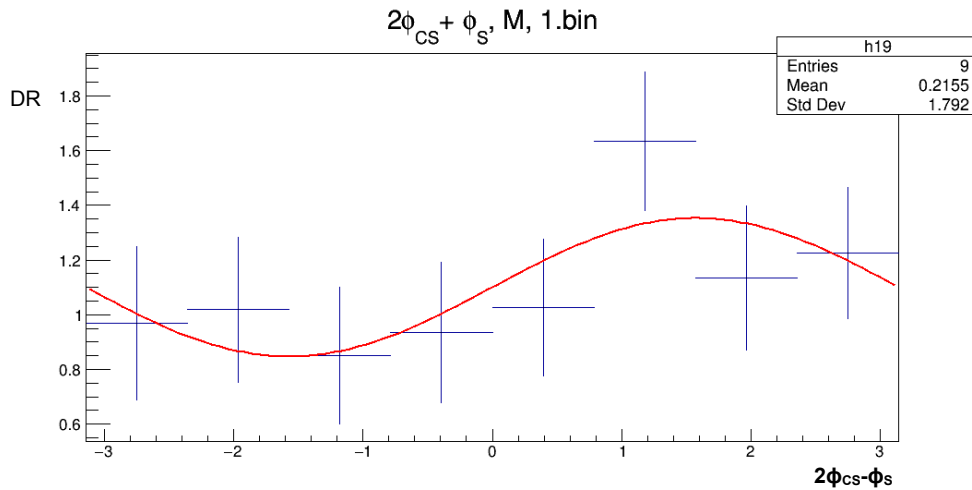

Figure 3.6: The double ratio fit of the modulation of the $\Phi = 2\phi + \phi_s$ angle describing the pretzelosity asymmetry in $M_{\mu\mu}$ variable for the first kinematical bin.

3.2.1 The Correction factors of the measured asymmetries

The measured asymmetry, which we obtain from the fit (3.8), is not the actual physical asymmetry; this raw asymmetry has to be corrected by the target inefficiencies, i.e. the level

of target polarisation $|S_T|$ and the dilution factor f of the target material, and for the depolarisation factor $D_{f(\theta)}$ from the DY cross-section (1.73):

$$A_i^{raw}(\Phi_i) = A_i(\Phi_i)\langle D_{f(\theta)}^n \rangle \langle |S_T| \rangle \langle f \rangle, \tag{3.9}$$

where the $D_{f(\theta)}$ is calculated event-by-event, S_T is given run-by-run, but in the practical calculation the mean value for a whole period of both of them and the dilution factor f is used. The n denotes the kinematic bin where the mean value if the $D_{f(\theta)}$ is calculated. In order to obtain the real value of the asymmetry $A_i(\Phi_i)$ the raw asymmetry has to be divided by the three described factors.

The measurement of the target polarisation was provided by 5 NMR coils installed in every target cell. The polarisation has shown to be inhomogeneous in the target mainly due to the heat deposited in the target material by the beam and the secondary particles, the deviation from the optimal DNP radiofrequency, or the non-uniformity of the solid ammonia in the cells [53]. In the previous COMPASS measurement the differences in the measured values of polarisation by each of the coils were in order of few %, however in the 2015 DY measurement the discrepancy showed to be up to 13% thus the simple average of the polarisation values could not be used. The PT group came with the solution of target polarisation as a function of z coordinate in the target cells. The polarisation was interpolated between the coils as a linear function (so-called Zigzag method, [53]). In time as the polarisation measurements were performed only before and after every period, not during the data-taking. The polarisation value during a period was interpolated by a decreasing exponential: $P(t) = P_0 \exp(-t/\tau) + P_{TE}$, where P_{TE} is the polarisation at the thermal equilibrium and the relaxation time τ indicates the loss of polarisation. The figure 3.7 shows the measurements of the polarisation for all the periods and coils. The table 3.3 shows the average values of the polarisation for the data sample for all the periods, which is also illustrated on the figure 3.8. The uncertainty of the target polarisation is estimated to 5%.

W07	W08	W09	W10	W11	W12	W13	W14	W15	Overall average
0.75	0.74	0.75	0.73	0.72	0.70	0.72	0.72	0.73	0.73

Table 3.3: The average values of the target polarisation for all the data-taking periods, together with the average value for the entire data sample.

Let us recall that the dilution factor describes the polarizability of the nucleons in the target material (see Section 2.3.1). Its values were obtained for every event by the PHAST function PaAlgo::GetDilutionFactor and their mean value for all of the 3 bins of each

kinematical variable was used for a correction of the raw asymmetries. The overall mean value of the dilution factor for the three bins of every kinematical variable is depicted in the lower band of the figure 3.9. The error of determining the dilution factor f is ~5% [53].
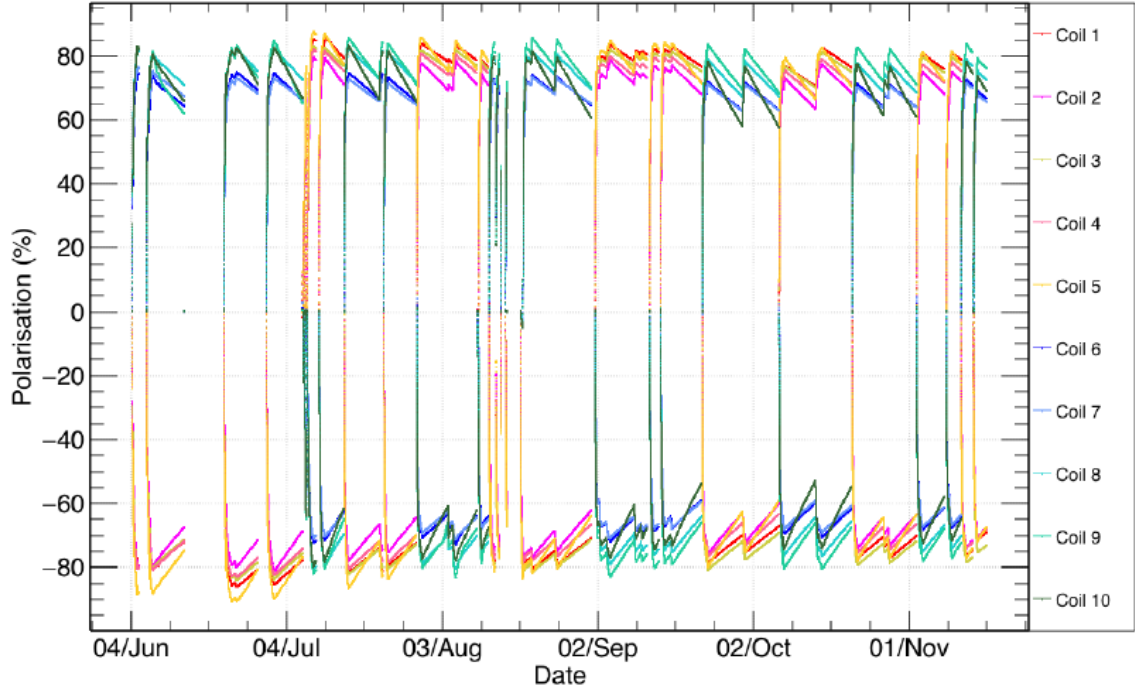

Figure 3.7: The target polarisation level for all the NMR coils interpolated between the beginning and the end of the data-taking periods. Taken from ref. [53].

The depolarisation factor $D_{f(\theta)}$ was defined in the Section 1.4. As can be seen from the DY cross-section (1.73), the depolarisation factor stands only before the pretzelosity and transversity asymmetry, namely the $D_{[\sin^2(\theta)]} = \dfrac{\sin^2(\theta)}{1 + \cos^2(\theta)}$ with the assumption $A_U^{1\,LO} = 1$.
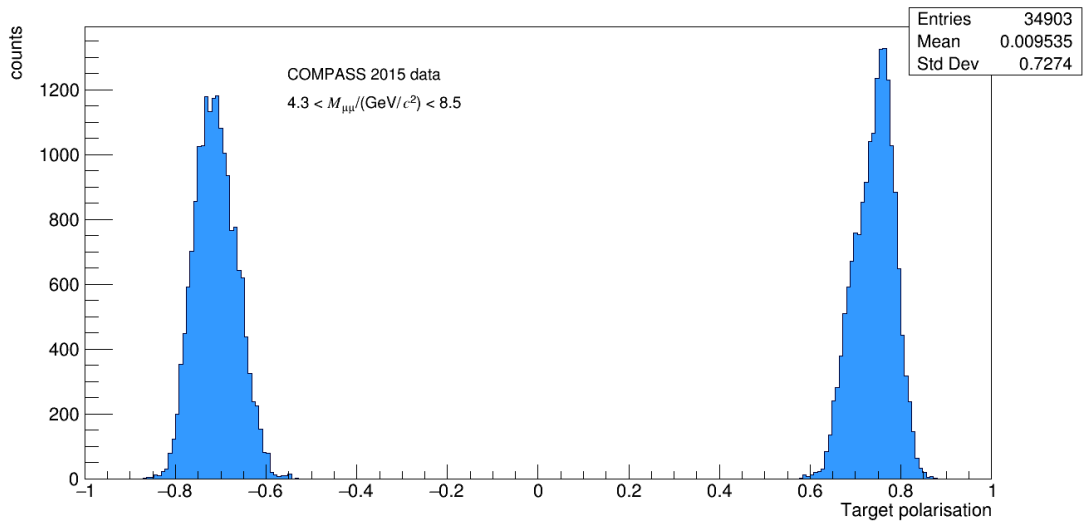

Figure 3.8: The interval of the values of target polarisation for the entire data sample.
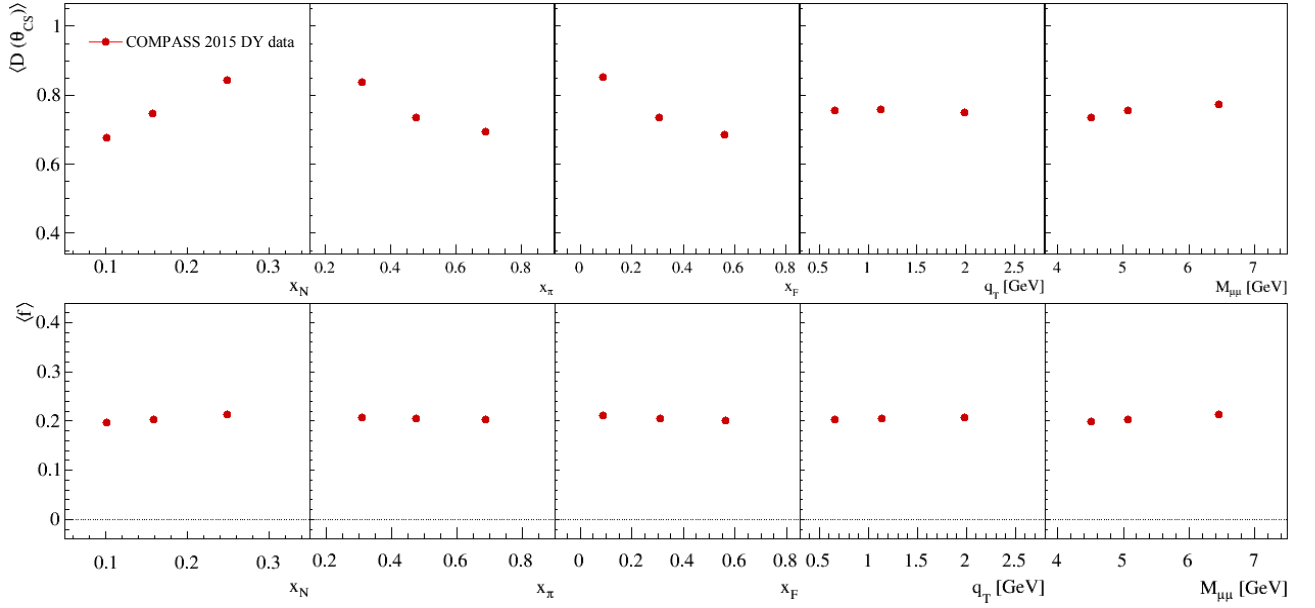
Figure 3.9: Average depolarisation factor (upper band) and the dilution factor (lower band) as a function of all the kinematical variables.

The correction was applied the same way as for the dilution factor, the mean value for every kinematical bin was used. The mean values for all the data are depicted in the upper row of the figure 3.9.

3.4 The Data sample

The actual data collecting after the commission and additional tuning took place since the 8th of June to 12th of November, i.e. the 9 periods having 2 weeks each. These data has been recorded under sufficiently stable conditions and are suitable for the physics analysis. The data taking periods with the corresponding polarisation state can be seen in the table 3.4. Except of the NH_3 target used for the polarised measurement, also the alumina and tungsten part of the absorber can be used as target for the unpolarised DY studies as it produces quite high statistics, as can be seen in the figure 3.14, however the vertex resolution is much worse.

Period	Sub-period	Polarisation state	Duration
W07	SP1	↓↑ (+-)	9.-15. July
	SP2	↑↓ (-+)	16.-22. July
W08	SP1	↑↓ (-+)	23.-29. July
	SP2	↓↑ (+-)	29. July-5.August
W09	SP1	↓↑ (+-)	5.-12. August
	SP2	↑↓ (-+)	12.-26. August
W10	SP1	↑↓ (-+)	26. August-1.September
	SP2	↓↑ (+-)	4.-9. September
W11	SP1	↓↑ (+-)	11.-22. September
	SP2	↑↓ (-+)	23.-30. September

W12	SP1	↑↓ (-+)	30. September-7. October
	SP2	↓↑ (+-)	8.-14. October
W13	SP1	↓↑ (+-)	15.-21. October
	SP2	↑↓ (-+)	22.-28. October
W14	SP1	↑↓ (-+)	28. October-2. November
	SP2	↓↑ (+-)	4.-8. November
W15	SP1	↓↑ (+-)	9.-11. November
	SP2	↑↓ (-+)	12.-16. November

Table 3.4: 2015 data-taking periods with the corresponding target polarisation state. Note that the direction of the transverse polarisation sign is defined with respect to the dipole field, not the LAB, and as the dipole field for the DY data-taking was oriented from up to down, thus the spin orientation ↓ corresponds to the positive one, and vice versa.

The analysis was performed on the data sample from the third mDST production (the first two were test productions which served tuning of the reconstruction parameters), which was finished on the beginning of September in 2016.

3.4.1 The Data stability studies

The produced data had to be checked by multiple tests for their stability. The following sub-section will shortly review the results of the tests ran by the collaboration [57],[58]. The stability test monitored variables which are correlated with the stability of the setup and are essential for the analysis. The tests have been performed spill-by-spill and run-by-run with a special software package used for the COMPASS data quality check (see [53]) adjusted for the DY measurement. The subject of the monitoring were the ratio of the beam particle flux and number of detected events and vertices, the ratios of the outgoing particles with the number of events, the primary vertices, the χ^2 of the outgoing particles and of all the vertices, then ratios of number of both the positive and negative muons and the number of events, and of the number of the muons from the primary vertices and the number events. The trigger rates (LAST-LAST, LAST-MT, LAST-OT) were also taken into account. Those ratios should be stable during the whole data-taking. The reason for this condition is that the data from the bad spills/runs produce instability in the acceptance of the spectrometer in the monitored variables, thus the conditions for the double ratio method (see Section 3.3) are not fulfilled. Concerning the test for bad spills, the value of each of the monitored variables is compared with the values from neighbouring spills, 2500 past spills and 2500 spills following the one monitored. Then, if the values for the spill fit in the certain interval ("sigma box") at least a certain number of times – which is specified by "minimum number of neighbours" – then the spill is marked as good, in other case is bad and rejected from the analysis. The conditions for

the whole run (consisting of up to 200 spills) not to be rejected are at least 10 spills contain, and less than 70% of them rejected. The example of the spill stability test can is in the figure 3.10.
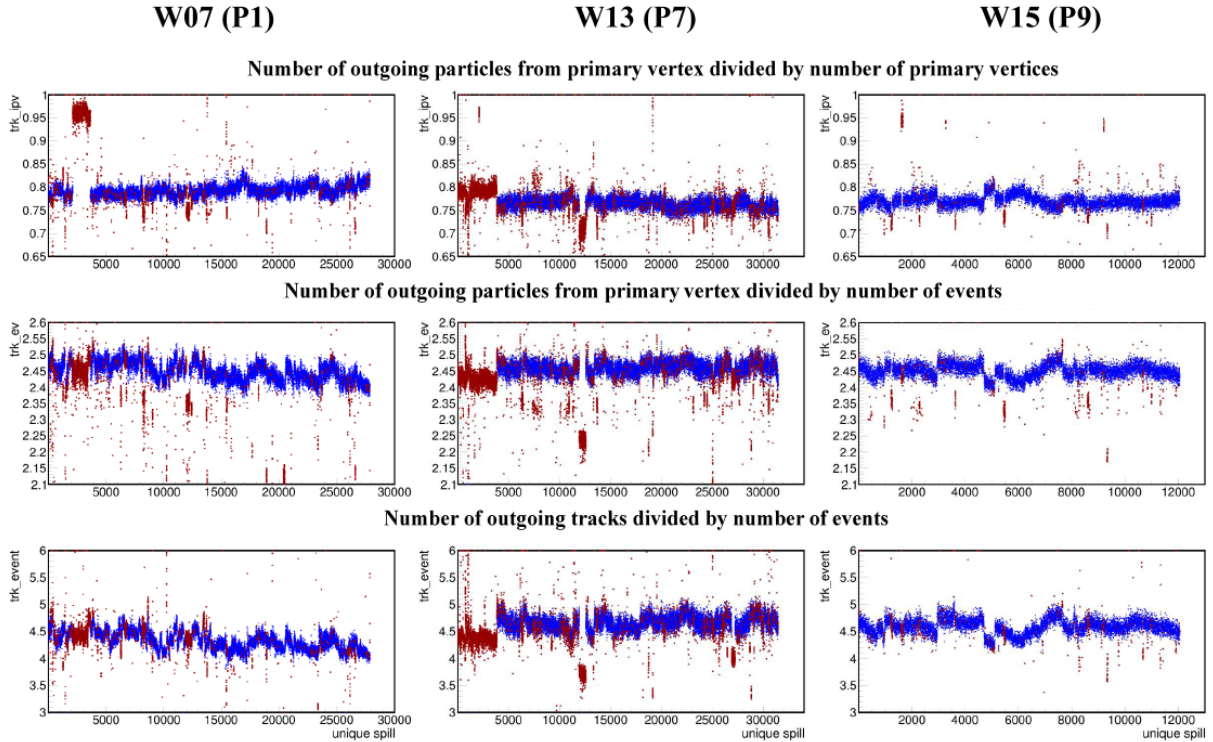

Figure 3.10: The spill-by-spill stability check of a three testing variables for three periods, the rejected spills are denoted in red. Taken from ref. [53].

Also the analysis of the data stability run-by-run was performed [57],[58]. Instabilities were sought in the major kinematic and angular variables (x_N, x_π, x_F, q_T, $M_{\mu\mu}$, the momenta of the particular muons, dimuons (virtual photons), or the beam, and the angular variables ϕ_s, ϕ, θ, or the angles in LAB), e.g. some deviations from the shape of distribution etc. Those runs, which are evaluated as incompatible (in a given variable) with most of the runs in the given period, are marked as bad.

Period	Bad spill	Bad spill/run
W07	11.79%	17.94%
W08	18.00%	21.19%
W09	14.76%	17.11%
W10	15.88%	17.80%
W11	22.49%	26.14%
W12	12.71%	13.79%
W13	22.32%	22.73%
W14	8.91%	10.70%
W15	3.94%	3.94%

Table 3.5: The percentage of the rejected spills from every period. In the last column is a ratio of the rejected spills versus rejected runs. Reproduced form the ref. [53].

Then, a comparison of the mean values of the observables is done. The run is marked as bad when the deviation of the observable mean value exceeds 5 standard deviations. Details on the evaluation can be found in [53]. An example of the run rejection on the basis of an observable mean value can be seen in the figure 3.11. The overview of the rejected spills and runs in the whole data set is given in the table 3.5.
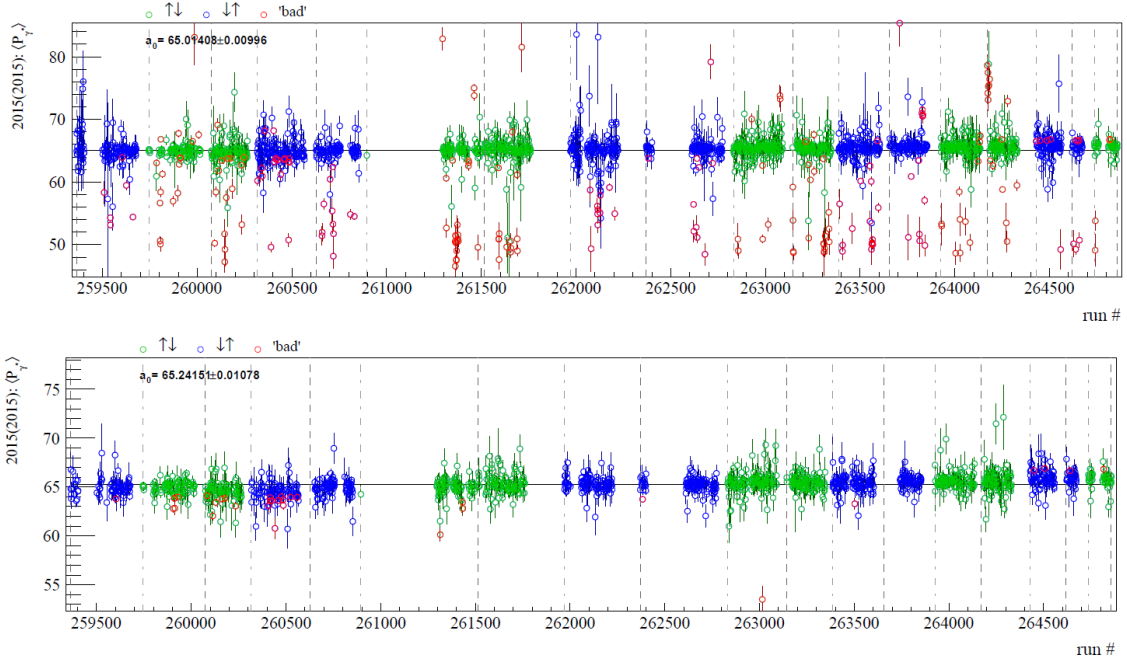

Figure 3.11: An example of run-by-run stability check in the mean value virtual photon momentum $P_{\gamma*}$ before (up) and after (down) the rejection.

The influence of the bad spills/runs rejection was tested on the asymmetries. The results of the test are shown in the figure 3.12. As can be seen in the figure, for the Sivers asymmetry (upper band) the results tend to be slightly higher (blue point for the sample with all spills/runs) then the final data (red points) but within the statistical error there is no real significance. In the case of the Pretzelosity and Transversity the data with no rejection show a certain reduction of the amplitudes but again, not statistically clear. However, using the bad spills/runs in the analysis would bring in a certain systematic effect (see [53]) which reflects the breaking of the conditions for using the double ratio method, mentioned above. The next figure 3.13 presents the pseudo-pulls of the filtered data with respect to all the spills/runs bin-by-bin. The *RMS* is slightly higher than 1 which indicates a lower statistical compatibility.
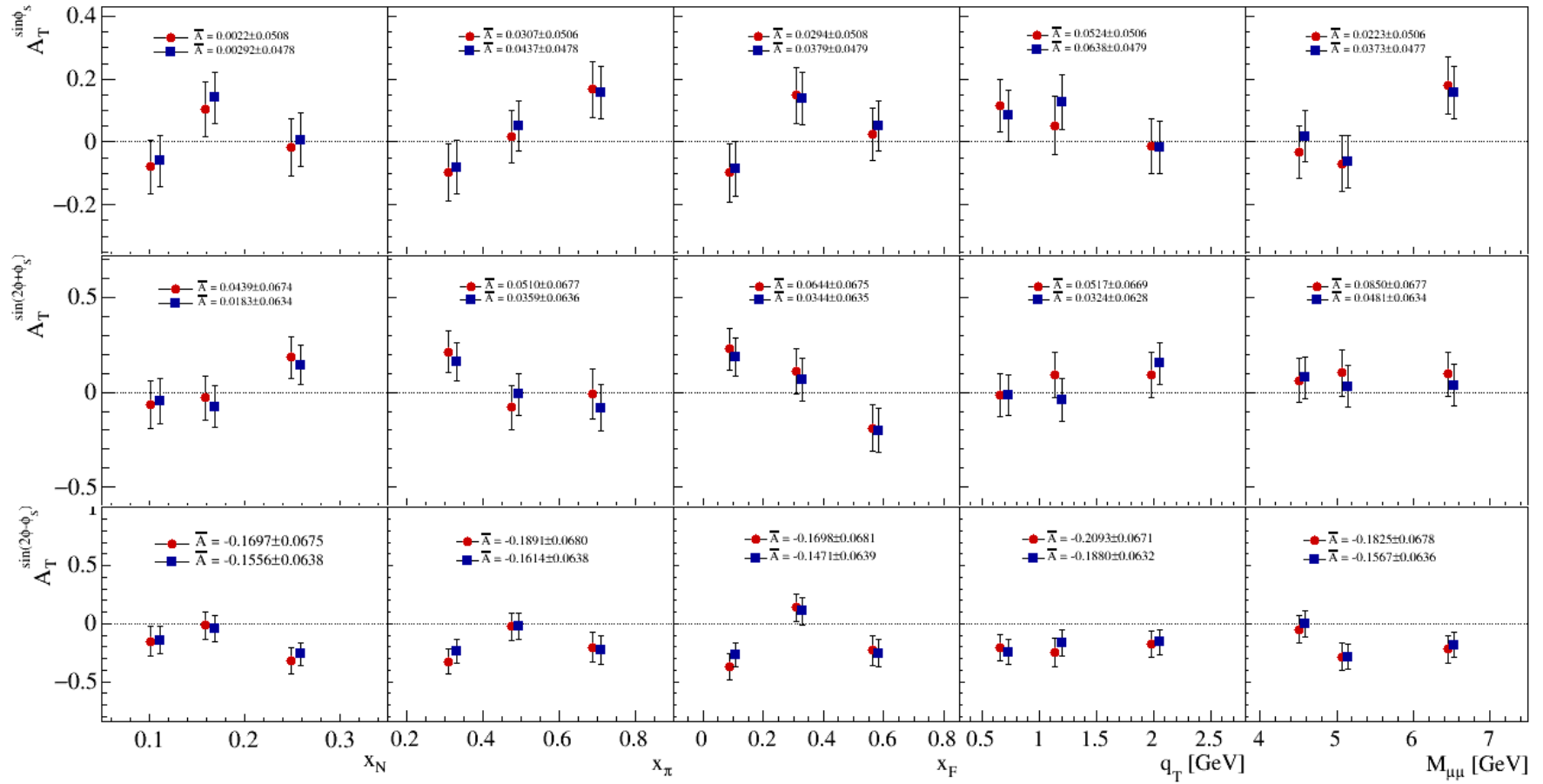
Figure 3.12: The influence of the bad spills/runs rejection on the asymmetries. The red points stand for the filtered data and the blue ones denote data with all the spills/runs.
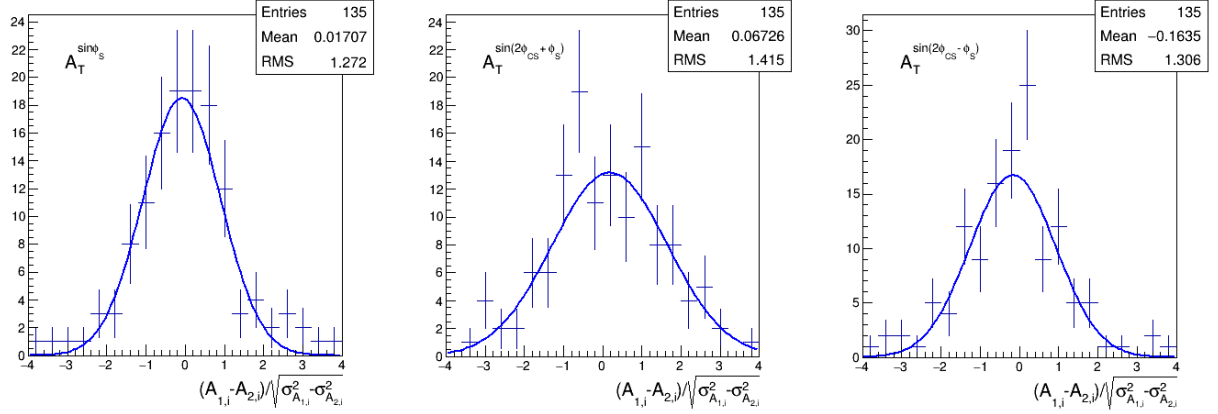
Figure 3.13: The pseudo-pulls of the comparison between the filtered data (denoted with subscript 1) and data from all the spills (subscript 2) bin-by-bin.

3.4.2. The Event selection

The data sample stored in the preselected μDSTs has to undergo a set of selection criteria to isolate the right muon pair candidates. The following list is the final version of the selection criteria used for both the official analysis [53], and the analysis presented in this thesis:

1. Dimuon candidates (particles crossing more than 30 X/X_0 (mean free path) with opposite charge) with the primary vertex. If there is more than one primary vertex, than the best primary vertex tagged by CORAL (the PHAST function PaVerttex::isBestPrimary()) is preferred. Otherwise, the primary vertex with the smallest vertex χ^2 is chosen. The requirement for the crossed radiation length denote that between the first measured point of the particle track and the last one the $\mu^{+/-}$ candidate crossed more than 30 radiation lengths in the spectrometer material. Also only the events from the high mass region 4.3 - 8.5 GeV/c^2 are chosen.

2. Only the events fired by the dimuon trigger are chosen, i.e. the coincidence of the fired LAST-LAST, LAST-OT triggers. As was already implied in the Section 2.2, the MT trigger was rejected at the end because it has been shown [59],[60] that the MT covers the phase space of the beam decay muons (BDM) as it is shown in the figure 3.14a. The removal of the MT replaced a former BDM cut on the negative muon momentum and theta.

3. Limits on the track of both muons: Z_{first} < 300 cm to ensure that the first measured point was before the SM1, and the last Z_{last} < 1500 cm to select the tracks with the last point passing through the Muon Filter 1.

4. The mean track time with respect to the trigger time is defined for both muons.

5. $\left| t_{\mu^+} - t_{\mu^-} \right| < 5\,\mathrm{ns}$ rejecting the uncorrelated pairs of muons (e.g. the positive muon from DY with the negative BDM one).

6. $\chi^2_{track} < 10$ which gives a limit on a quality of a muon track.

7. The trigger validation to ensure that the muons candidates are the ones that fired the dimuon trigger. In other words, if the extrapolated tracks of the muons fall in the active zone of dimuon hodoscopes that fired the signal.

8. The rejection of the bad spills or runs.

9. The cut on the physical value of x_N, x_π, and x_F, i.e. x_N, and $x_\pi \in [0,1]$ and $x_F \in [-1,1]$.

10. The transverse momentum of the dimuon pair in the CS frame $q_T \in [0.4,5]$. The lower limit is given by the resolution in the azimuthal angles which is less than 200 mrad (see the table 3.1), and the upper limit has a negligible significance as it only removes the tail of the high q_T.[17]

11. The z-position of the primary vertex of dimuon has to be within either of the two target cells: $Z_{vtx} \in [-294.5, 239.3] \| [-219.5, -164.3]\,\mathrm{cm}$. The gap between the cells is extended to reduce the number of the events migrating from one cell to another (see figure 3.17).

12. Radial cut on the target $R_{vtx} < 1.9\,\mathrm{cm}$ to cut off the beam halo and the reaction of the beam with the surrounding material which then ensures the validity of the assumption that the flux in the first cell is equal to the flux in the latter cell and C_F from the eq. (3.5) is 1.

The influence of the selection cuts on the statistics can be seen in the table 3.6. In the following, the influence of some cuts is presented and the resulting form of the kinematic and the angular variables (figures 3.18 and 3.19). The figure 3.15 shows the 2D projection of the X_{vtx} versus Y_{vtx} distribution of the coordinates of the vertex of all the events before the selection. The circle in the middle illustrates the beam radial cut (no. 12).

---

[17] In the TMD approach the condition of low q_T w.r.t. $M_{\mu\mu}$ has to be fulfilled (see Section 1.4) which is still true in our analysis as the $\langle q_T \rangle = 1.2\ \mathrm{GeV}/c^2$ and the $\langle M_{\mu\mu} \rangle = 5.3\ \mathrm{GeV}/c^2$.

	Cut	# Events	Statistics [%]
1.	$\mu^+ \mu^-$ pair ($X/X_0 > 30$) from primary vertex	1159349	100
2.	Dimuon trigger	868291	75
3.	$Z_{last} > 1500$ cm || $Z_{first} < 300$ cm	784379	68
4.	t_μ is defined	776643	67
5.	$|t_{\mu+} - t_{\mu-}| < 5$ ns	373081	32
6.	$\chi^2 < 10$	370054	32
7.	Trigger validation	169526	15
8.	Good spills only	138255	12
9.	$0 < x_N$ and $x_\pi < 1$, $-1 < x_F < 1$	138162	12
10.	$0.4 < q_T < 5$	124857	11
11.	$-294.5 < Z_{vtx} < -239.3$ || $-219.5 < Z_{vtx} < -164.3$	38197	3
12.	$R_{vtx} < 1.9$ cm	34903	3

Table 3.6: The impact of each selection on the statistics.

(a)

(b)
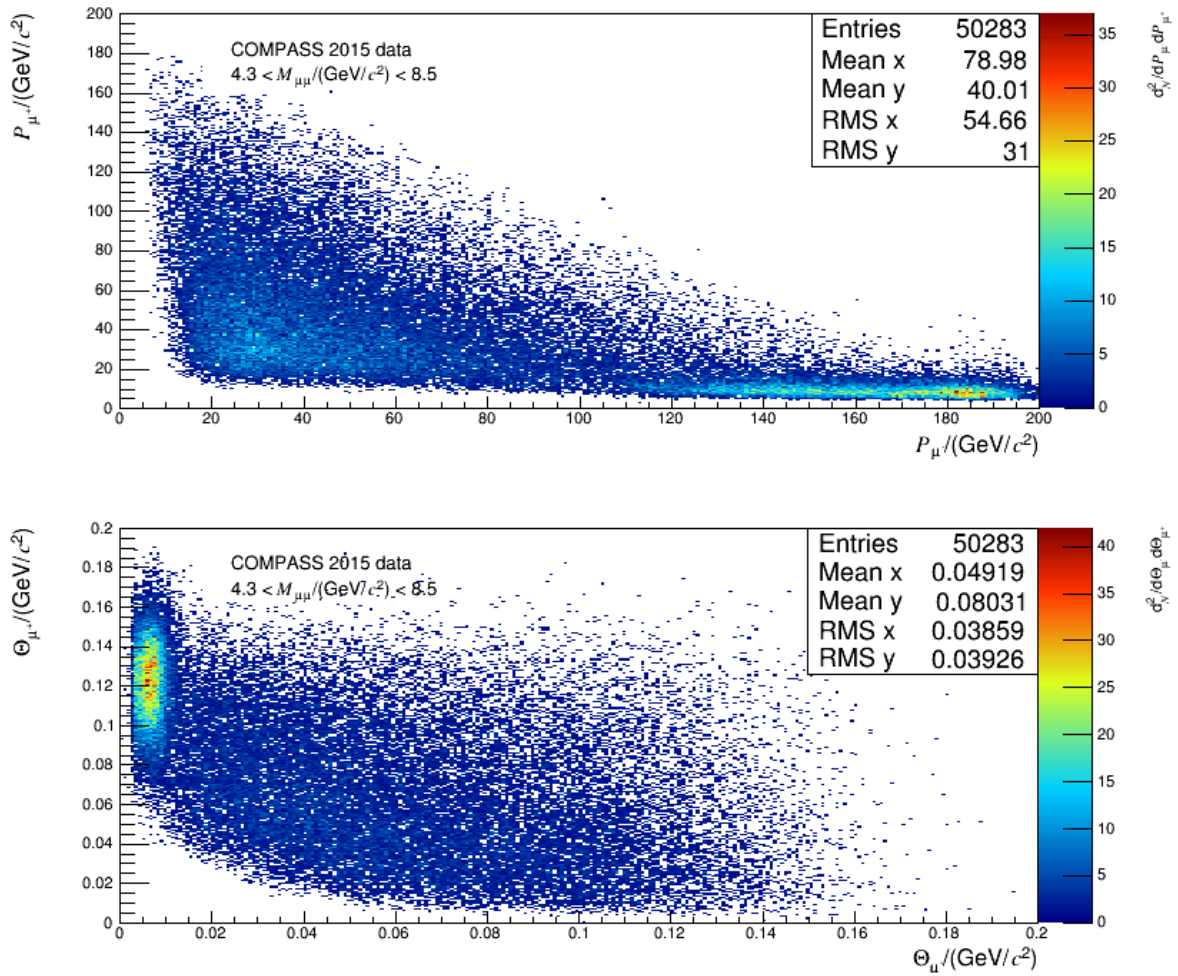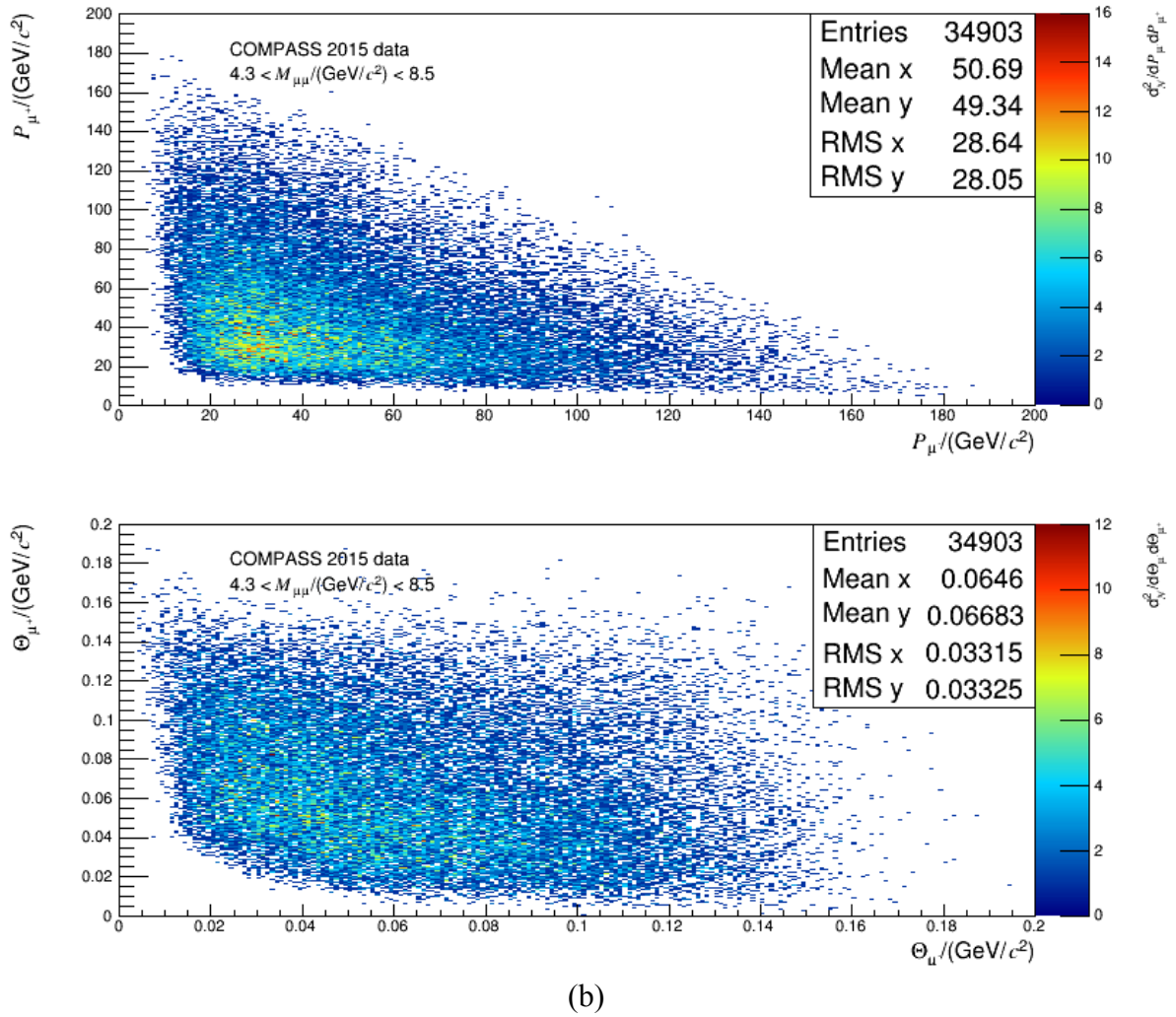
Figure 3.14: The distribution of the momentum of $P_{\mu+}$ versus $P_{\mu-}$ (upper from (a) and (b)) and $\theta_{\mu+}$ versus $\theta_{\mu-}$ (lower from (a) and (b)). The upper two figures (a) show the impact of the Middle trigger; one can see the appearance of the beam decay muons in the high μ^- momenta and low azimuthal angle. The lower two figures (b) demonstrate the resulting distribution after rejecting the MT, the distribution is μ^+/μ^- symmetric which indicates that the BDM are cut out.

Variable	Binning
x_N	0.00, 0.13, 0.19, 1.00
x_π	0.00, 0.40, 0.56, 1.00
x_F	-1.00, 0.21, 0.41, 1.00
q_T	0.4, 0.9, 1.4, 5.0 (GeV/c^2)
$M_{\mu\mu}$	4.3, 4.75, 5.5, 8.5 (GeV/c^2)

Table 3.7: The binning of the kinematical variables used for the analysis.

The kinematical variables used for the asymmetry extraction were divided in the 3 kinematical bins; the bin edges are shown in the table 3.7. The figure 3.16 demonstrates the cuts performed the isolate the NH$_3$ target area.
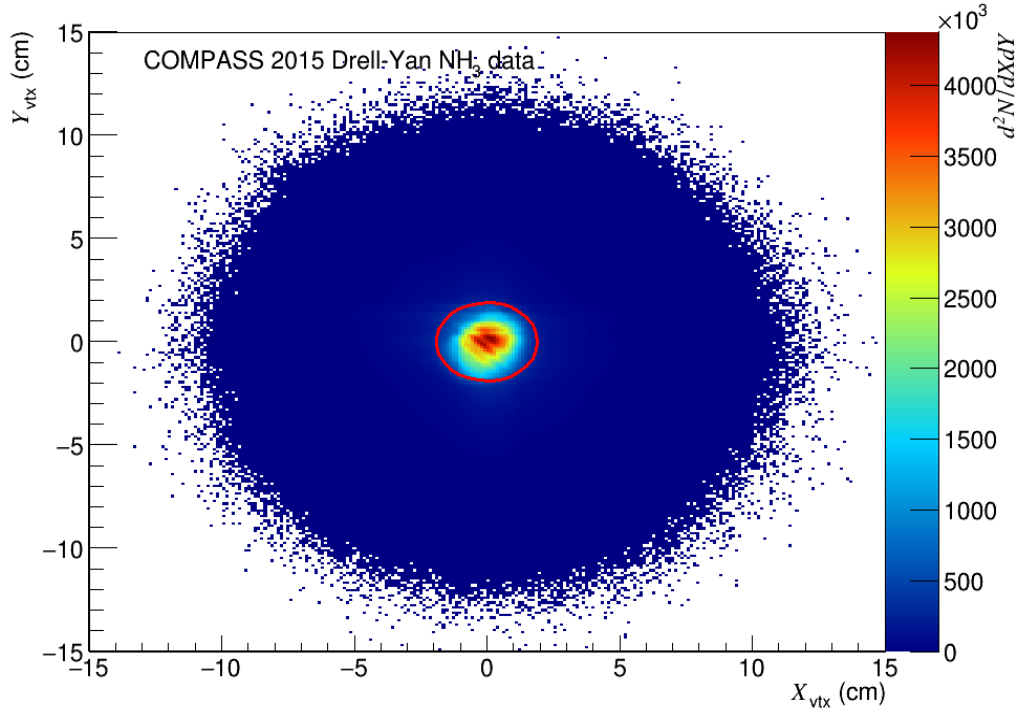
Figure 3.15: The 2D projection X_{vtx} to Y_{vtx} distribution of the data sample with the beam cut indicated by the red circle.
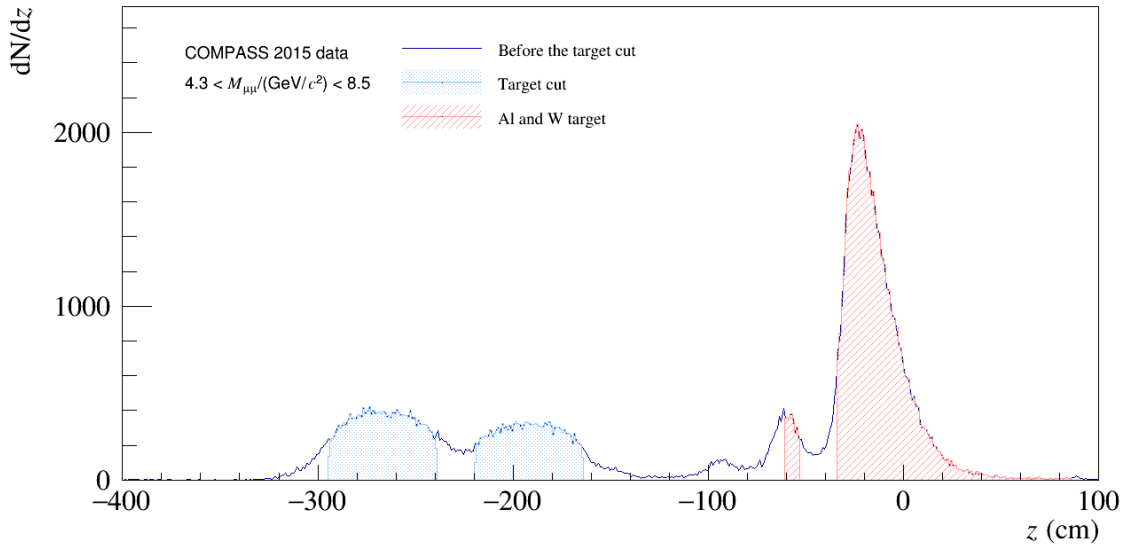

Figure 3.16: The Z_{vtx} position with the NH$_3$ target cut indicated by the blue filled area. The red filled area shows the positions of the Al target (the lower peak) and the W beam plug (the higher peak) in the absorber which can be used for the unpolarised studies.

On the figure 3.17 one can see the MC simulation of the contributions to the event migration from the first cell to the other. The migration from the cells in caused by the inefficiency in the Z_{vtx} resolution which is about 11 cm (see the table 3.1) in addition to the contribution of the events originated in the reaction with the liquid helium in the gap between the cells.
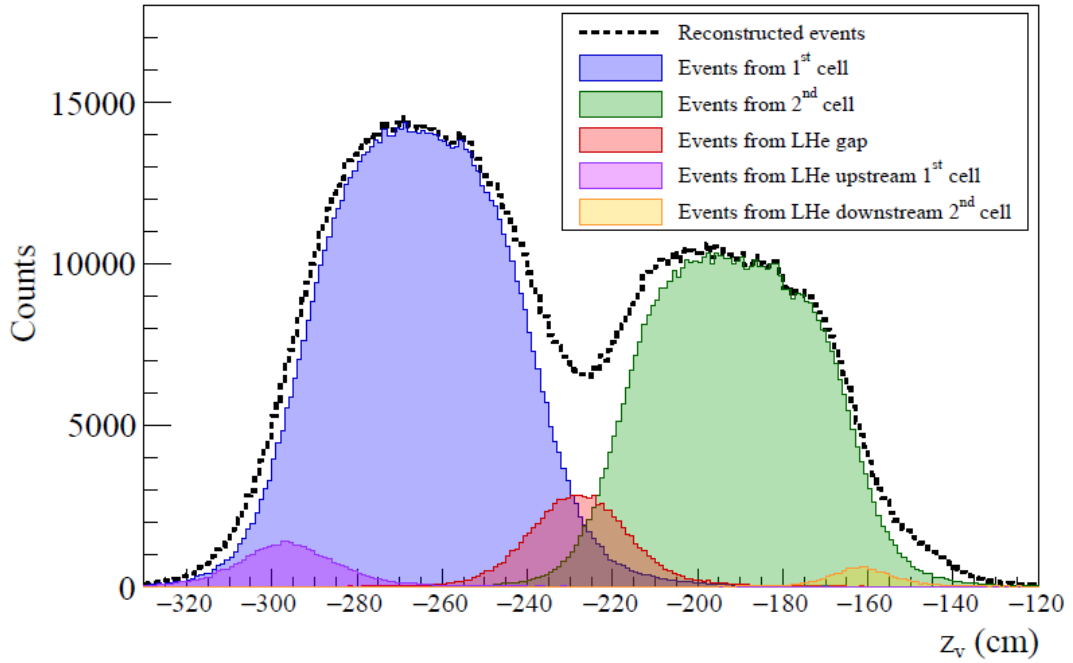
Figure 3.17: The event migration from cell to cell. Taken from the ref [53].
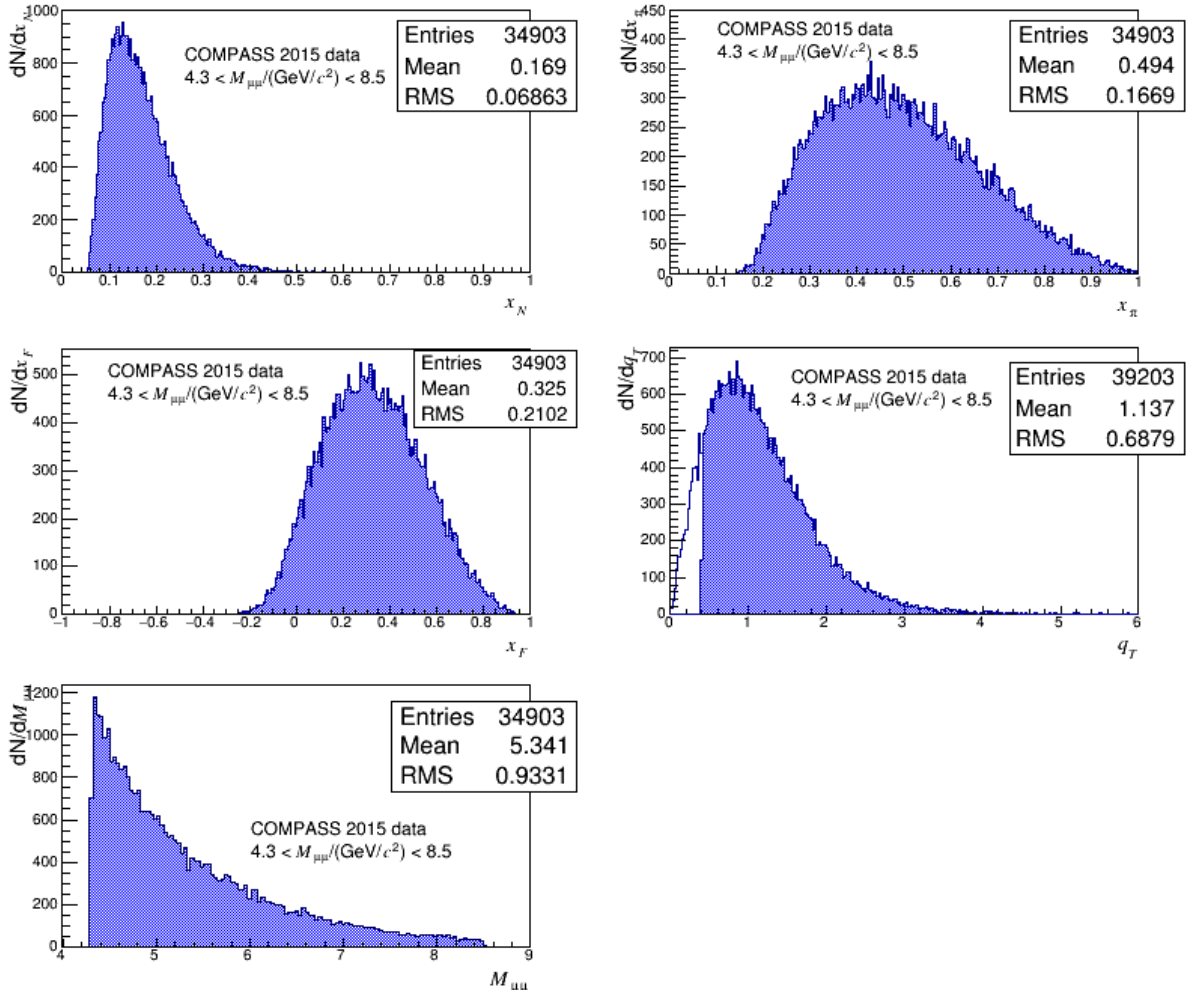

Figure 3.18: The kinematical variables: in the top band there are x_N and x_π; in the middle band x_F and q_T, in the latter the q_T cut (no. 10) is illustrated; and the lower stands for the $M_{\mu\mu}$.
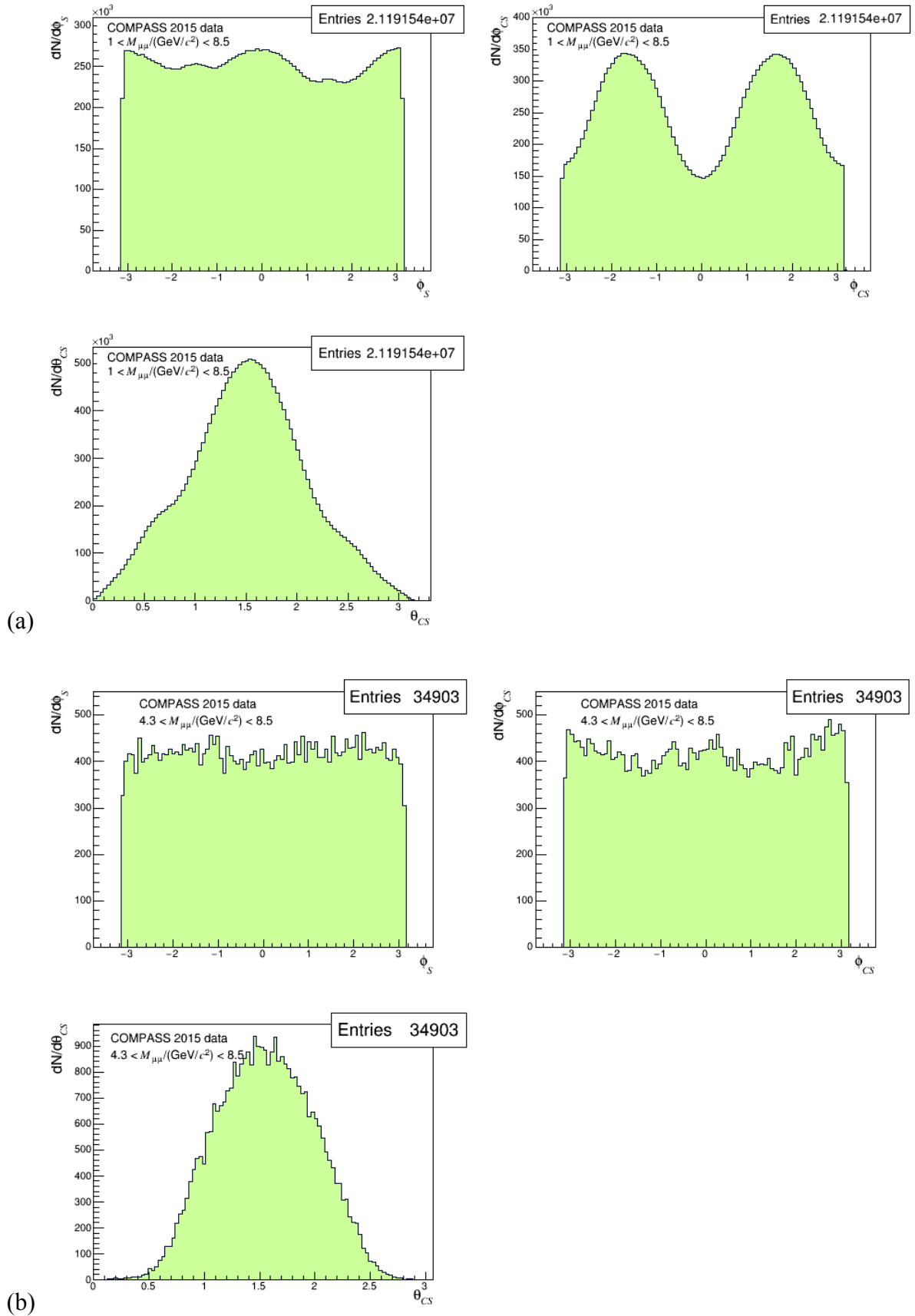
(a)

(b)

Figure 3.19: The azimuthal angles ϕ, ϕ_s, and θ distributions. One can see the influence of angular acceptance of the spectrometer for all the mass in the upper set (a), and for the high mass (b).

The following figures show the 2D distribution of the Bjorken variables for nucleon x_N and for the pion x_π for all the range of the dimuon spectrum $1 - 8.5$ GeV/c^2 (figure 3.20) and for the high mass region (figure 3.21). The lower figure demonstrates that the kinematic phase space measured at COMPASS DY program matches the valence region both of the nucleon and of the pion. In this region, the DY cross-section for a proton target is dominated by the contribution of nucleon u quark and pion $\bar{u}$ quark TMD PDFs.
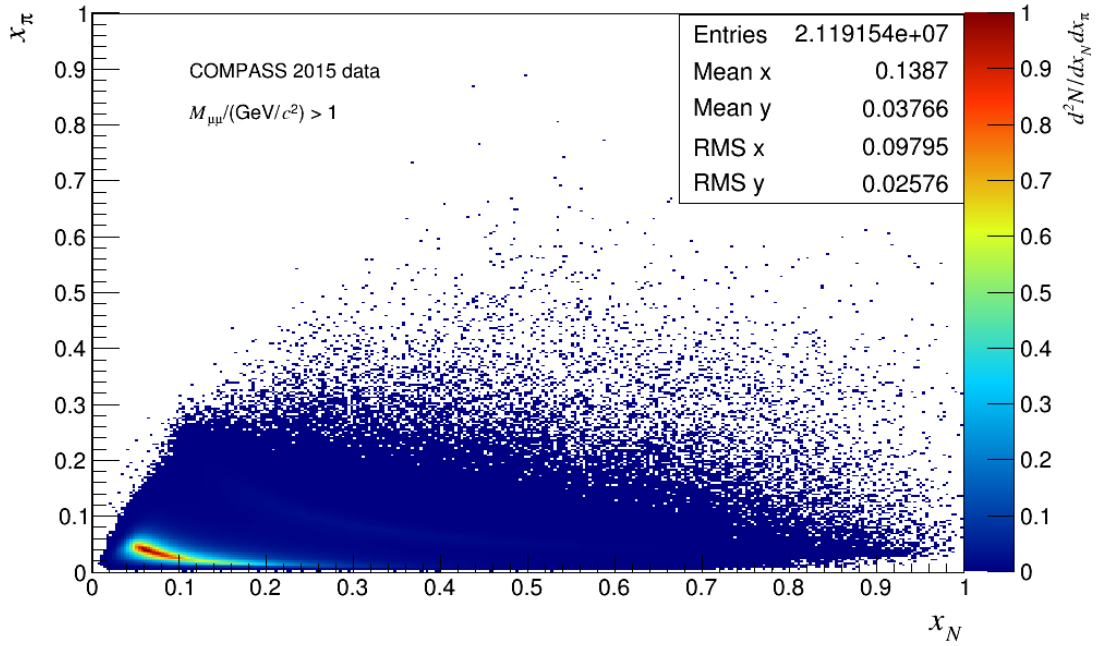

Figure 3.20: The phase space of the Bjorken variables of a nucleon x_N and the pion x_π for the dimuon spectra of $1 - 8.5$ GeV/c^2. Both the valence and the sea regions are populated.
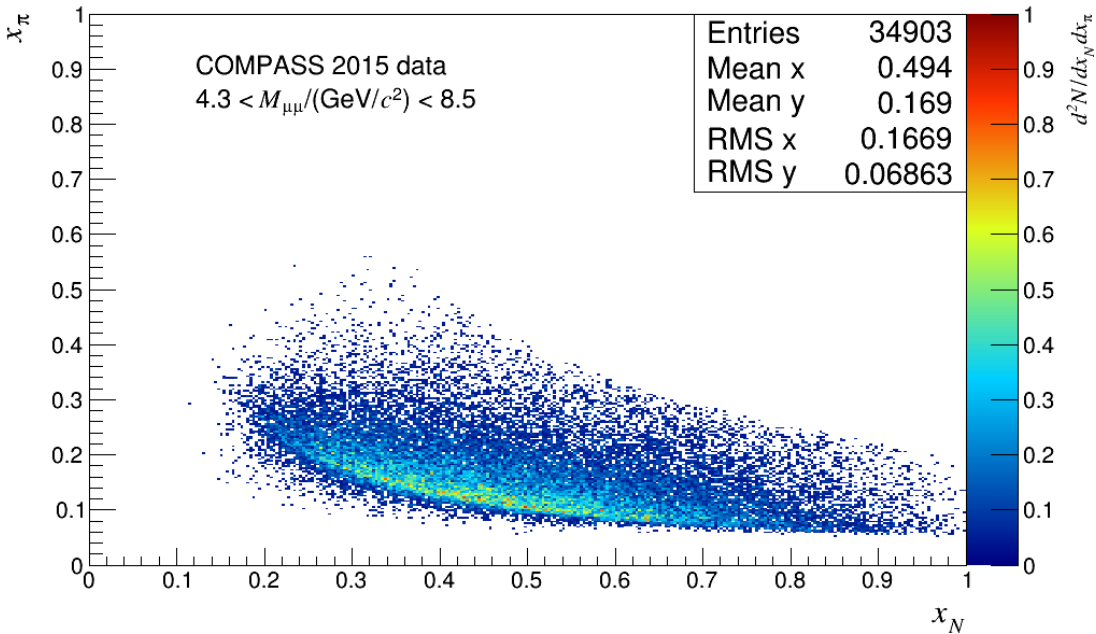

Figure 3.21: The phase space of the Bjorken variables of a nucleon x_N and the pion x_π for the high mass $4.3 - 8.5$ GeV/c^2. The asymptotes delimit the valence region of the N and π.
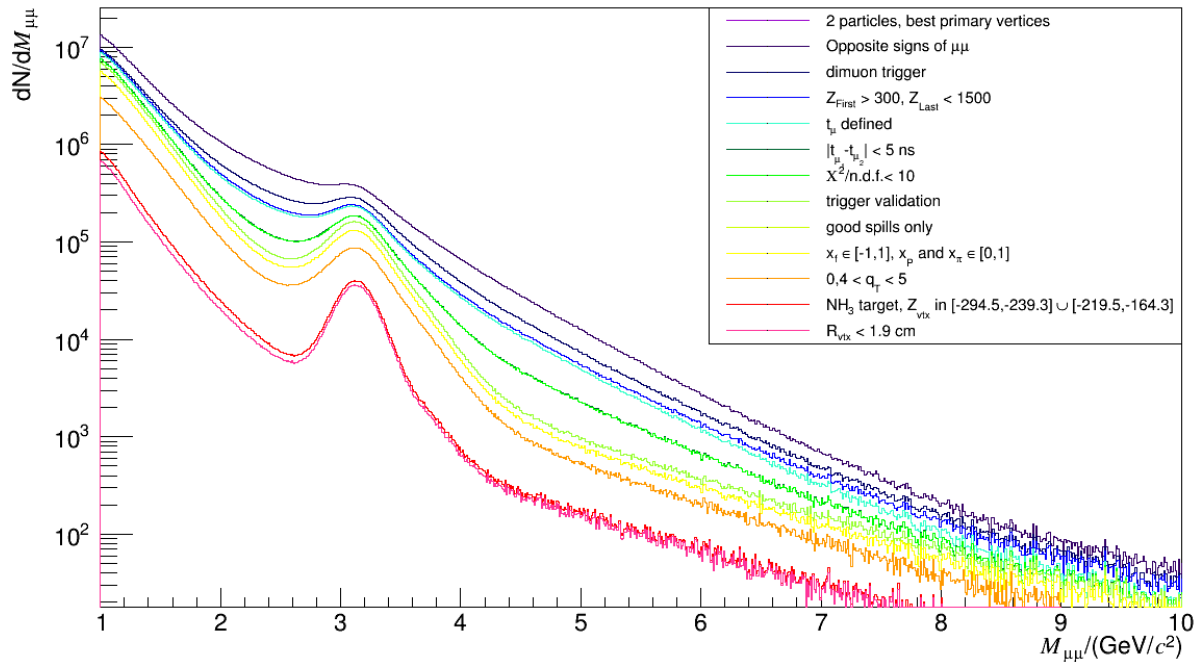
Figure 3.22: The impact of the selection criteria on the whole dimuon mass distribution.
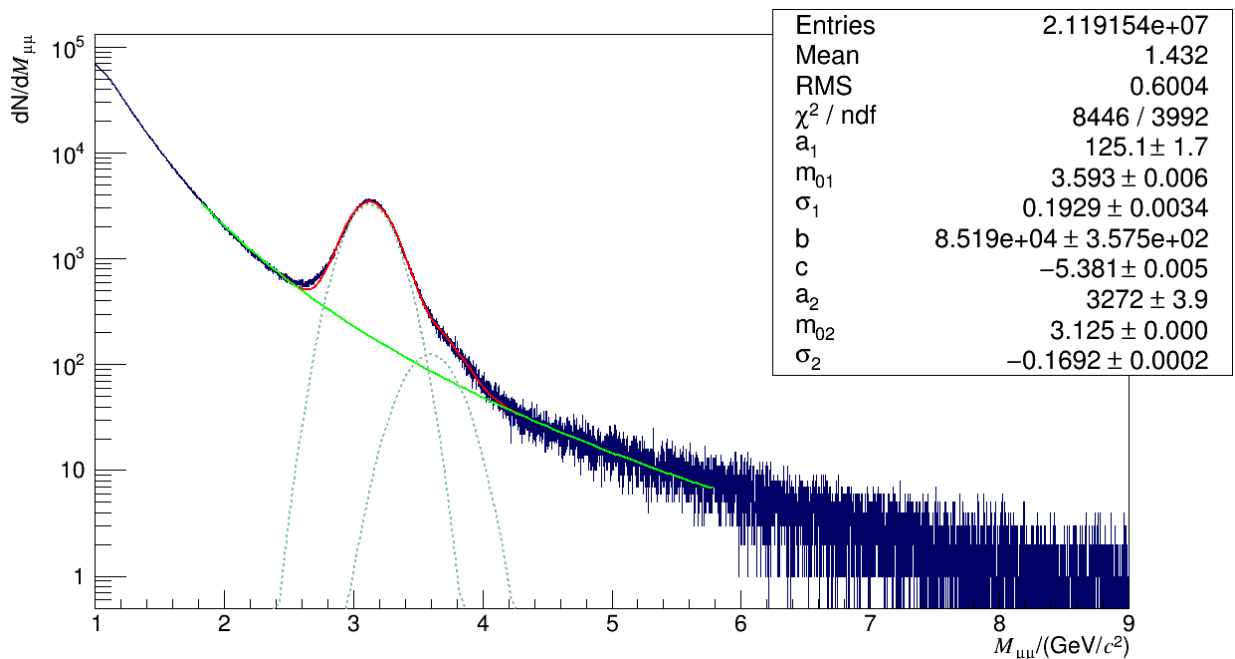

Figure 3.23: The dimuon invariant mass with the J/ψ (parameters with the subscript 1) and ψ' (subscript 2) peak fit versus the background (b and c parameters). a_1 and a_2 denote the amplitudes of the fits, m_{01} and m_{02} are the means, i.e. the mass of the J/ψ and the ψ', respectively, and σ_1 and σ_2 describe the resolution of their mass regions.

On the figure 3.22 the impact of the selections (except the high mass cut) is demonstrated. The final DY mass distribution after the cuts is shown in the figure 3.23 with the fit of J/ψ, ψ' peak and the background, the fit has the following form:

$$\text{gauss}(J/\psi)+b\cdot M_{\mu\mu}{}^{c}+\text{gauss}(\psi'). \tag{3.10}$$

The J/ψ and ψ' peak are fitted with the gauss function and *b* and *c* are the fitting parameters of the background.

3.5 The Systematic studies

In the following section are presented the systematic studies we have performed to determine the possible sources of the systematic error. We have checked the compatibility of the periods, and performed the false asymmetries test. The false asymmetries are considered to be the largest contribution to the systematic error [24]. The additional contributions to the systematic error are the errors of the target polarisation and dilution factor measurements which contribute to the systematic error by the simple error propagation. The error of the target polarisation measurement is 5% and the error of determining the dilution factor is also 5%.

3.5.1 The Compatibility of results from different periods

The results of the extracted asymmetries were compared period after period. The figure 3.24 shows the average of the three kinematical bins for every period and the fit with a constant function demonstrates the deviations of the periods. It can be seen that the deviations are merely statistical fluctuations and within the statistical error the whole data set is stable. The value of the average, i.e. the value of the fitting constant is shown in each plot. On the next figure 3.25 are the results of all periods in standard 3-bin representation. It can be seen that the values are compatible within the statistical errors as well as the average value in the figure 3.24. In the figure 3.26 are the pulls from the average value of each three asymmetries integrated over the kinematical bins are shown for all the 135 values (9 periods × 5 kinematical variables × 3 bins) for each asymmetry. The pulls were evaluated using the following formula:

$$Pull_{i} = \frac{A_{i} - \langle A \rangle}{\sqrt{\sigma_{A_{i}}^{2} - \sigma_{\langle A \rangle}^{2}}}. \tag{3.11}$$

The distribution of the pulls is well within the standard normal distribution *RMS* ≈ 1 and the mean value ≈ 0 which indicates the good compatibility of the results and the that deviations from the mean value have merely statistical origin. Thus, we can conclude the results of this test that there is no contribution of the period incompatibility to the estimate of the systematic error.
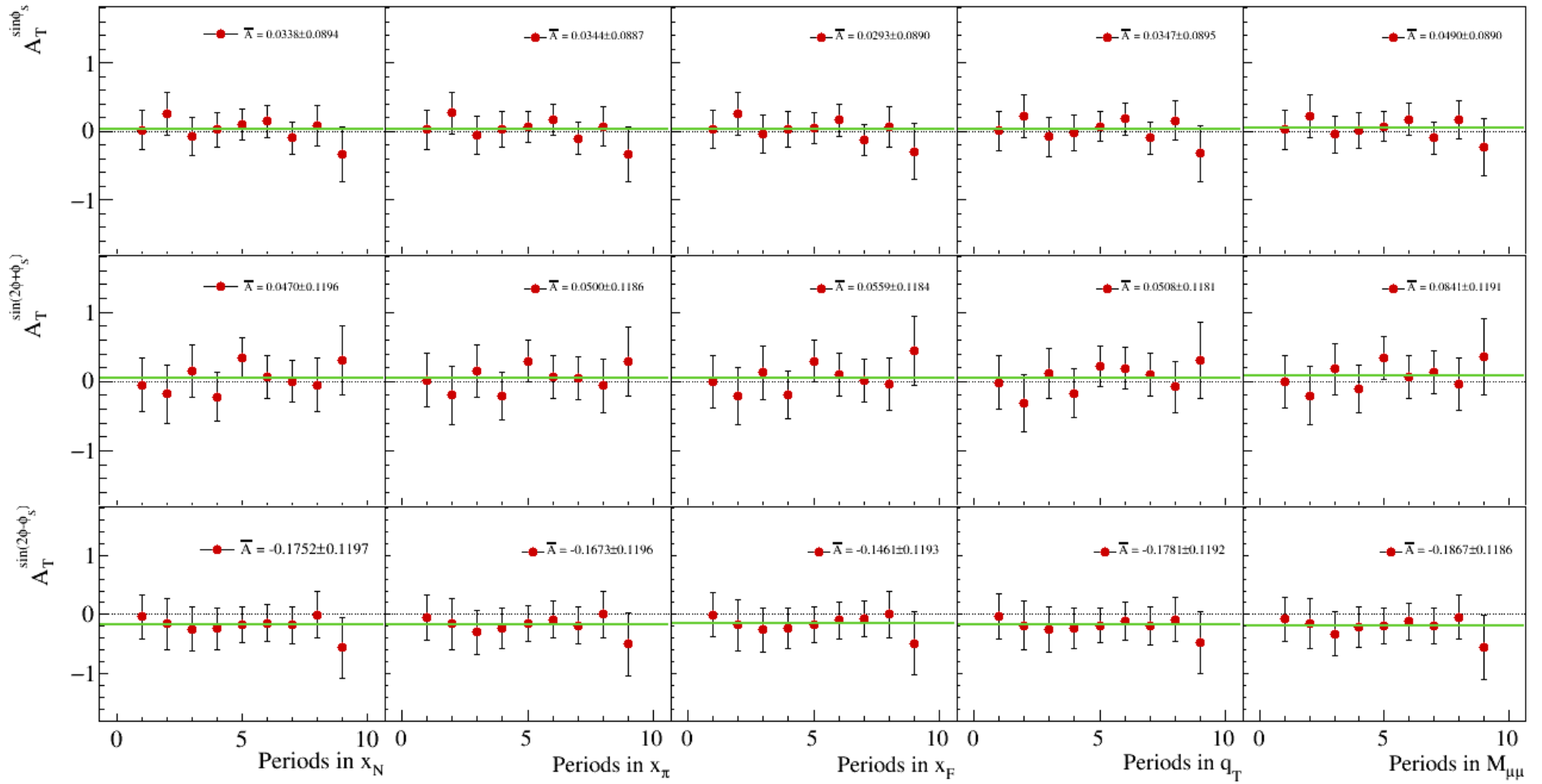
Figure 3.24: The averaged asymmetry per period fitted by a constant function. The value of the fitting constant is stated in the legend of every graph.
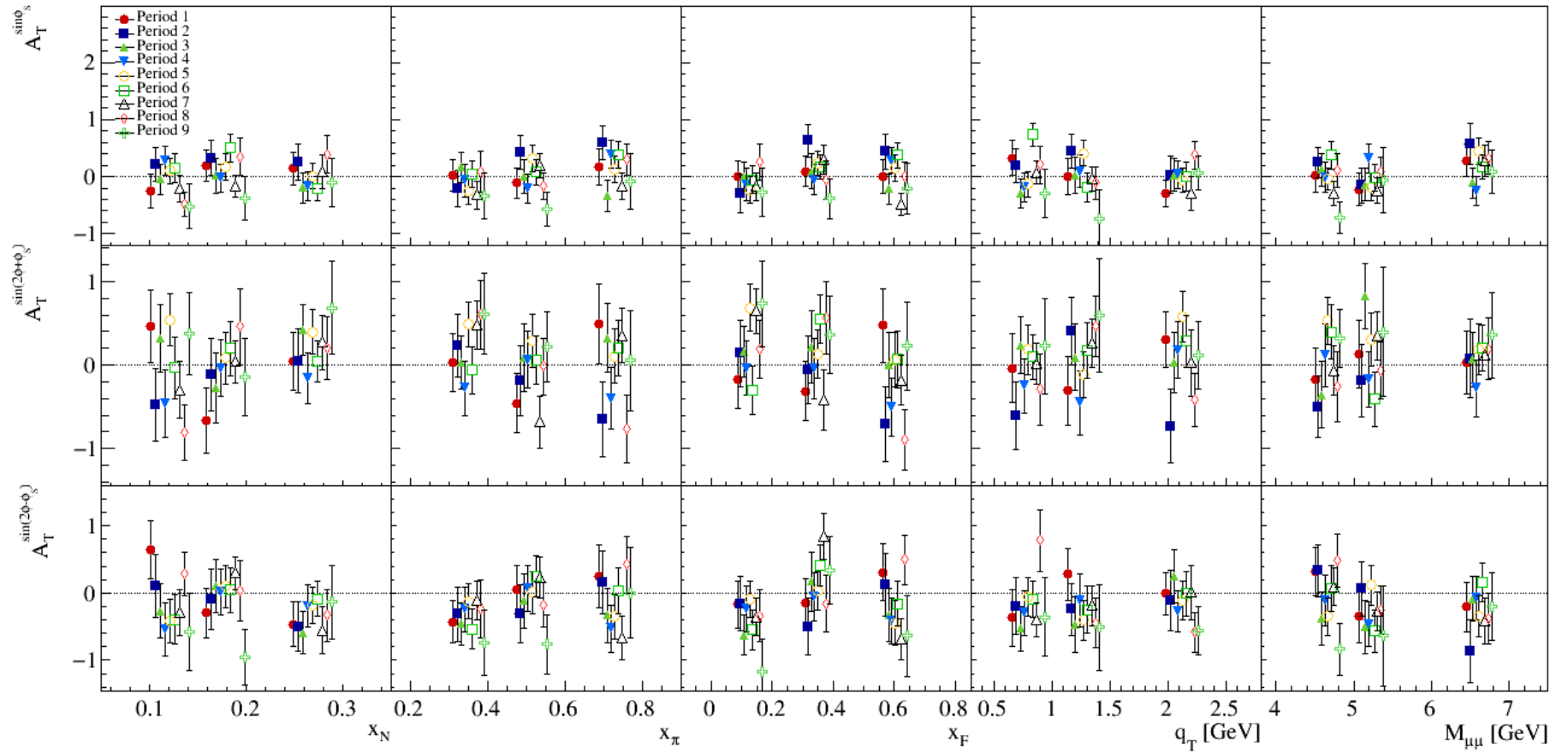
Figure 3.25: The complete set of results for all the 3 asymmetries in 5 kinematical variables and 3 bins in 9 data-taking periods. The assignment of the markers to the particular period can be found in the legend in the top left plot.
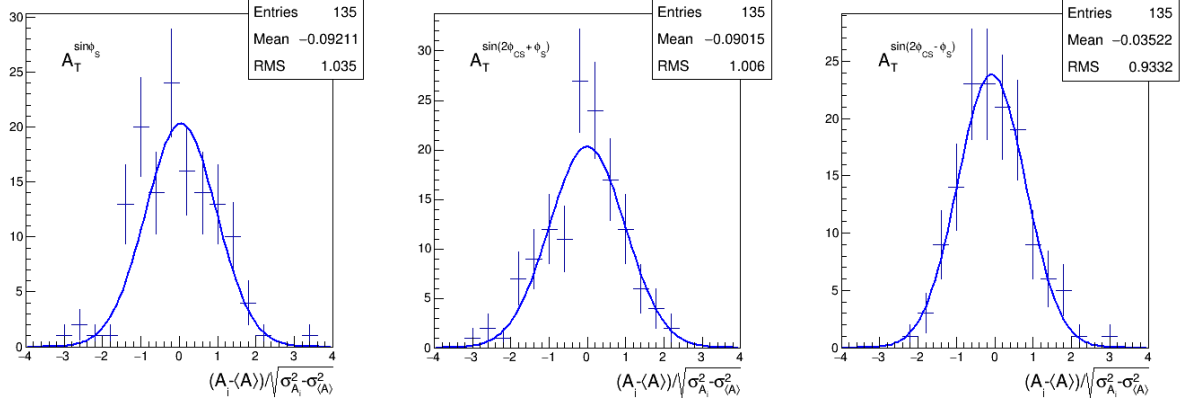
Figure 3.26: The pulls of all the values of asymmetries in all the periods from the average value of the Sivers (left), Pretzelosity (middle), and Transversity (right) asymmetry.

3.5.2 The Evaluation of the false asymmetries

The false asymmetries are obtained by combining the data in a way that the spin effects cancel out. We have tested two types of the false asymmetries (FA):

1) Dividing the periods in two fake sub-periods: the odd runs are considered as the first sub-period and the even runs compose the second sub-period (here denoted FA_1).

2) Division of the target cells into two sub-cells to make two fake cells in the following way: first part of the first cell and the second part of the second cell comprise the first, upstream fake cell, and the second sub-cell of the first cell and the first sub-cell of the second is the second, downstream fake cell (denoted FA_2).

And otherwise the data are treated the same as the physics data with the DR method. The FAs are expected to be compatible with zero as the physics effect disappears with the polarisation cancelling out. Possible non-zero effect would indicate an azimuthal modulation in the acceptance, which did not cancel out after the use of DR method. The procedure for estimating the influence on the systematic error is following: As the two data sets used for evaluating the FAs are the same, i.e. the results are correlated, we had to evaluate the ratio of systematic error to the statistical one, the α, separately for both of the FAs, in a following way (similarly as in ref. [24]):

$$\frac{\sigma_{syst.,i,period}}{\sigma_{stat.,i,period}} = \alpha_{i,period} = \sqrt{\frac{\left|FA_{i,period}\right|^2}{\sigma^2_{FA_{i,period}}} - 0.68^2} \ . \tag{3.12}$$

The α was measured for both of the FA_i as an integrated value of all the data per period. If the value of error-weighted FA is lower than 0.68, then the $\alpha_{i,period}$ is equal 0.
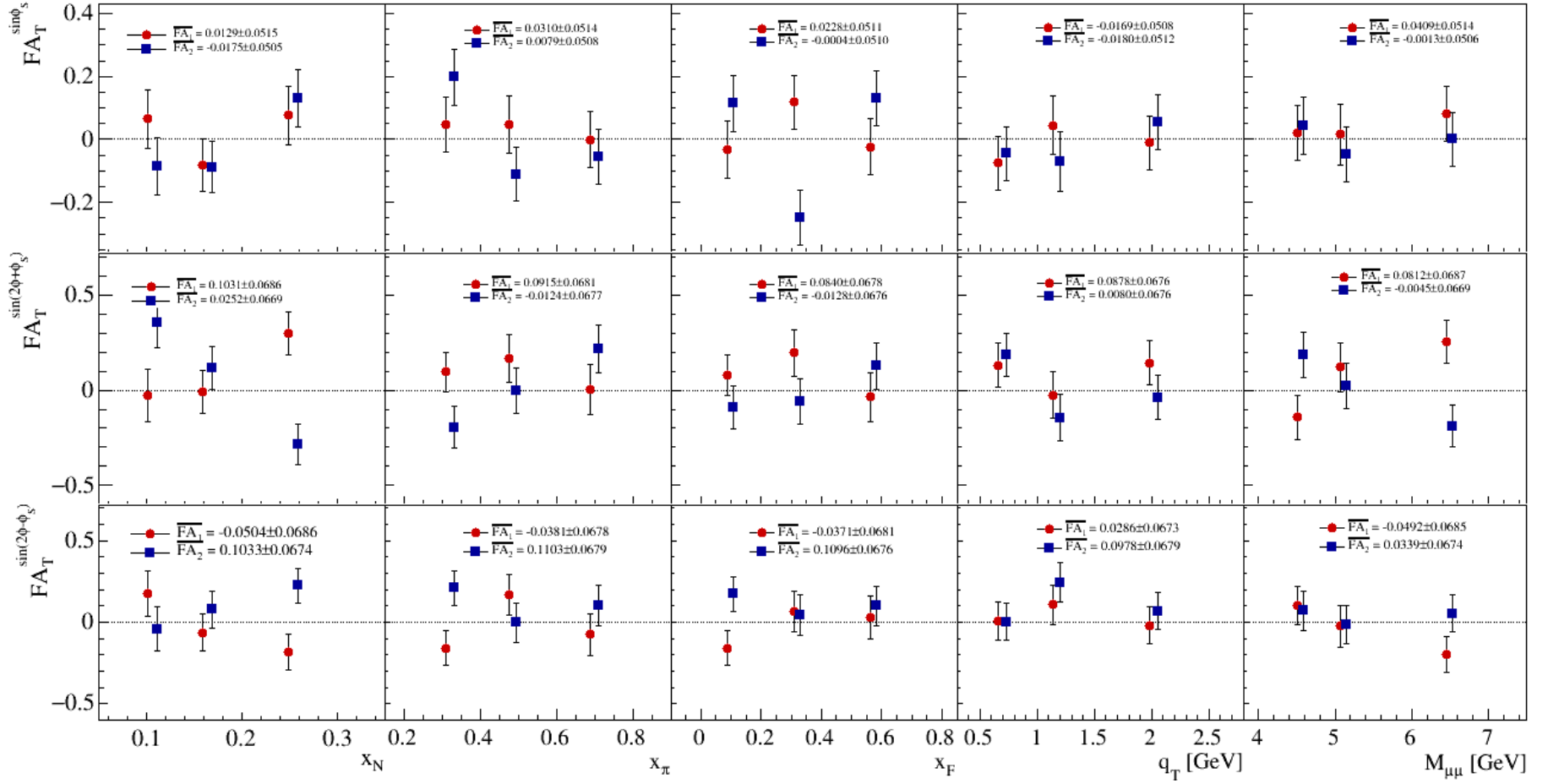
76

Figure 3.27: The results for both of the *FA*s as a weighted average of all the periods where the red points show the *FA₁* and the blue points stand for the *FA₂*. The legend shows their mean values.
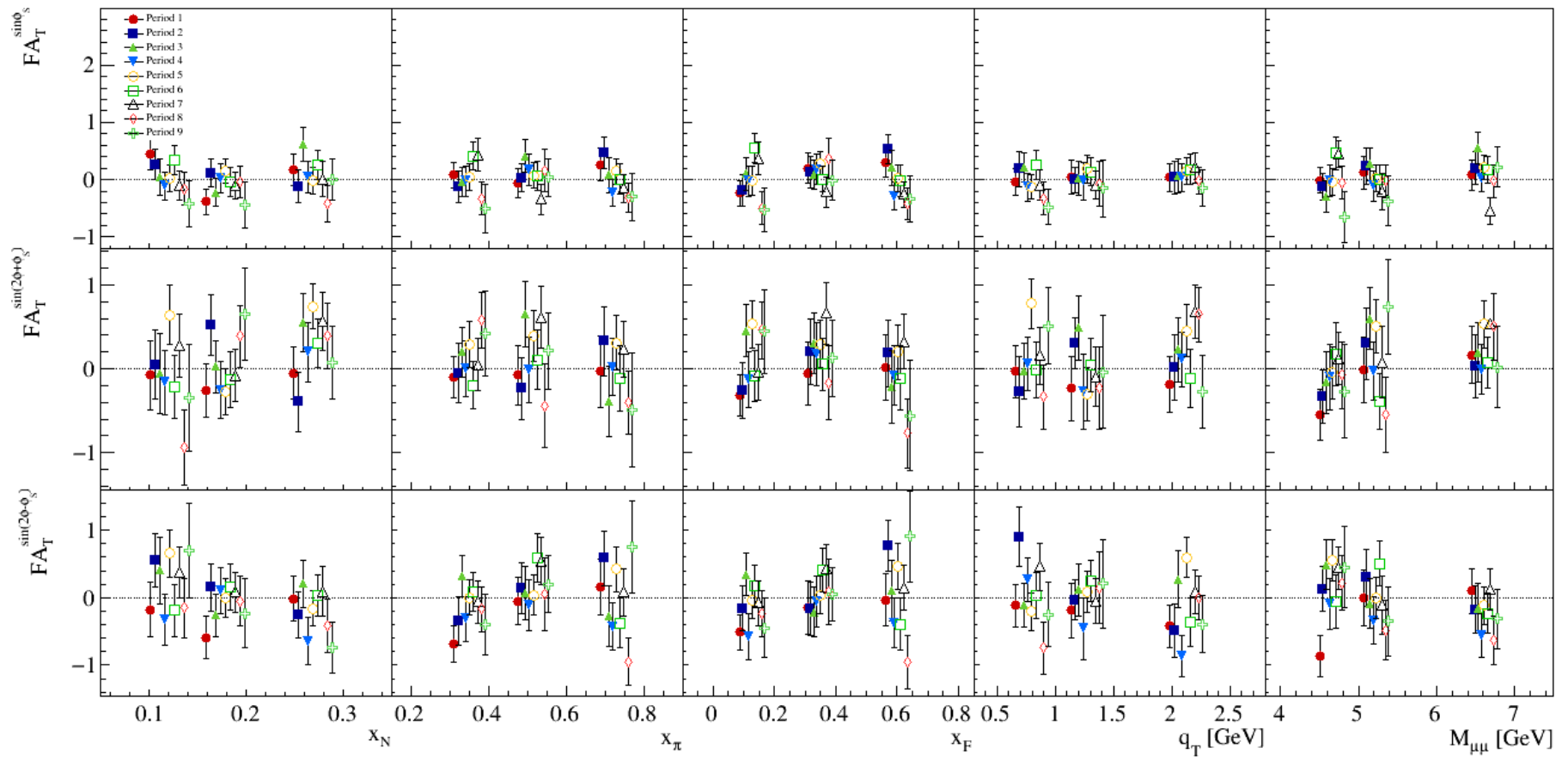
Figure 3.28: The results of the FA_1 for all the periods in 3 bins.
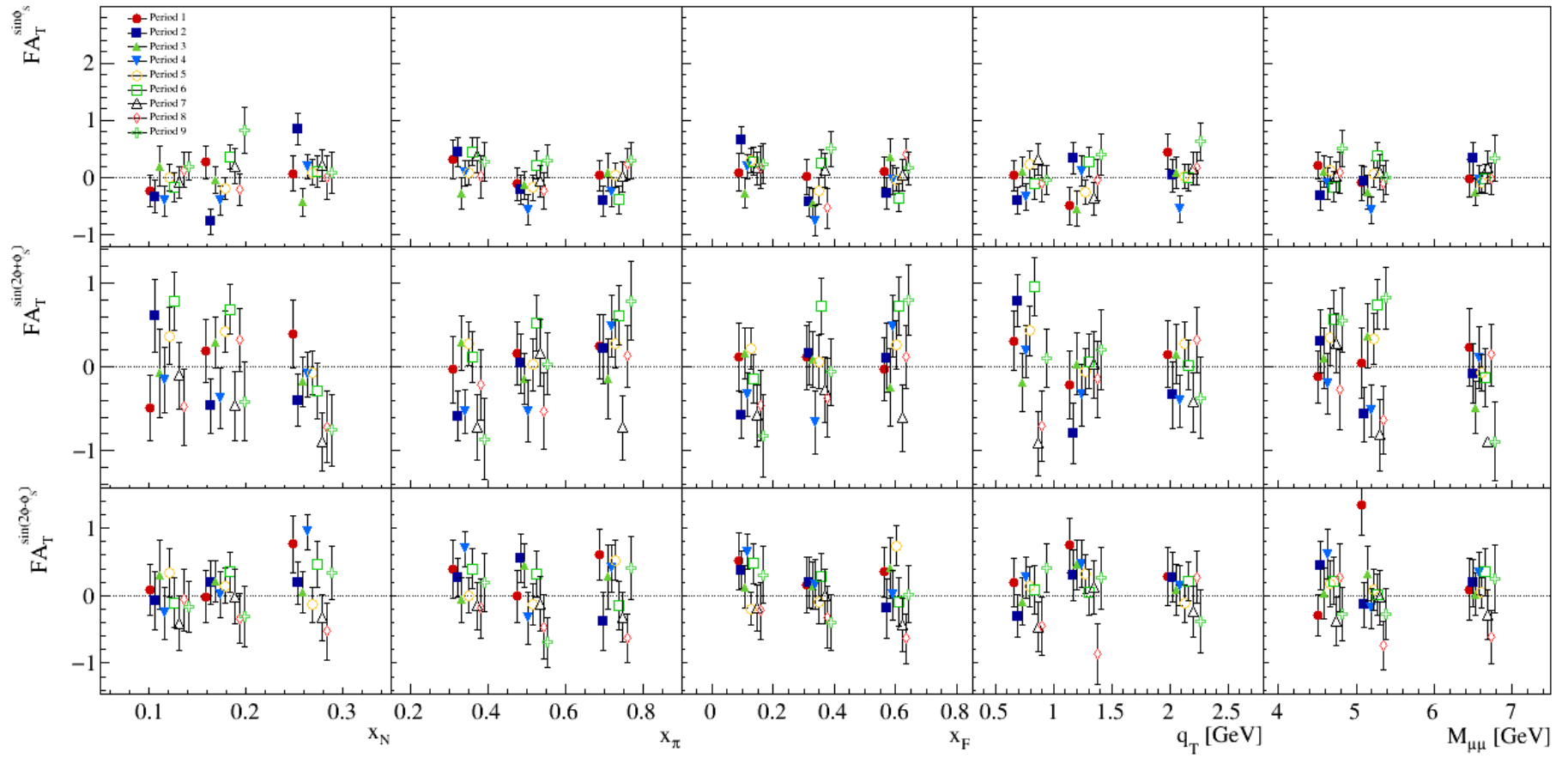
Figure 3.29: The results of the *FA₂* for all the periods in 3 bins.

The meaning of the 0.68 squared subtraction is that we use the absolute value of the *FA* instead of its real value, i.e. the final distribution of the FA_i results in not a Gaussian centred at zero, but a function (half a Gaussian going from 0 to infinity) with a median at 0.68. Thus, the 0.68 is the expected value and we need to know the deviation of the results from this value, whether they are lower (in that case the α is zero as was pointed out) or larger and must be accounted to the systematic effect. More detailed information can be found in the refs. [24],[53].

These $\alpha_{i,period}$ values are then averaged for both of the FA_i:.

$$\frac{\sigma_{syst.,period}}{\sigma_{stat.,period}} = \alpha_{period} = \frac{\alpha_{1,period} + \alpha_{2,period}}{2} \,. \tag{3.13}$$

And then the final value is given as a simple average over the periods:

$$\frac{\sigma_{syst}}{\sigma_{stat}} = \alpha = \frac{\sum_{period}\alpha_{period}}{9} \,. \tag{3.14}$$

This gives us the final contribution of the FA test to the systematic error showed in the following table:

Asymmetry	$\sigma_{syst}/\sigma_{stat}$
Sivers	0.4
Pretzelosity	0.6
Transversity	0.6

Table 3.8: The values of α for all the asymmetries.

The figures 3.30 and 3.31 show the pulls of the measured values of FA_1 and FA_2, respectively, of their average values. One can see that they are all centred on zero and their *RMS's* are approximately 1, except the Pretzelosity which shows a slight statistical incompatibility.

As the period compatibility test proved that there is no systematic effect in data stability, the final error estimation with taking into account the uncertainty of the target polarisation and the dilution factor for the 3 measured asymmetries then is simply given as:

$$\begin{aligned}
\sigma_{syst,A_S} &= \sqrt{(0.05A_S)^2 + (0.05A_S)^2 + (0.4\sigma_{stat})^2}\,, \\
\sigma_{syst,A_P} &= \sqrt{(0.05A_P)^2 + (0.05A_P)^2 + (0.6\sigma_{stat})^2}\,, \\
\sigma_{syst,A_T} &= \sqrt{(0.05A_T)^2 + (0.05A_T)^2 + (0.6\sigma_{stat})^2}\,,
\end{aligned} \tag{3.15}$$

where the Sivers asymmetry is denoted as A_S, the Pretzelosity asymmetry as A_P, and the Transversity asymmetry is A_T. The numerical evaluation of the systematic errors is presented in the next Section 3.6 together with the results of the asymmetries extraction.
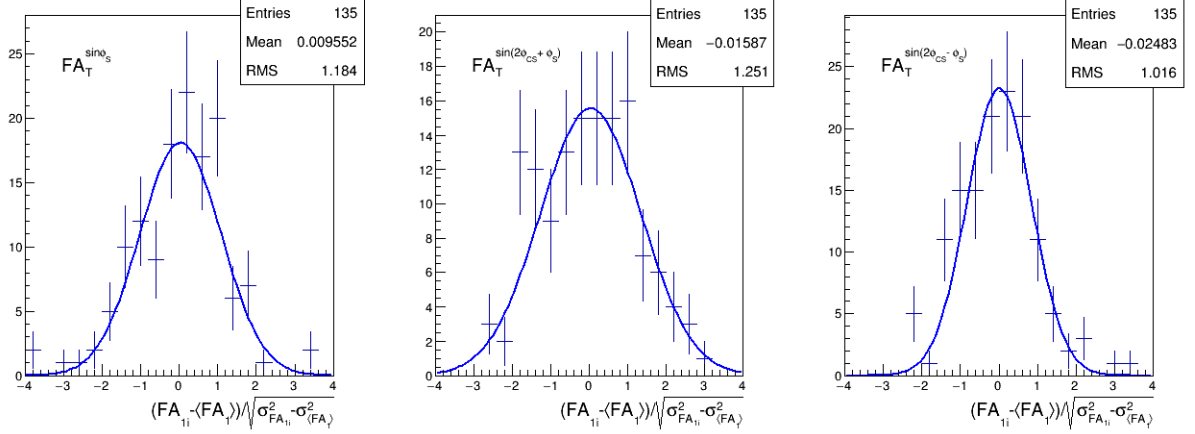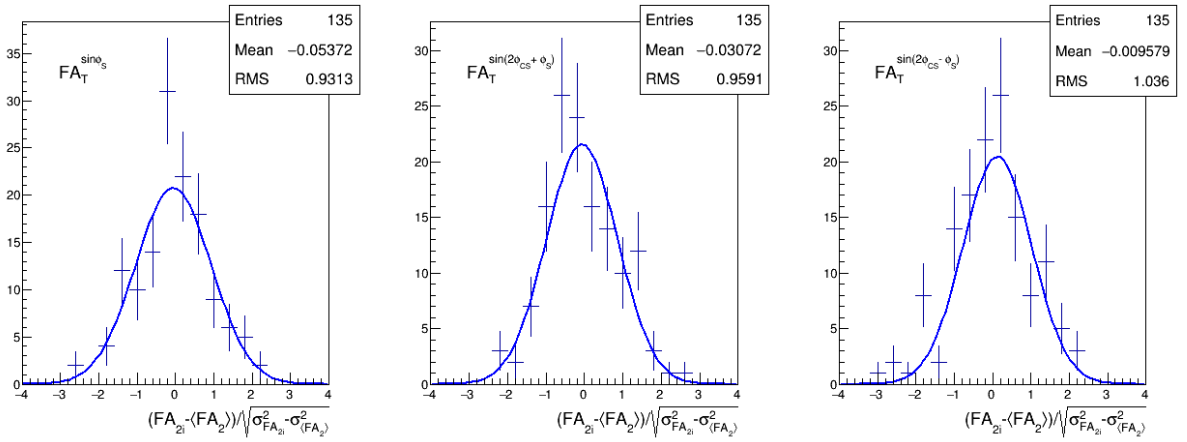
Figure 3.30: The pulls from the average value of FA_1.

Figure 3.31: The pulls from the average value of FA_2.

3.6 The Results of the Transverse spin asymmetries

In this section the results from the extraction of the TSAs from the COMPASS 2015 DY data are presented. The asymmetries were obtained by the double-ratio method in 5 kinematical variables: x_N, x_π, x_F, q_T, and $M_{\mu\mu}$ in 3 bins each. The weighted average of the 3 analysed asymmetries over the periods is presented in the figure 3.32. The systematic uncertainties have been evaluated to $0.4\sigma_{stat}$ for Sivers asymmetry and $0.6\sigma_{stat}$ for Pretzelosity and Transversity asymmetries. In the figure 3.32 the systematic uncertainties are presented in the form of bands. The mean values of the asymmetries and their σ_{stat}, averaged over all the periods, for particular kinematic variables are shown in the legend. The integrated values of all the asymmetries, determined from the fit of all the data and averaged over periods, are depicted in the figure 3.33. The Sivers asymmetry has been measured to be at about 1 standard deviation positive. Our results are summarized in the table 3.9. They are perfectly in agreement with the official results of the COMPASS analysis [52],[53].
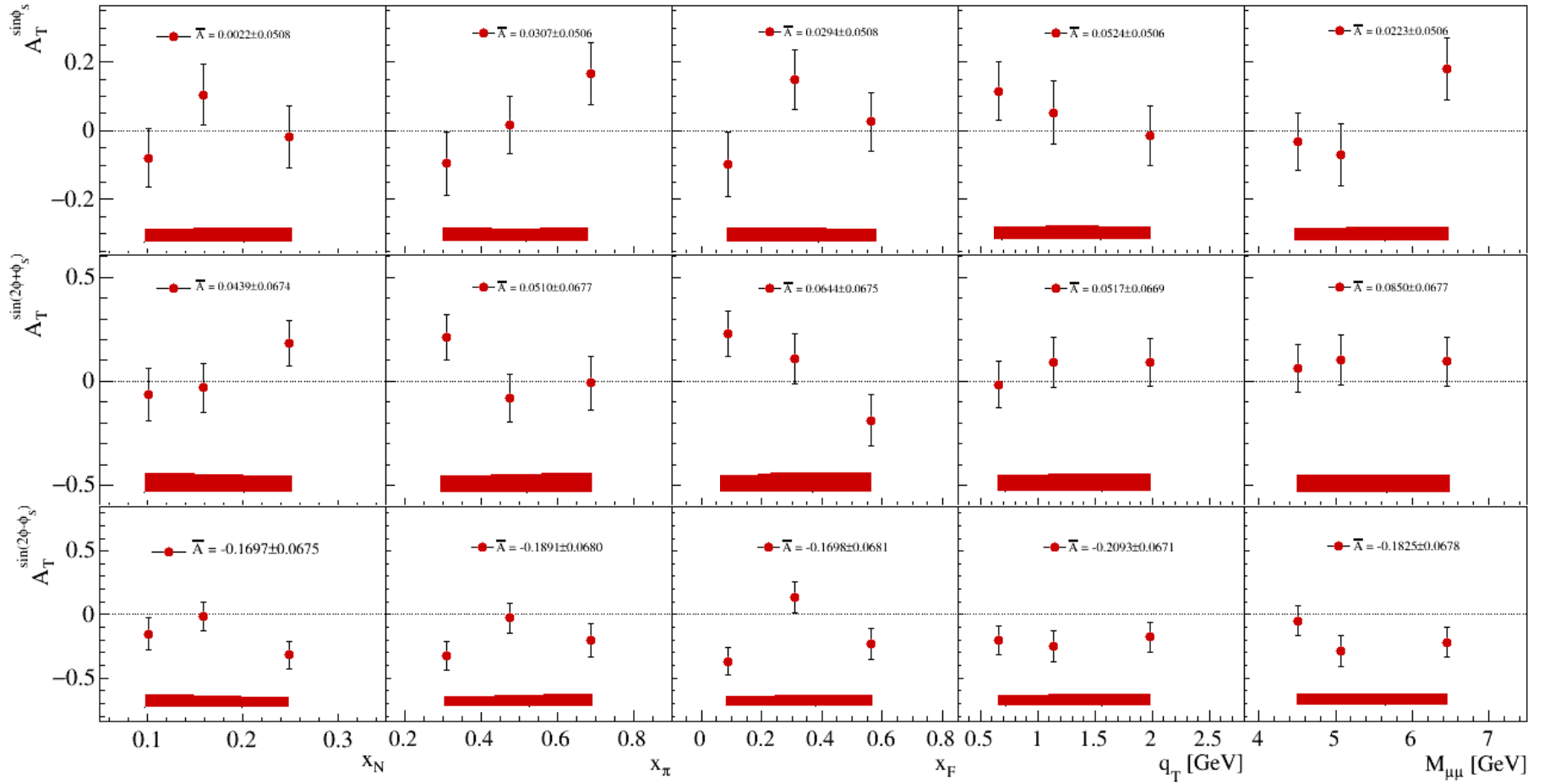
Figure 3.32: The final results for the TSA asymmetries. The mean values are showed in the legend. The systematic uncertainties are depicted as the bands.
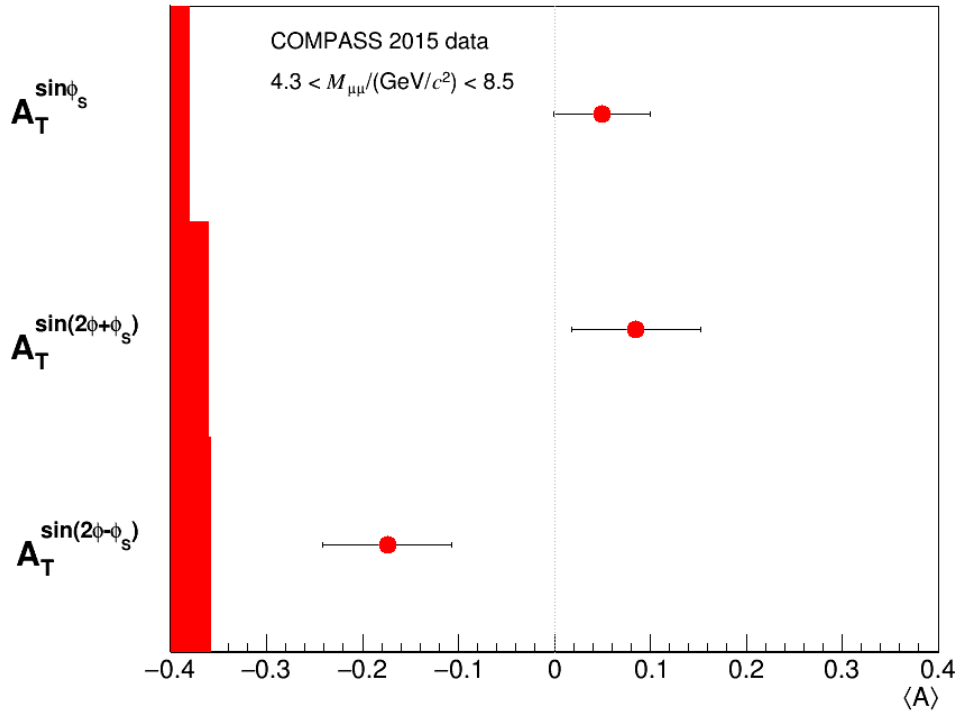
Figure 3.33: The three extracted asymmetries averaged over the whole kinematic range.

In this thesis, the sign convention of the TSAs is given by the eq. (1.73) together with the definition of the Collins-Soper reference frame (see fig. 1.13). However, the relation of the sign of the Sivers TSA and the sign of the Sivers TMD PDF is given only by a convention. In the SIDIS case (eq. (1.82) and fig. 1.15) the angle describing the Sivers modulation $(\phi_h - \phi_s)$ is rotated with respect to the DY Sivers modulation (ϕ_s) by π. Thus the sign change prediction in our case results in the same sign of the measured Sivers asymmetry in SIDIS (see fig. 1.10) and DY. In the figure 3.34 a comparison of the measured Sivers asymmetry by COMPASS with the recent theoretical predictions on the asymmetry and the sign change [61],[62],[63] is shown[18]. The predictions are based on the different Q^2-evolution approaches and collectively state the positive sign for the Sivers TSA if the sign-change hypothesis is considered. The lower band is the prediction in case that no sign change is present. The first measurement of the Sivers asymmetry by COMPASS and the result of our analysis together are consistent with the prediction for the sign change with the certainty of 1 σ.

Asymmetry	$<A>$	σ_{stat}	σ_{syst}
$A_T^{sin(\phi s)}$	0.050	0.050	0.020
$A_T^{sin(2\phi+\phi s)}$	0.085	0.067	0.041
$A_T^{sin(2\phi-\phi s)}$	-0.174	0.068	0.042

Table 3.9: The final results of the asymmetries.

---

[18] The value of the Sivers is taken from the official analysis as their result is about 1% higher but well compatible within the error. See ref. [52].

The Pretzelosity asymmetry has been measured to be more than 1 σ positive. On the other hand, the Transversity asymmetry is below zero with a significance of about 2 standard deviations. The obtained value can be used for the study of the universality of the transversity TMD function $h_1^q(x)$. Both of the asymmetries, Pretzelosity and Transversity, are also related to the pion Boer-Mulders TMD function (see Section 1.4) thus the obtained results can be further used for studying of the characteristics of this function and determining its sign.
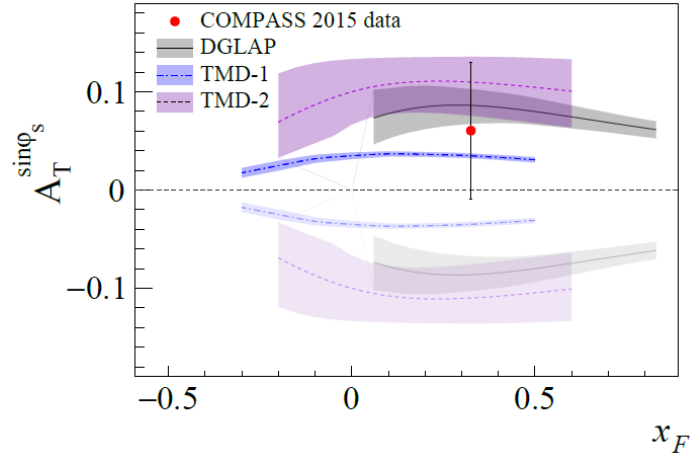

Figure 3.34: The measured average Sivers asymmetry with the total uncertainty in the comparison with theoretical predictions [61],[62],[63] for a different Q^2-evolution scheme, namely the DGLAP (ref. [61]), TMD1 (ref. [62]), and TMD2 (ref. [63]). The highlighted distributions denote the sign change while the shaded ones no sign change.

Conclusion

The Drell-Yan and the Semi-inclusive DIS processes are two complementary tools capable of accessing the spin-dependent structure functions of the nucleon. The Drell-Yan has the advantage the cross-section consists only from a convolution of Transverse-Momentum-Dependent PDFs and no fragmentation function is present. The COMPASS experiment is a unique spectrometer with a setup adapted for measurements of both processes. The SIDIS measurement on transversely polarised proton target took place in 2007 and 2010. In 2015 COMPASS took the first polarised DY data using the negative pion beam and the polarised proton target. The continuation of the polarised DY data-taking is planned for 2018.

The goal of this thesis was the extraction of the DY Transverse-spin-dependent azimuthal asymmetries from the 2015 COMPASS data: the Sivers asymmetry, the Pretzelosity asymmetry, and the Transversity asymmetry. In the first part, the physics principles of the DY process were presented. The QCD improved parton model was reviewed and the TMD approach briefly outlined. The DY formalism and the measured modulations of the cross-section were introduced with the emphasis on the transverse-spin-dependent amplitudes. The main aim of the COMPASS DY and SIDIS measurements, i.e. the test of the universality of the T-odd TMD PDFs, was presented. The special attention was given to the Sivers asymmetry which is connected with the T-odd Sivers TMD function and should change the sign when measured in DY w.r.t. SIDIS in order to prove the validity of the TMD-approach in QCD.

The description of the experimental setup was given in the next part. The COMPASS is a two-stage magnetic spectrometer with about 300 tracking planes with an angular acceptance up to 200 mrad. The experimental beamline and setup is adapted for supporting both lepton and hadron beams (namely muons, and pions, respectively). The setup used for the DY measurement was described. The operation principles of the COMPASS polarised target were outlined. And the basic principles of the data acquisition and the new DAQ system were given.

The analysis of the 2015 DY data was presented. Firstly, we showed the properties of the beam, the data-taking strategy, and the MC simulations done by the collaboration to map the spectrometer acceptances and resolutions. We presented the data stability study done by the collaboration needed for the event selection of the dimuon candidates. Then, the intrinsic part of our analysis was given. The influence of the selections and the properties of the data

sample were illustrated. The method of the transverse-spin-dependent asymmetries was introduced. The results of the extracted asymmetries are presented together with the test for the systematic uncertainties. The obtained results are in agreement with the output of the official independent analysis done by the collaboration [52]. The measured value of Sivers is 1-σ positive which is a hint for the predicted sign change. We present our results with the statistical and systematic uncertainties for the Sivers, Pretzelosity, and Transversity asymmetries, respectively as follows:

$$A_T^{\sin\phi_S} = 0.050 \pm 0.050 \pm 0.020,$$
$$A_T^{\sin(2\phi+\phi_S)} = 0.085 \pm 0.067 \pm 0.041,$$
$$A_T^{\sin(2\phi-\phi_S)} = -0.174 \pm 0.068 \pm 0.042.$$

Bibliography

[1] Ashman, J. et al. [EMC Collaboration]: *An Investigation of the Spin Structure of the Proton in Deep Inelastic Scattering of Polarized Muons on Polarized Protons*. Nucl. Phys. B328, 1-35, 1989.

[2] Alexseev, M. et al. [COMPASS collaboration]: *Direct Measurement of the Gluon Polarisation in the Nucleon via Charmed Meson Production*. CERN–PH–EP/2008–003, 2008. https://arxiv.org/abs/0802.3023

[3] Matoušek, J.: *Studies of Drell-Yan process at Compass experiment*. Diploma thesis, Charles University, Prague, 2013, available at: http://wwwcompass.cern.ch/compass/publications/welcome.html#theses.

[4] Chýla, J.: *Quarks, partons and Quantum Chromodynamics*. Praha, 2004, available at: http://www-ucjf.troja.mff.cuni.cz/new/wp-content/uploads/2014/02/text.pdf.

[5] Williams, W. S. C.: *Nuclear and Particle Physics*. Oxford University Press, 1991.

[6] Devenish, D., Cooper, A.: *Deep Inelastic Scattering*. Oxford University Press, 2011.

[7] Levorato, S.: *Measurement of transverse spin effects in COMPASS on a polarised proton target*. PhD thesis, Trieste, 2008, available at: http://wwwcompass.cern.ch/compass/publications/theses/2009_phd_levorato.pdf

[8] Bjorken, J. D, Paschos, E. A.: *Asymptotic Sum Rules at Infinite Momentum*. Phys. Rev. 179 (1969), 1547- 1553.

[9] Pešek, Míša: *Low temperature proton polarized target for nucleon structure studies at COMPASS*. Diploma Thesis, Charles University, Prague (2014), available at: http://wwwcompass.cern.ch/compass/publications/welcome.html#theses.

[10] Chekanov, S. et al. [ZEUS Collaboration], Eur. Phys. J. C 21, 443 (2001)

[11] Adloff, C. et al. [H1 Collaboration], Eur. Phys. J. C 21, 33 (2001)

[12] Whitlow, L. W. et al., Phys. Lett. B 282, 475 (1992).

[13] Benvenuti, A. C. et al. [BCDMS Collaboration], Phys. Lett. B 223, 485 (1989).

[14] Adams, M. R. et al. [E665 Collaboration], Phys. Rev. D 54, 3006 (1996).

[15] Arneodo, M. et al. [New Muon Collaboration], Nucl. Phys. B 483, 3 (1997).

[16] Adeva, B. et al.: *Spin asymmetries A_1 and structure functions g_1 of the proton and the deuteron from polarized high energy muon scattering*. Phys. Rev., D58:112001 (1998).

[17] Patrignani C. et al.: *Particle Data Group*, Chin. Phys. C, 40, 100001 (2016).

[18] Alekseev, M. et al. [COMPASS Collaboration]: Phys. Lett. B 693 (2010), 227-235.

[19] Adolph, C. et al. [COMPASS collaboration]: *The Spin structure function $g_1{}^p$ of the proton and a test of the Bjorken sum rule*. Phys. Lett. B753 (2016).

[20] de Florian, D. et. al.: *Evidence for Polarisation of Gluons in the Proton*. Phys. Rev. Lett.113, 012001 (2014).

[21] Jaffe R.L., Manohar A., Nucl. Phys. B 337 (1990), 509.

[22] Barone, V. et al.: *Transverse Polarisation of Quarks in Hadrons*. Phys. Rept. 359 (2002) 1-168.

[23] Boer, D., Mulders, P.J.: *Time-reversal odd distribution functions in leptoproduction*. Phys. Rev. D57 (1998) 5780–5786, arXiv:hep-ph/9711485.

[24] Quaresma, M. M. V.: *Transverse Momentum Dependent Parton Distribution Functions through SIDIS and Drell-Yan at COMPASS*. PhD thesis, Lisboa (2016), available at: http://wwwcompass.cern.ch/compass/publications/theses/2016_phd_quaresma.pdf

[25] Ralston, J. P., Soper, D. E.: Nucl. Phys., B 152, (1979) 109.

[26] Adolph, C. et al. [COMPASS collaboration]: *Sivers asymmetry extracted in SIDIS at the hard scale of the Drell-Yan process at COMPASS*. arXiv:1609.07374 [hep-ex] CERN-EP-2016-250 (2016).

[27] Mulders, P. J.: *Transverse momentum dependence in structure functions in hard scattering processes*. Private notes, Amsterdam (2000).

[28] Collins, J. C., Metz, A.: *Universality of Soft and Collinear Factors in Hard-Scattering Factorization*. Phys. Rev. Lett. 93, 252001 (2004).

[29] Collins, J. C.: *Leading-twist Single-transverse-spin asymmetries: Drell-Yan and Deep Inelastic Scattering*. Phys. Rev. Lett. 536, 43 (2002).

[30] Frederix, R.: *Wilson Lines in QCD*. Master thesis, Amsterdam, 2005, available at: https://www.nikhef.nl/pub/theory/masters-theses/rikkert_frederix.pdf

[31] Sivers, D.: *Single-spin asymmetries from the hard scattering of pointlike constituents*. Phys. Rev. D 41 (1990).

[32] Arnold, S. et. al.: *Sivers effect at Hermes, Compass and Clas12*. arXiv:0805.2137 [hep-ph] JLAB-THY-08-820 (2008).

[33] Avakian, H., et al.: *Pretzelosity distribution function $h_{1T}^{\perp}$ and the single spin asymmetry $A_{UT}^{\sin(3\phi-\phi_S)}$*. Phys. Rev. D 78 (2008), 114024.

[34] Arnold, S., Metz, A., Schlegel, M.: Phys. Rev. D 79 (2009), 034005.

[35] Drell, S. D., Yan, T. M.: Phys. Rev. Lett. 25 (1970), 316.

[36] Brodsky, S. J. et. al.: *Initial-state interactions and single-spin asymmetries in Drell-Yan processes*. Nucl. Phys. B 642 (2002) 344–356.

[37] Gautheron, F. et al. [The COMPASS collaboration]: *COMPASS-II Proposal*. CERN-SPSC-2010-014 (2010), SPSC-P-340.

[38] Kotzinian, A. [The COMPASS collaboration]: *Description of polarized π^- and N Drell-Yan processes*. COMPASS Note 2010-2 (2010).

[39] Kleinjan, D.: *A Future Polarized Drell-Yan Experiment at Fermilab*. arXiv:1510.00636 [nucl-ex] CIPANP2015-KLEINJAN (2015).

[40] Bacchetta, A. et al.: *Semi-inclusive deep inelastic scattering at small transverse momentum*. JHEP 0702 (2007), p. 93. arXiv:hep-ph/0611265v2.

[41] Brodsky, S. J. et. al.: *Final-state interactions and single-spin asymmetries in semi-inclusive deep inelastic scattering*. Phys. Lett. B 530 (2002) 99–107.

[42] Abbon, P. et al. [The COMPASS collaboration]: The COMPASS experiment at CERN, NIMA 577, 455-518, 2007.

[43] Pešek, M.: *DY express analysis*. Presented on the COMPASS Weekly meeting, August 31, 2015.

[44] Nový, J.: *COMPASS DAQ – Basic control system*. Diploma Thesis, CTU, Prague, 2012.

[45] Bodlák, M. et al.: *New data acquisition system for the COMPASS experiment.* Journal of Instrumentation, 2013-02-01, vol. 8, issue 02 (2013), available at: http://iopscience.iop.org/1748-0221/8/02/C02009/.

[46] Abbon, P. et al. [The COMPASS collaboration]: *The COMPASS setup for Physics with Hadron Beams*. NIMA 779, 69 (2014).

[47] [COMPASS collaboration]: *Vertex detector meeting*. December, 14, 2015.

[48] Kondo, K. et al. [The COMPASS collaboration]: *Polarization measurement in the COMPASS polarized target*. NIMA 526, 70-75 (2004).

[49] Matoušek, J.: *Polarised target for Drell–Yan experiment in COMPASS at CERN, part I*. Presented on The 22nd international spin symposium, September 25-30, 2016, Illinois, USA.

[50] Matoušek, J. and Pešek, M.: *Proceedings of the XVth International workshop on polarised sources and polarimetry*. September 9-13, 2013, Charlottesville, Virginia, USA.

[51] Doshita N. et al. [The COMPASS collaboration]: Performance of the COMPASS polarized target dilution refrigerator, NIMA 526 (2004), 138-143.

[52] Aghasyan, M. [The COMPASS collaboration]: *First measurement of transverse-spin-dependent azimuthal asymmetries in the Drell-Yan process*. CERN-EP/2017-059, hep-ex/1704.00488 (2017), submitted to PRL.

[53] Andrieux, V. et al. [The COMPASS collaboration]: *Transverse-spin-dependent azimuthal Drell-Yan asymmetries from COMPASS 2015 data*. COMPASS Note (2017).

[54] Longo, R., Parsamyan, B.: *TGeant MC for DY: impact of trigger efficiencies and other updates*. Presented on the COMPASS Drell-Yan meeting, February 7, 2017.

[55] Parsamyan, B., Quaresma, M. M. V., Vit, M.: *COMPASS Drell-Yan 2015 data with NH₃ and W targets: ongoing analysis, Kinematic distributions and projected uncertainties for the asymmetries*. Presented on the COMPASS Analysis meeting, June 22, 2016.

[56] Parsamyan, B.: *Analysis and Interpretation of Transverse Spin Dependent Azimuthal Asymmetries in SIDIS at the COMPASS Experiment*. PhD thesis, Torino (2007), available at:
http://wwwcompass.cern.ch/compass/publications/theses/2007_phd_parsamyan.pdf

[57] Ivanov, A., Parsamyan, B.: *Data stability W07-10-12*. Presented on the COMPASS Drell-Yan meeting, May 17, 2016.

[58] Ivanov, A..: *Data stability W12t1-W12t3*. Presented on the COMPASS Drell-Yan meeting, August 31, 2016.

[59] Quaresma, M. M. V.: *2015 data analysis, Middle trigger and theta cut*. Presented on the COMPASS Drell-Yan meeting, January 17, 2017.

[60] Parsamyan, B.: *Status and general comments on the polarized Drell-Yan analysis concept*. Presented on the COMPASS Analysis meeting, January 19, 2017.

[61] Anselmino, M., et al.: *Study of the sign change of the Sivers function from STAR Collaboration W/Z production data*. arXiv:1612.06413 [hep-ph].

[62] Sun, P., Yuan, F.: Phys. Rev. D 88 (2013) no.11, 114012.

[63] Echevarria, M. G., Idilbi, A., Kang, Z. B. and Vitev, I.: Phys. Rev. D 89 (2014) 074013.

List of Abbreviations

BDM	Beam Decay Muons
BMS	Beam Momentum Station
CASTOR	CERN Advanced STORage manager
CB	Combinatorial Background
CEDAR	Cherenkov Differential counter with Achromatic Ring focus
CERN	European Organization for Nuclear Research (originating from 'Conseil Européen pour la Recherche Nucléaire')
CMS	Center-of-mass System
COMPASS	Common Muon and Proton Apparatus for Structure and Spectroscopy
CORAL	COmpass Reconstruction and AnaLysis
CS	Collins-Soper frame
DAQ	Data Acquisition System
DC	Drift Chamber
DIS	Deep inelastic scattering
DNP	Dynamic Nuclear Polarization
DR	Dilution Refrigerator
DVCS	Deep Virtual Compton Scattering
DY	Drell-Yan
ECAL(1,2)	Electromagnetic calorimeter (1 or 2)
EMC	European Muon Collaboration
FA	False Asymmetries
HCAL(1,2)	Hadronic Calorimeter (1 or 2)
LAB	Laboratory frame
LAS	Large Angle Spectrometer
LAST	Large Angle Spectrometer Trigger

|	
LO QCD	Leading-Order Quantum Chromodynamics
MC	Monte Carlo method
mDST	mini Data Summary Trees
µDST	micro Data Summary Trees
MDT	Mini Drift Tubes modules
MW(1,2)	Muon Wall (1 or 2)
MWPC	Multiwire Propotional Chamber
MT	Middle Trigger
NMR	Nuclear Magnetic Resonance
OT	Outer Trigger
PT	Polarised Target
QCD	Quantum Chromodynamics
QED	Quantum Electrodynamics
QM	Quark Model
PHAST	PHysics Analysis Software Tool
RICH	Ring Imaging Cherenkov detector
SAS	Small Angle Spectrometer
SciFi	Scintilating Fibers
SIDIS	Semi-inclusive deep inelastic scattering
SLAC	Standford Linear Accelerator
SPS	Super Proton Synchrotron
TF	Target rest Frame

Attachment
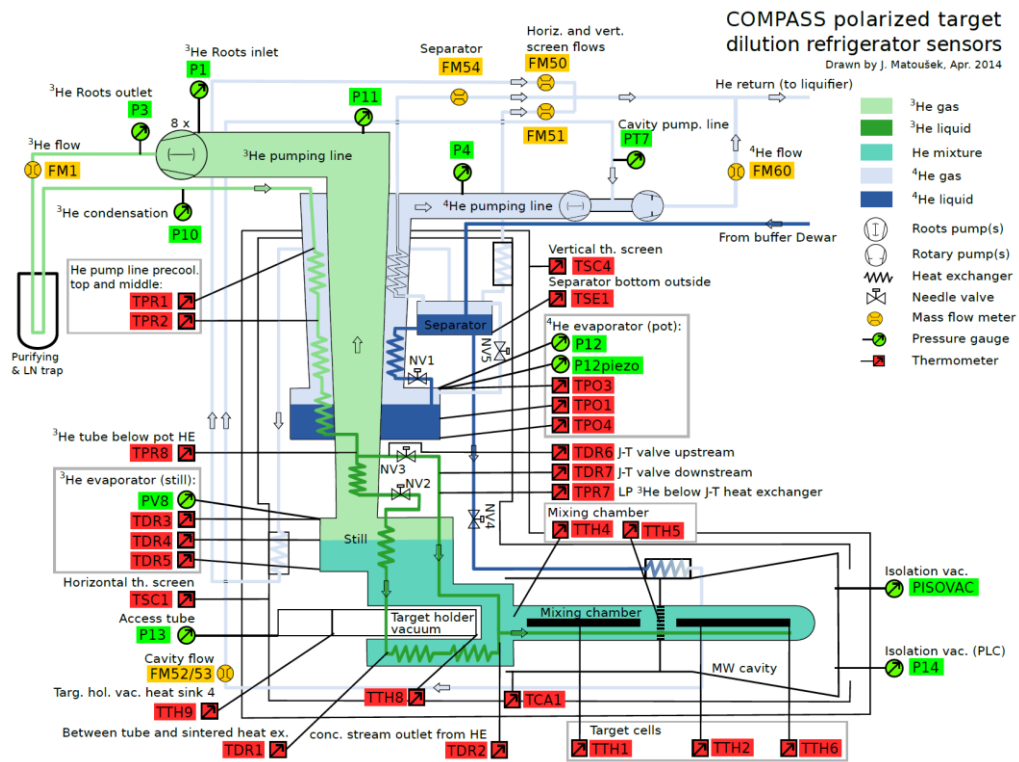
Attachment 1: The detailed scheme of the PT dilution refrigerator.
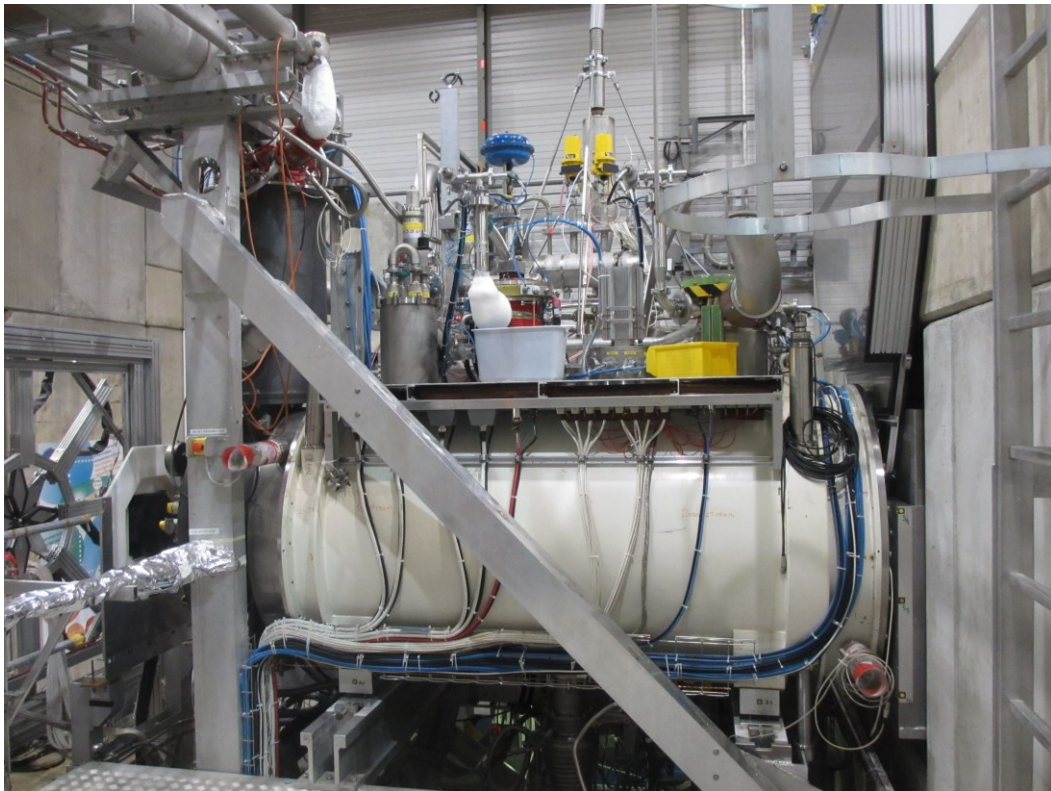
Attachment 2: The polarised target. The vertical black tube on left contains the main part of the dilution refrigerator.
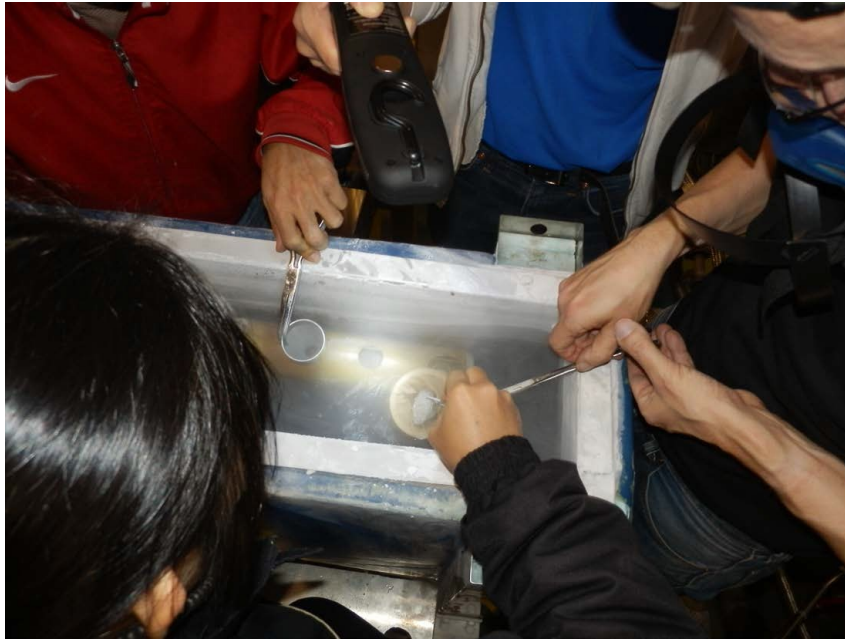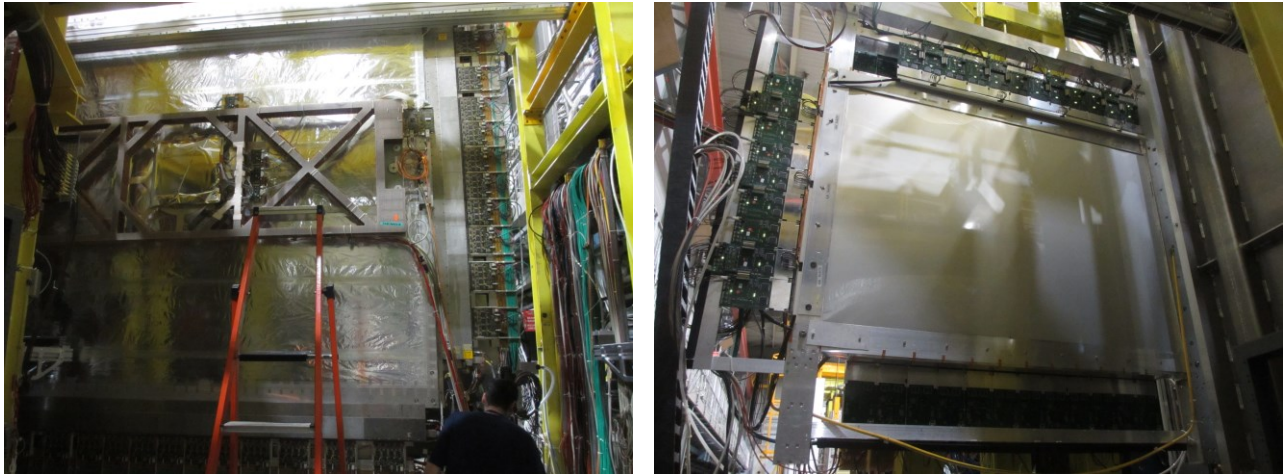
Attachment 3: The target material loading.
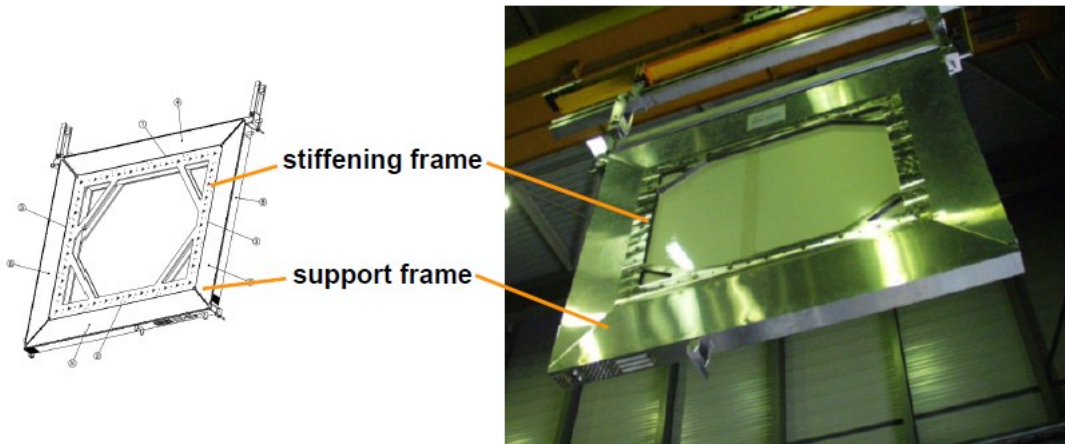
Attachment 4: The new DC05 detector.

Attachment 5: The works on the installation of the DC05. The left upper figure shows the DC04 in the garage position from upstream side. On the right upper, the Straw3 is being moved out to the garage position beside the DC04. The left bottom in the Straw3 already parked and the right bottom shows the MWPC PS01 detector also in the parking position.